2020

Competing And Cooperating Orders In The Three-Band Hubbard Model: A Comprehensive Quantum Monte Carlo And Generalized Hartree-Fock Study

Adam Chiciak
William & Mary - Arts & Sciences, adamthecheech@gmail.com

Competing and Cooperating Orders in the Three-Band Hubbard Model: A Comprehensive Quantum Monte Carlo and Generalized Hartree-Fock Study

Adam C. Chiciak

New York, New York

Master of Science, College of William & Mary, 2016
Bachelor of Science, Villanova University, 2014

A Dissertation presented to the Graduate Faculty
of The College of William & Mary in Candidacy for the Degree of
Doctor of Philosophy

Department of Physics

College of William & Mary
August 2020

APPROVAL PAGE

This Dissertation is submitted in partial fulfillment of
the requirements for the degree of

Doctor of Philosophy

Adam Chiciak

Adam Carl Chiciak

Approved by the Committee June 2020

Committee Chair
Shiwei Zhang, Chancellor Professor, Physics
College of William & Mary

Enrico Rossi

Enrico Rossi, Associate Professor, Physics
College of William & Mary

George Vahala, Professor, Physics
College of William & Mary

Henry Krakauer, Professor, Physics
College of William & Mary

Ettore Vitali

Ettore Vitali, Assistant Professor, Physics
California State University, Fresno

ABSTRACT

Significant progress has been made in studying strongly correlated electronic systems with major focus on understanding high-temperature superconductivity. At the center of these studies are the so-called cuprates, which are characterized by a quasi-2D Copper-Oxide plane in which superconductivity is believed to arise. From the theoretical point of view, the complex electronic structure of these materials makes a fully ab initio many-body computation a formidable task, so we are forced to focus on minimal models that can reproduce the physics, the most well known of which is known as the Hubbard Model, which relies on the Zhang-Rice singet notion to reduce the degrees of freedom by treating the oxygen atoms implicitly. However, despite years of study, the superconducting order is still unknown. Moreover, recent experiments indicate that the oxygen p-bands play a significant role as non-trivial hole carriers, so we find it fit to study the three-band Hubbard (Emery) model, which treats the oxygen p-orbitals explicitly. We perform extensive generalized Hartree–Fock and auxiliary-field quantum Monte Carlo (AFQMC) calculations for the three-band Hubbard (Emery) model in the underdoped regime, in order to study the ground-state properties of Copper-Oxygen planes in the cuprates. Firstly, we find it important to focus on the magnetic and charge orders, and present results from generalized Hartree-Fock (GHF) calculations. The ground-state properties at the thermodynamic limit are challenging to pin down because of sensitivity to computational details, including the shapes and sizes of the supercells. We employ large-scale computations with various technical improvements to determine the orders within GHF. The ground state exhibits a rich phase diagram with hole doping as the charge transfer energy is varied, including ferromagnetic domain walls embedded in an antiferromagnetic background, spin spirals, and nematic order. Secondly, we use these results to guide and feed into exact methods by employing cutting-edge AFQMC techniques with a self-consistent gauge constraint in auxiliary-field space to control the sign problem, we reach supercells containing 500 atoms to capture collective modes in the charge and spin orders and characterize the behavior in the thermodynamic limit. The self-consistent scheme interfaced with generalized Hartree-Fock calculations allows high accuracy in AFQMC to resolve small energy scales, which is crucial for determining the complex candidate orders in such a system. We present results on the charge order, spin order, and localization properties as a function of charge-transfer energy.

TABLE OF CONTENTS

Acknowledgments iii

List of Tables iv

List of Figures v

CHAPTER

1 Introduction 2

2 A generalized Hartree-Fock study of the magnetic orders in the hole doped three-band Hubbard model: spin spirals, nematicity, and ferromagnetic domain walls 6

2.1 Model 8

2.2 Methods 10

2.3 Results 12

2.3.1 Magnetic Domain Walls (MDWs) 14

2.3.2 Spin Spirals 21

2.3.3 Intermediate Nematic Order 28

2.4 Summary and Discussion 30

3 An auxiliary-field quantum Monte Carlo study of the magnetic and charge orders in the ground state of the Emery model in the underdoped regime 33

3.1 Model 34

3.2 Methods 37

3.2.1 Self-Consistent Constraint 39

3.2.2 Extrapolation to Thermodynamic Limit 42

3.3 Results 43

3.3.1 Spin and Charge Orders 44
3.3.2 Momentum Distributions 55
3.3.3 Zhang-Rice Singlets and Localization 60
3.3.4 Electron-Hole Asymmetry 66
3.4 Summary and Discussion 69
4 Conclusion 74
Bibliography 78
Vita 87

ACKNOWLEDGMENTS

I would like to thank my advisor Professor Shiwei Zhang, whose guidance helped me develop both as a scientist and professionally.

I would also like to thank my collegues Ettore Vitali and Hao Shi, for sharing their knowledge and helping to guide me through my research.

I have also been privileged to work with and learn from many excellent members of the Condensed Matter Theory Group at William & Mary, including Professor Henry Krakauer, Professor Enrico Rossi, Dr. Mingpu Qin, Dr. Mario Motta, and Dr. Eric Walter as well as those at the Center for Computational Quantum Physics at the Flatiron Institute. These groups are exceptionally collaborative and friendly, and I am grateful to have worked in such pleasurable environments in my time in Williamsburg and New York.

I thank the Simons Foundation for support. Computing was performed using resources from XSEDE, which is supported by National Science Foundation grant number ACI-1053575, and the OLCF at ORNL which is supported by the Office of Science of the U.S. Department of Energy under contract no. DE-AC05- 00OR22725. I also acknowledge the High Performance Computing at William & Mary for their resources and help. The Flatiron Institute is a division of the Simons Foundation.

I would especially like to thank my family and my wife for their total support through my graduate studies.

LIST OF TABLES

2.1 Parameter values adopted in the present study. The parameters are obtained from [1] La_2CuO_4. We scan the value of $\Delta = \varepsilon_p - \varepsilon_d$ from 4.4 to 1.5 in our study. 10

3.1 Parameter values adopted in the present study. The parameters are obtained from La_2CuO_4 [1]. We study the value of $\Delta = \varepsilon_p - \varepsilon_d$ at 4.4 and 2.5. 36

3.2 Table of measured ground-state properties at doping $h = 1/8$, for different supercell sizes $M = L_x \times L_y$, at two different values of charge transfer energy Δ. All systems have PBC in both directions and have a pinning field applied in one row along the short direction with $h_{\text{pinn}} = 0.05$. The quantities are energy per site, d- and p- (sum of p_x and p_y) occupancies, percentage of the doped holes in the Cu d band, expectation values of the hopping matrix elements (kinetic energy components), and the interaction energy. 72

3.3 Table of measured ground-state total energy at doping $h = 1/8$, for different supercell sizes $M = L_x \times 16$, at two different values of charge transfer energy Δ. All supercells use the same systematic parameters as in Tab. 3.2. . . . 73

LIST OF FIGURES

2.1 (Color online) Schematic view of the CuO_2 planes in cuprates. Cu $3d_{x^2-y^2}$ orbitals are represented in blue, and O $2p_x$ and $2p_y$ orbitals in green. We use the reference frame defined by the two axes in the figure. The curve connectors represent the hopping, and the labels define the sign rule. . . . 9

2.2 (Color online) Different phases given by GHF as a function of the charge transfer energy Δ. The phase "boundaries" are meant as rough guides only. Each parameter regime is discussed in a subsection as indicated in the figure. 12

2.3 (Color online) Enlarged section of the magnetic and charge order in the ground state of a 24×30 lattice at $\Delta = 4.4\,eV$, $h = 1/8$, and tilted (diagonal) PBC. All spins are aligned or anti-aligned along one (arbitrary) direction in this state. The spin is plotted as red (positive) and blue (negative) arrows, with their length representing the magnitude. The excess hole density given by δn_{excess} is proportional to the size of the green circles. 13

2.4 (Color online) Ground-state energy per site, E/L, vs. supercell size along the diagonal $(1,1)$-direction for $4 \times L_{(1,1)}$ systems, for $\Delta = 4.4$, $h = 1/8$, tilted PBC. The inset shows the charge and spin order for the lowest E/L solution (corresponding to the 4×15 supercell, indicated by a circle). Magnetic and charge orders are plotted in the same manner as in Fig. 2.3. 16

2.5 (Color online) Momentum distribution in MDW state. The total momentum distribution are shown for spin up (left) and spin down (right) particles from the 24×30 supercell calculation of Fig. 2.3. The white dotted lines outline the Fermi surface of the non-interacting solution for the same system. . . 17

2.6 (Color online) Formation of MDWs from low doping, at $\Delta = 4.4$. The crosses represent the d-orbital on the copper atom and the horizontal and vertical dashes represent the p_x and p_y orbitals on the oxygen, respectively. The colored arrows are proportional to the spin (which are all oriented in one arbitrary direction as in Fig. 2.3), with blue representing positive spin and red representing negative. The green circles indicate where the extra charge (holes) localize, with their sizes proportional to the excess hole density on a given site (δn_{excess}). Tilted supercells with PBC are used in the calculations, with sizes: a) 6×6 (single hole doped); b) 6×6 (two hole doped); c) 6×12 (four hole doped). 19

2.7 (Color online) Charge and magnetic order for a periodic 32×36 supercell, with $\Delta = 1.5$ eV and $h = 1/8$. In (a), the spins (arrows) are plotted as a projection in the x-y plane. The total spin, $S_{tot}(\vec{r})$, on each site is given by the color gradient on the right. The spin on the O sites is negligible. The size of the green circles are proportional to the excess hole density from half-filling, $\delta n_{\text{excess}}(\vec{r})$. A small section of the lattice can be seen in (b), better highlighting the order. In (c) a 3-D plot of the staggered spin is shown along a line cut at $x = 0$, viewed along the y-axis. Blue arrows are the real 3D staggered spin and green dashed lines connect near neighbor spins to highlight spiral structure. 21

2.8 (Color online) Energy per site vs. lattice length along y for $4 \times L_y$ systems at $\Delta = 1.5$ eV, $h = 1/8$, PBC. 23

2.9 (Color online) Momentum distribution and nesting structure for spin spiral states. The left panel shows $n_\sigma(\mathbf{k})$ for $\sigma =\uparrow$ (left half) and $\downarrow$ (right half) in the 32×36 supercell in Fig. 2.7. The color scale is set to show nearly fully occupied momenta in white/red, nearly empty momenta in blue/black, and half occupied momenta around the Fermi surface in green. The white dotted lines outline the Fermi surface of the non-interacting solution for the same system. The right panel illustrates the nesting structure. Similar to the left panel, $n_\uparrow$ is on the left half and $n_\downarrow$ is on the right. The size of the circles is proportional to the occupation (magnitude of n_σ). The colors are to guide the eye around the Fermi surface. The black lines represent a (π, π) vector. The red lines connect complementary points $\mathbf{k}$ and $\mathbf{k}'$ between $n_\uparrow(\mathbf{k})$ and $n_\downarrow(\mathbf{k}')$ near the Fermi surfaces (see text). The blue lines show the shift $(\mathbf{k}' - \mathbf{k})$ [with respect to (π, π)], which defines the spiral wave vector. . . . 24

2.10 (Color online) Evolution of the magnetic and charge order from an AFM spiral to ferromagnetic domain walls. A 16×16 supercell is studied for varying values of the charge transfer energy, Δ, in the intermediate regime, at $h = 1/8$. The total staggered spins (arrows) are plotted as a projection in the x-y plane. The color of the arrow represents the angle between the spin on that site and a reference spin marked by the red "x". It can be thought of as a spin correlation and it runs from $(0, \pi)$. The spin on the O sites is negligible and omitted from the plot. The size of the green circles are proportional to the excess hole density from half-filling, $\delta n_{\text{excess}}(\vec{r})$. . . 27

3.1 (Color online) Schematic view of the CuO_2 planes in cuprates and illustration of the 3-band model. Cu $3d_{x^2-y^2}$ orbitals are represented in blue, and O $2p_x$ and $2p_y$ orbitals in green. We use the reference frame defined by the two axes in the figure. The curve connectors represent the hopping, and the labels define the sign rule. 35
3.2 (Color online) Plots of the S_z-component of the staggered spin vector along the line cut at $x = 0$, for three separate self–consistent calculations starting from varied initial states (SDW, Random, and Spiral) for $\Delta = 4.4$. The top panel is the QMC spin order for the 0^{th} iteration. The bottom panel shows the order is converged by the 3^{rd} iteration. The final order is a linear SDW with the majority of the spin vector in the S_z-direction, the same as the pinning field. 40
3.3 (Color online) Plot of the *staggered* spin vector, $(-1)^y S_x$, for $\Delta = 4.4$ along the line cut at $x = 0$ for a group of $6 \times L_y$ systems. A pinning field is applied at $y = 0$. The spin across the x-direction is antiferromagnetic. The spin order converges as $L_y \to \infty$. 42
3.4 (Color online) 2-D plot of the staggered spin vector, $(-1)^{x+y}\langle\hat{\mathbf{S}}(\mathbf{r})\rangle$, and charge density, $\langle\hat{n}(\mathbf{r})\rangle$, for $\Delta = 4.4$ and $h = 1/8$. The total staggered spins (arrows) are plotted as a projection in the x-z plane. The color of the arrow represents the angle between the spin on that site and an arbitrary reference spin. It can be thought of as a spin correlation and it runs from $(0, \pi)$. The spin on the O p-orbitals is negligible and omitted from the plot. The size of the circle is proportional to the density, with an overall background subtracted away. We neglect the first and last two rows to avoid the open boundaries and pinning field. 45
3.5 (Color online) Plot of the components of the staggered spin vector along the line cut at $x = 0$, for the system in Fig. 3.4. The spin across the x–direction is antiferromagnetic. The majority of the spin vector lies in the S_x-direction, the same as the pinning field. A stripe phase with antiferromagnetic domains is seen. 46
3.6 (Color online) Plot of the occupations on different sites along the line cut at $x = 0$, for the system in Fig. 3.4. The Cu d-band occupation is shown in the top panel, and the O p_x and p_y-bands are plotted in the bottom. The hole density wave is correlated with the spin order in Fig. 3.5, with higher density at the domain boundaries. A small asymmetry is seen between p_x and p_y sites. 47
3.7 (Color online) 2-D plot of the staggered spin vector and hole density, similar to Fig. 3.4, but for $\Delta = 2.5$. 49

3.8 (Color online) Plot of the components of the staggered spin vector along the line cut at $x = 0$, for the system in Fig. 3.7. The spin across the x–direction is antiferromagnetic. The majority of the spin vector lies in the S_x-direction, the same as the pinning field. A smooth antiferromagnetic spin-density wave is seen. 50
3.9 (Color online) Plot of the occupations on different sites along the line cut at $x = 0$, for the system in Fig. 3.7. The Cu d-band occupation is shown in the top panel, and the O p_x and p_y-bands are plotted in the bottom. Densities on the d sites show little fluctuation, while occupations on the p sites are correlated with the spin density in Fig. 3.8, with p_x sites showing a much larger response. 51
3.10 (Color online) 3D plot of the staggered spiral spin order for an 8×18 system, at $\Delta = 2.5$ and $h = 1/8$. The staggered spin is shown, projected in three-dimensions along a line-cut at $x = 0$ plotting along the y-direction. Along the x-direction, the order remains perfect AFM. 53
3.11 (Color online) (Top) Total momentum distributions for $\Delta = 4.4$ (left) and $\Delta = 2.5$ spiral state (right) in the 8×18 system at $h = 1/8$. For reference, the corresponding non-interacting Fermi surface is plotted as a white dashed line. (Bottom) Hole occupation, $n(\boldsymbol{k}) \equiv \frac{1}{2}(n_\uparrow(\boldsymbol{k})+n_\downarrow(\boldsymbol{k}))$, plotted along the path in momentum space $(0,0) \to (\pi,0) \to (\pi,\pi) \to (0,\pi) \to (0,0) \to (\pi,\pi)$ for the same systems in (a) along with their corresponding half-filled systems. For reference, the non-interacting system is plotted as the black dashed line. 56
3.12 (Color online) Band resolved hole occupation, $n(\boldsymbol{k}) \equiv \frac{1}{2}(n_\uparrow(\boldsymbol{k}) + n_\downarrow(\boldsymbol{k}))$, plotted along the path in momentum space $(0,0) \to (\pi,0) \to (\pi,\pi) \to (0,\pi) \to (0,0) \to (\pi,\pi)$ for the same systems in Fig. 3.11 (closed symbols) along with their corresponding half-filled systems (open symbols). For reference, the non-interacting system is plotted as the black dashed line. . . 57
3.13 (Color online) The difference between the spin-up and spin-down momentum distributions in the spiral state at $\Delta = 2.5$ with $h = 1/8$. To guide the eye to complimentary nesting points on the Fermi surface, for $k_x < 0$, we plot $n_\uparrow(\boldsymbol{k}) - n_\downarrow(\boldsymbol{k})$, and for $k_x > 0$, we plot $n_\downarrow(\boldsymbol{k}) - n_\uparrow(\boldsymbol{k})$. We plot the nesting vector, q, in red, $Q = (\pi,\pi)$ in white, and $\Delta q = q - Q$ in blue. . . 59
3.14 (Color online) Zhang-Rice singlet density for both $\Delta = 4.4$ and 2.5. The results are plotted along a line cut $x = 0$, alongside the Oxygen p_x and p_y-orbital densities for both doped ($h = 1/8$) and half–filled ($h = 0$) systems. Plots are taken along a line cut at $x = 0$. Note: the overall scale is the same for both values of Δ; however there is an overall shift. 61

3.15 (Color online) Plot of the (y, y)–component of the QMT as a function of L_y. At $\Delta = 4.4$, the value of the QMT is saturated for large lattice sizes suggesting an insulating state. For both $\Delta = 2.5, 4.4$, the QMT appears to be still increasing suggesting conducting states. 64
3.16 (Color online) 2-D plot of the x-component of the total spin vector, $\langle \hat{\mathbf{S}}_x(\mathbf{r}) \rangle$, and charge density, $\langle \hat{n}(\mathbf{r}) \rangle$, for $\Delta = 4.4$ for both (a) a hole doped system, $h = 1/8$, and (b) an electron doped system $h = -1/8$. The spins (arrows) are plotted as a projection in the x- plane. The color of the arrow represents the directionality of the spin in the x-direction, blue being positive and red negative, to highlight AFM order. The spin on the O p-orbitals is negligible and omitted from the plot. The size of the green circles are proportional to the hole density. To highlight density waves, we plot the color of the circles scaled to the maximum and minimum hole densities for the respective systems. We neglect the first and last two rows to avoid effects at the open boundaries and pinning field. 67
3.17 (Color online) Plot of the occupations on different sites along the line cut at $x = 0$, for the systems in Fig. 3.16. The Cu d-band occupation is shown in the top panel, and the O p_x and p_y-bands are plotted in the bottom. Closed symbols represent the hole doped system ($h = 1/8$) and open symbols represent the electron doped system ($h = -1/8$). 68

COMPETING AND COOPERATING ORDERS IN THE THREE-BAND HUBBARD MODEL: A COMPREHENSIVE QUANTUM MONTE CARLO AND GENERALIZED HARTREE-FOCK STUDY

CHAPTER 1

Introduction

Significant progress has been made in the study of a variety of strongly correlated electron systems[2, 3, 4, 5, 6, 7, 8, 9, 10, 11, 12, 13, 14, 15]. However, despite more than thirty years of theoretical and experimental studies, understanding high–temperature superconductivity has remained a very difficult problem. Recent advances in computing technology and computational methods are providing new opportunities to address important questions with more powerful and more systematic computational studies.

It is widely believed that the superconducting order of the cuprates arises from a physical mechanism in the quasi–two–dimensional planes hosting the copper and oxygen atoms[16]. Other layers of the material play the role of charge reservoirs, which can be used to dope the copper–oxide planes by adding or removing electrons (holes). The experimental evidence indicates that, when no doping is present, in the parent compounds, the stable phase is an insulating antiferromagnet[17]. With doping, this order rapidly disappears, giving rise to a rich, complicated phase diagram with respect to doping and temperature in which different spin and charge orders appear to coexist, either cooperating or competing[18, 19]. From the theoretical point of view, the complex electronic structure

of these materials makes a fully *ab initio* many-body computation a formidable task, in particular since the characterization of the phases requires a detailed study of the bulk limit. Because of this, a main focal point of the theoretical research is creating minimal models to study the order in the copper–oxide plane.

The majority of efforts to model this problem have focused on the Hubbard Hamiltonian[20]. This model relies on the Zhang–Rice singlet notion[21] that allows a reduction of the degrees of freedom by treating the oxygen sites implicitly in the mathematical description. A variety of accurate numerical results (see for example, Refs. [22, 23, 24]) have been obtained for the one-band Hubbard model, which indicate the existence of certain spin and charge orders observed in experiments on the real materials, and, perhaps more importantly, the close and delicate competition between different orders; however, there are strong indications that, at least at zero–temperature, the simplest Hubbard model does not display a superconducting ground state [25] in the relevant region in parameter space.

Recent X-ray scattering experiments and nuclear magnetic resonance experiments indicate that the oxygen p-bands are involved in spin and charge density wave states [26, 27, 28, 29, 30]. This suggests one direction to improve the model may be to include the oxygen p-bands explicitly as non-trivial hole carriers. With recent advances in computational methodologies, several sophisticated many-body approaches can now go well beyond the minimal Hubbard model to study the more realistic three-band Hubbard model, or Emery model[16]. This model explicitly includes copper $3d_{x^2-y^2}$ and the oxygen $2p_x$ and $2p_y$ orbitals. The model Hamiltonian contains several parameters, including the charge transfer energy, hopping amplitudes and on-site repulsion energies for the different bands.

In principle the Hamiltonian parameters can be computed from approximate *ab initio* approaches. However their actual determination is subtle. In particular the value of the charge transfer energy, which carries the physical meaning of the energy required to move a hole from a copper $d_{x^2-y^2}$ orbital to a oxygen p orbital, Δ, can be affected by double–

counting issues[31] in the computation. In addition, the value of the charge transfer energy varies across the different families of the cuprates, and it controls the average electron occupation around copper and oxygen atoms. There are indications that this occupation is anti–correlated with the critical temperature[32, 27, 28, 33], which makes Δ a crucial parameter in the Emery model. From a recent auxiliary-field quantum Monte Carlo study of the model at half-filling [34], we have seen that the properties of the ground state of the model vary fundamentally with Δ, showing a quantum phase transition transition from an insulating antiferromagnet to a non–magnetic metal.

Away from half-filling, there have been many computational studies addressing the behavior of the Emery model using different methodologies, including exact diagonalization of small clusters[35], random phase approximation [36], Density Matrix Renormalization Group [10], quantum Monte Carlo[37, 38, 39, 40], and embedding methodologies (including dynamical mean field theory and cluster extensions, and density matrix embedding theory) [41, 42, 43, 44]. These calculations have revealed a great deal about the properties of the model. Many similarities are seen between this model and the one-band Hubbard model, including the presence of strong magnetic correlations away from half-filling and their delicate balance or competition with superconductivity. Even so, the numerical evidence has been inconclusive on several key issues, including the nature of the true ground state caused by various computational limitations, which include the accuracy of the many-body methods and the reliability of reaching the thermodynamic and zero-temperature limits. This is not surprising, given that even in the one-band model some of these issues are only now being resolved using combinations of the latest advances in computational methodologies.

In particular, the above mentioned limitations make it difficult to explore long-range orders, which are expected to play a crucial role in the determination of the phase diagram of the model. In this regard, in a recent study, Huang et al[45] found the presence of

fluctuating stripes in the model at high temperature. We have recently carried out a Generalized Hartree–Fock study[46] (discussed in this work) of the magnetic and charge orders in this model, focusing on the ground-state phase diagram and its dependence on Δ. The results indicate the existence of long-wavelength collective modes as was seen in the one-band Hubbard model [47, 48, 49]. In addition to stripes, they also suggested possible additional orders as Δ is varied, such as spirals and magnetic domains. Such states are extremely challenging to detect and establish, because of the requirements on both accuracy and robustness of the underlying many-body method and the capability to reach large system sizes to approach the thermodynamic limit.

The focus of this dissertation is to perform a comprehensive study of the magnetic and charge orders that arise in the Emery model as a function of the charge-transfer energy in the thermodynamic limit and to compare and contrast results with the one-band Hamiltonian and experimental results. We use two main numerical techniques: generalized Hartree-Fock (GHF) and auxiliary-field quantum Monte Carlo (AFQMC). These two techniques can be used in tandem, in an iterative self-consistent scheme to determine the true ground state of the model.

The following chapters are each a self-contained study. Firstly, in Chapter 2, we perform a comprehensive GHF study of the Emery model as a function on the charge-transfer energy as well as doping. This is the first study of its kind, and it is crucial to see the magnetic and charge order phase diagram of the model. In Chapter 3, we use the candidate states found in Chapter 2 as trial wavefunctions in the self-consistent AFQMC method to target the true ground state of the model. We focus on the system at 1/8 doping and at two values of the charge transfer energy: $\Delta = 4.4$ which corresponds to a Mott insulator at half–filling and $\Delta = 2.5$ which corresponds to a non–magnetic metal at half–filling. Chapter 4 provides a summary and outlook.

CHAPTER 2

A generalized Hartree-Fock study of the magnetic orders in the hole doped three-band Hubbard model: spin spirals, nematicity, and ferromagnetic domain walls

Since the phase diagram in the underdoped regime is intrinsically complex, with several cooperating and competing phases separated by small energy scales, it is crucial to be able to study very large lattices with different geometries and boundary conditions in order to rule out spurious finite size effects. A useful illustration is found in the one-band Hubbard model, where the magnetic and charge orders in the ground state exhibit long wavelength collective modes which are extremely delicate and sensitive to finite-size effects [50, 48, 47]. The task to systematically determine such orders is especially challenging for

many-body approaches, with high computational costs that tend to make it particularly difficult to reliably reach the thermodynamic limit and scan multiple parameters. Mean-field calculations can serve as a valuable guide in this regard. In the one-band Hubbard model, unrestricted Hartree-Fock solutions were found to capture much of the magnetic phase diagram [51], albeit with parameter values that can differ [22, 47], reflecting the tendency of mean-field theory to exaggerate order.

Although mean-field studies have been performed on the three-band Hubbard model[8, 52, 53, 54, 55, 56, 57], a systematic determination of the magnetic and charge properties within a general mean-field framework is, to our knowledge, still not available. This is the goal of the present work. We employ a generalized Hartree-Fock (GHF) approach which allows non-colinear magnetic orders. As described below, we find a rich ground-state phase diagram, with some phases hereforeto not seen in models for cuprates. The phase diagram of the three–band model is much more complex than that of the single-band Hubbard model. Based on the lessons from the single-band model, these phases should serve as very plausible candidate zero-temperature states of the model, possibly with modified parameters (e.g., reduced effective repulsion). The results identify several phases which are potentially important to the physics of the CuO_2 planes in cuprate materials. Our results also provide guidance on finite-size and other subtleties for many-body calculations. The mean-field solution can serve as possible trial wave functions for more advanced quantum Monte Carlo (QMC) investigations.

The rest of the chapter is organized as follows. In Sec. 2.1 we introduce the three-band Hubbard, or Emery, model. In Sec. 2.2, we outline the GHF method and explain the need, and our strategies, for scanning the parameter space. Sec. 2.3 presents our resultsin which three distict phases are observed as Δ is varied: 2.3.1. magnetic domain walls, 2.3.2. spin spirals, and 2.3.3. nematic phases in the intermediate Δ region. We further discuss the results and conclude in Sec. 2.4.

2.1 Model

The Emery model includes the Cu $3d_{x^2-y^2}$ orbital and the O $2p_x$ and $2p_y$ orbitals in the description of the cuprates. In Fig. 2.1, a schematic representation of the CuO_2 plane is given to help visualize the model. The Hamiltonian is

$$\begin{aligned}\hat{H} = &\varepsilon_d \sum_{i,\sigma} \hat{d}^\dagger_{i,\sigma}\hat{d}_{i,\sigma} + \varepsilon_p \sum_{j,\sigma} \hat{p}^\dagger_{j,\sigma}\hat{p}_{j,\sigma} + \\ &\sum_{<i,j>,\sigma} t^{ij}_{pd}\left(\hat{d}^\dagger_{i,\sigma}\hat{p}_{j,\sigma} + h.c\right) + \sum_{<j,k>,\sigma} t^{jk}_{pp}\left(\hat{p}^\dagger_{j,\sigma}\hat{p}_{k,\sigma} + h.c\right) \\ &+ U_d \sum_i \hat{d}^\dagger_{i,\uparrow}\hat{d}_{i,\uparrow}\hat{d}^\dagger_{i,\downarrow}\hat{d}_{i,\downarrow} + U_p \sum_j \hat{p}^\dagger_{j,\uparrow}\hat{p}_{j,\uparrow}\hat{p}^\dagger_{j,\downarrow}\hat{p}_{j,\downarrow}\,.\end{aligned} \tag{2.1}$$

In Eq. (2.1), i runs over the sites $\vec{r}_{\mathrm{Cu}}$ of a square lattice $\mathbb{Z}^2$ defined by the positions of the Cu atoms. The labels j and k run over the positions of the O atoms, shifted with respect to the Cu sites, $\vec{r}_{\mathrm{O}_x} = \vec{r}_{\mathrm{Cu}} + 0.5\,\hat{x}$ for the $2p_x$ orbitals, and $\vec{r}_{\mathrm{O}_y} = \vec{r}_{\mathrm{Cu}} + 0.5\,\hat{y}$ for the $2p_y$ orbitals. This model is formulated in terms of holes rather than electrons: for example, the operator $\hat{d}^\dagger_{i,\sigma}$ creates a hole on the $3d_{x^2-y^2}$ orbital at site i with spin $\sigma = \uparrow, \downarrow$. The first two terms in the Hamiltonian contain the orbital energies, which define the charge-transfer energy parameter $\Delta = \varepsilon_p - \varepsilon_d$, the energy needed for a hole to move from a Cu $3d_{x^2-y^2}$ orbital to an O p orbital. The next two terms describe hopping between orbitals; the hopping amplitudes t^{ij}_{pd} and t^{jk}_{pp} are expressed in terms of two parameters, t_{pd} and t_{pp}, and the dependence on the sites is simply a sign factor, as depicted in Fig. 2.1. Finally, the last two terms represent the on-site repulsion energies, namely double-occupancy penalties similar to those in the one–band Hubbard model. We neglect Coulomb interactions beyond the on-site terms.

As mentioned in the introduction, we study the properties of the model as a function of the charge transfer energy Δ. Our starting point is an *ab intio* set [1] of parameters

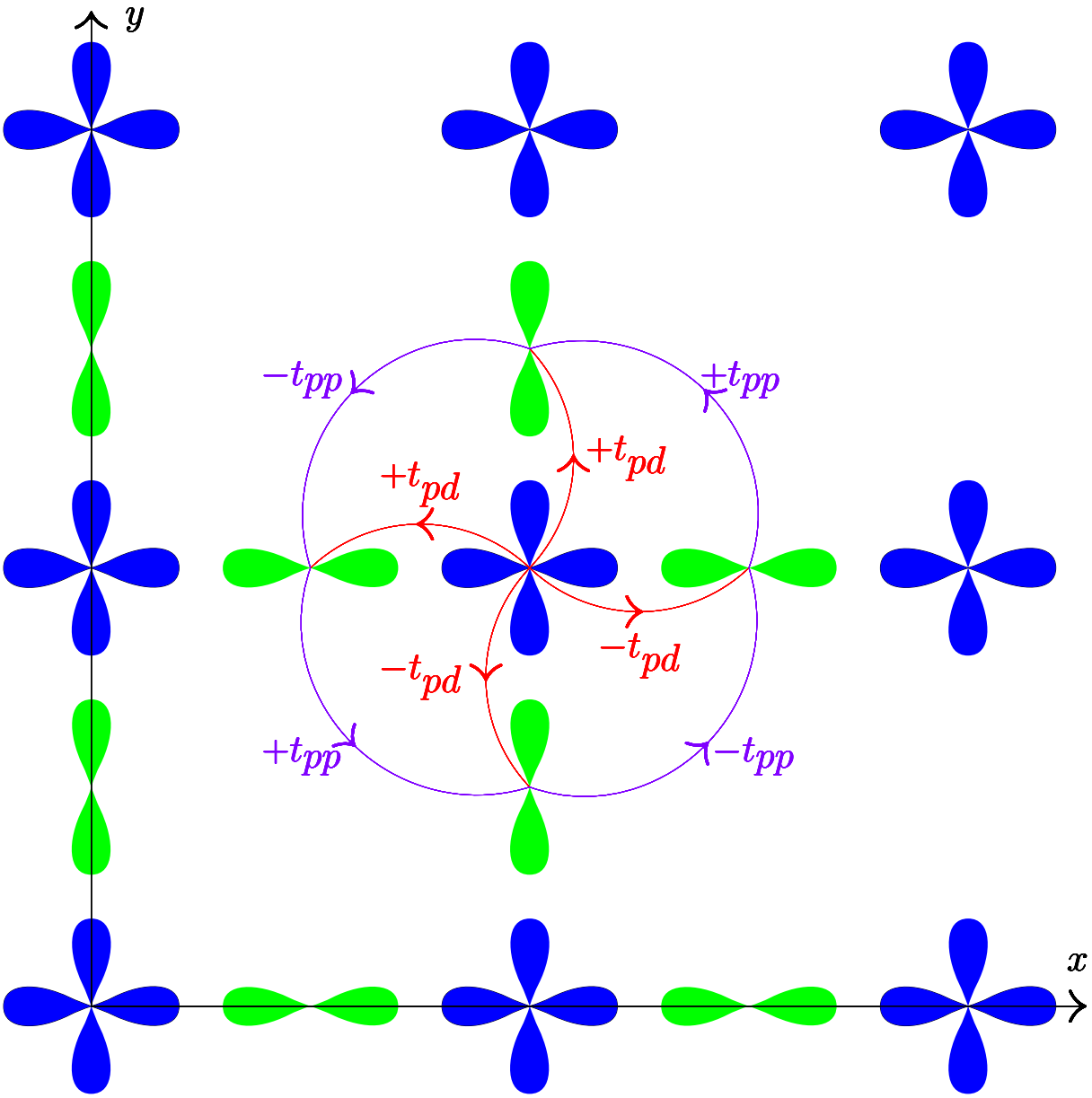

FIG. 2.1: (Color online) Schematic view of the CuO_2 planes in cuprates. Cu $3d_{x^2-y^2}$ orbitals are represented in blue, and O $2p_x$ and $2p_y$ orbitals in green. We use the reference frame defined by the two axes in the figure. The curve connectors represent the hopping, and the labels define the sign rule.

Parameter	U_d	U_p	ε_d	ε_p	t_{pd}	t_{pp}
Value (eV)	8.4	2.0	-7.6	-3.2	1.2	0.7

TABLE 2.1: Parameter values adopted in the present study. The parameters are obtained from [1] La_2CuO_4. We scan the value of $\Delta = \varepsilon_p - \varepsilon_d$ from 4.4 to 1.5 in our study.

obtained for La_2CuO_4, the parent compound of the lanthanum based family of cuprates. The parameter values are listed in Table 2.1. This set corresponds to a charge transfer energy $\Delta = 4.4$ eV. To correct for possible double counting issues [31] would imply a considerable reduction of this value to $\Delta \sim 1.5$ eV. In our calculations we scan the value of Δ in this range. As we will show below, the variation of Δ can dramatically affect the physical properties of the model.

2.2 Methods

In order to study the Hamiltonian in Eq. (2.1), we use a fully self-consistent mean-field approach, where the two-body operators are decoupled as follows:

$$\begin{aligned} &\hat{d}^\dagger_{i,\uparrow}\hat{d}_{i,\uparrow}\hat{d}^\dagger_{i,\downarrow}\hat{d}_{i,\downarrow} \simeq \text{const} \\ &+ \langle \hat{d}^\dagger_{i,\uparrow}\hat{d}_{i,\uparrow}\rangle\, \hat{d}^\dagger_{i,\downarrow}\hat{d}_{i,\downarrow} + \langle \hat{d}^\dagger_{i,\downarrow}\hat{d}_{i,\downarrow}\rangle\, \hat{d}^\dagger_{i,\uparrow}\hat{d}_{i,\uparrow} \\ &- \langle \hat{d}^\dagger_{i,\uparrow}\hat{d}_{i,\downarrow}\rangle\, \hat{d}^\dagger_{i,\downarrow}\hat{d}_{i,\uparrow} - \langle \hat{d}^\dagger_{i,\downarrow}\hat{d}_{i,\uparrow}\rangle\, \hat{d}^\dagger_{i,\uparrow}\hat{d}_{i,\downarrow}\,. \end{aligned} \tag{2.2}$$

The terms in brackets, densities and spin densities, are obtained self-consistently by a diagonalization of a one-body Hamiltonian. We use a generalized Hartree-Fock approach, which constrains only the total number of particles (holes), N.

Since we are interested in the bulk physics of the model, we perform calculations on large lattices, Cu_LO_{2L} hosting N holes corresponding to a doping of $h = N/L - 1$. In

order to minimize size effects, which is important if long-range charge or magnetic orders are present, we explore different choices of geometries (square and rectangular supercells) and boundary conditions while keeping h fixed. More precisely we consider both periodic boundary conditions (PBC) and twist boundary conditions (TBC) with random twist angles. We examine both "regular" and tilted supercells. The former has basis vectors along the coordinates axes depicted in Fig. 2.1, while the latter has basis vectors along the two diagonal directions, i.e., those obtained from rotating the x- and y-axes by $\pi/4$. The tilted supercell requires considering unit cells containing two Copper atoms and four Oxygen atoms and is meant to capture orders along the diagonal direction. In both cases, we will use the notation $L_a \times L_b = L$ to denote the dimension of our supercell, with a (b) being either x (y) or the two diagonal directions. We study systems with increasing L to improve the extrapolation to the bulk limit.

For given lattice and number of holes, the GHF solution will be a Slater determinant of spin orbitals:

$$\begin{aligned} |\Psi\rangle &= \prod_{n=1}^{N} \hat{\phi}_n^\dagger \, |0\rangle \\ \hat{\phi}_n^\dagger &= \sum_{i=1}^{L} \sum_{\sigma=\uparrow,\downarrow} \sum_{\alpha=d,p_x,p_y} u_n(i,\alpha,\sigma) \, \hat{\alpha}_{i,\sigma}^\dagger \end{aligned} \tag{2.3}$$

that minimizes the energy $\langle \Psi \,|\, \hat{H} \,|\, \Psi \rangle$ within the manifold of Slater determinants. From the wave function $|\Psi\rangle$, any ground-state property of the model can be computed. The GHF approach allows the number of the spin-$\uparrow$ and spin-$\downarrow$ particles to fluctuate and non-colinear spin orders to develop. No particular order is assumed at the beginning of the calculation. The self-consistent procedure can lead to a local minimum. In our calculations we frequently introduce random noise in the orders and anneal the solution to help the mean-field procedure locate the order corresponding to the global minimum in energy.

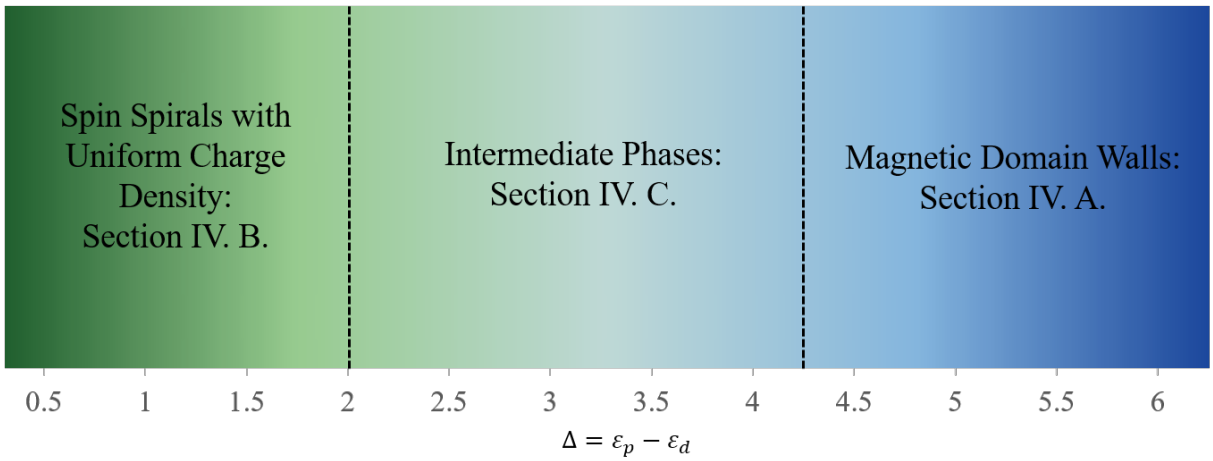

FIG. 2.2: (Color online) Different phases given by GHF as a function of the charge transfer energy Δ. The phase "boundaries" are meant as rough guides only. Each parameter regime is discussed in a subsection as indicated in the figure.

2.3 Results

Most of our calculations are at optimal doping $h = 1/8$, using the hopping and on-site interaction parameters given in Table 2.1, while scanning the charge-transfer energy Δ, which represents the energy needed to move a hole from a Copper atom to an Oxygen atom. The parameter Δ, via its interplay with hopping amplitudes and on-site Coulomb repulsion, has a direct consequence on the average density of holes at the Cu and O sites: n_d and n_p, respectively. Magnetic resonance experiments [28] are now able to detect the values of n_d and n_p for the different families of cuprates. These results indicate that smaller differences $(n_d - n_p)$, i.e. smaller values of Δ, correspond to higher critical temperature and thus higher superfluid fraction. The anticorrelation between Δ and the critical temperature is also seen from scanning tunneling microscopy [32]. Cluster dynamical mean field theory calculations indicate [43] similar tendencies. Thus a systematic investigation of the dependence of the ground-state properties on Δ is especially important and timely.

We find a rich and complex set of possible ground-state magnetic and charge orders as Δ is scanned. At optimal hole doping of $h = 1/8$ and with hopping and on-site

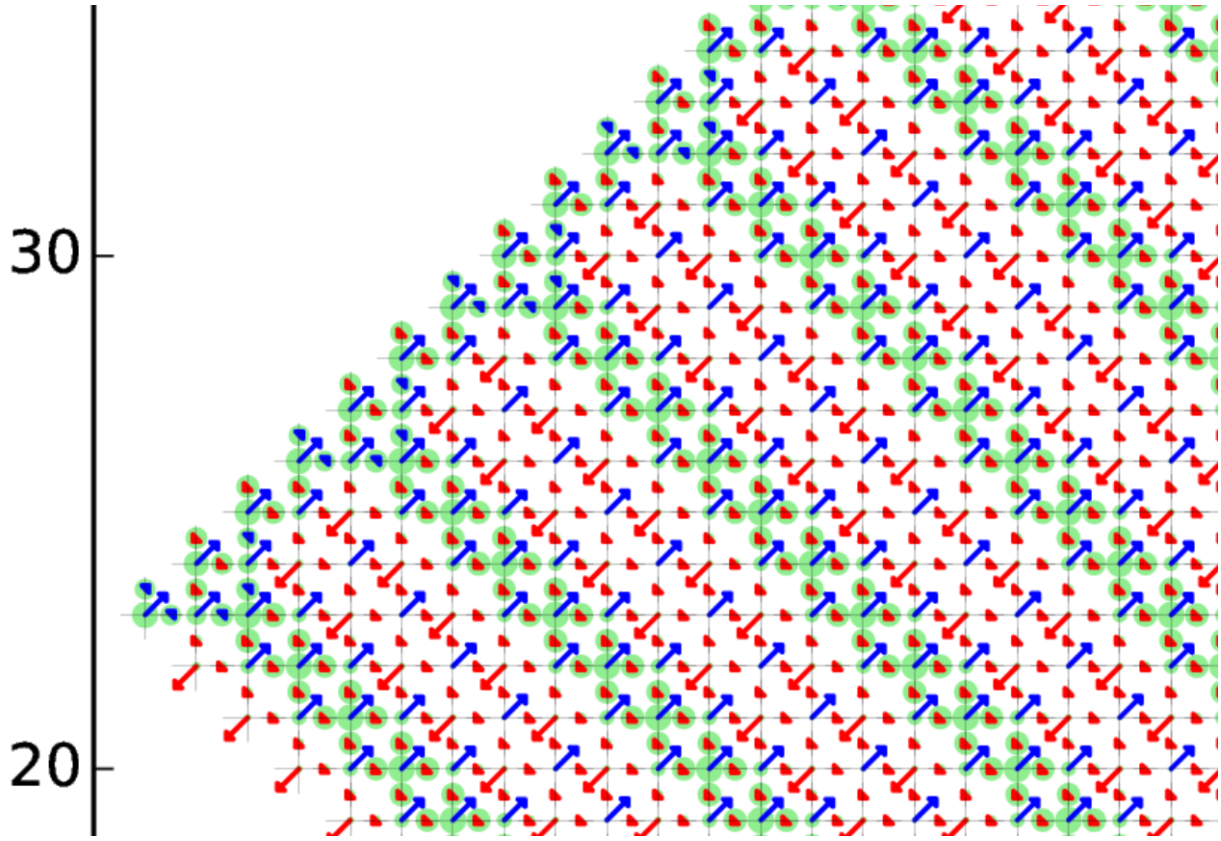

FIG. 2.3: (Color online) Enlarged section of the magnetic and charge order in the ground state of a 24×30 lattice at $\Delta = 4.4\,eV$, $h = 1/8$, and tilted (diagonal) PBC. All spins are aligned or anti-aligned along one (arbitrary) direction in this state. The spin is plotted as red (positive) and blue (negative) arrows, with their length representing the magnitude. The excess hole density given by δn_{excess} is proportional to the size of the green circles.

repulsion parameters listed in Table 2.1, three different regimes are encountered with GHF as Δ is varied: magnetic domain walls at high Δ ($\sim 4.4\,\text{eV}$), spiral spin-density waves at low Δ ($\sim 1.5\,\text{eV}$), and nematic intermediate phases in between. The gradient plot in Fig. 2.2 shows the parameter range scanned, and these different regimes, which are described separately in the following three subsections.

2.3.1 Magnetic Domain Walls (MDWs)

Spin and Charge Order at Doping h = 1/8

We start from the largest value of the charge-transfer energy, $\Delta = 4.4\ eV$. At half-filling, the system is antiferromagnetic (AFM) and the densities of holes on the Copper and Oxygen sites are $n_d \approx 0.735$ and $n_p \approx 0.133$, respectively. At optimal doping of $h = 1/8$, the system exhibits diagonal magnetic domain walls (MDW) in the ground state. In Fig. 2.3 we show the spin and charge densities, using a large supercell, 24×30, with tilted periodic boundary conditions, i.e., $Cu_{1440}O_{2880}$, in order to determine the order. We find that the spins $(S_x(\vec{r}), S_y(\vec{r}), S_z(\vec{r}))$ in the GHF ground state are, to very good accuracy, aligned (anti-aligned) in one arbitrary direction. In the plot we use arrows to represent the spin density, and circles to represent the excess hole density, which we define as:

$$\delta n_{\text{excess}}(\vec{r}) = n_{\text{doped}}(\vec{r}) - n_0(\vec{r})\,, \tag{2.4}$$

where $n_0(\vec{r})$ is the density at half-filling.

From the plot in Fig. 2.3, we clearly see an array of lines of increased hole density, with $n_d \approx 0.842$, i.e., extra occupation on the order of $\delta n_{\text{excess}} \sim 0.1$, forming a $\pi/4$ angle with respect to the CuO bonds, superimposed to the AFM background. On the Cu d-sites within these domain wall lines, there is a near perfect spin flip ($\vec{S} \to -\vec{S}$) creating local ferromagnetic order. These d-sites are surrounded by four O p-sites which also have increased hole occupancy, $n_p \approx 0.225$. The doped holes are concentrated on these lines, with only slight "spill-over" to the adjacent AFM lines. These MDW structures are spaced out and embedded in the rest of the system which is kept essentially at the AFM state found at half-filling. The spin on the O p-sites, negligible at half–filling, remains very small but does show noticible increase ($\mathcal{O}(10^{-3})$). The small spins on the p-sites are all aligned

in the direction opposite to that of the ferromagnetic line defects on the Cu sites (except near the connecting 2-D structures).

The phase of MDWs immersed in an AFM background is suggestive of the stripes found experimentally by Tranquada et. al. [3]. However, unlike the stripe states, these domain walls have an overall spin, and the AFM domains separated by the MDWs appear to be in phase. Compared to theoretical studies, the MDW state is reminiscent to the charged Bloch domain lines found in the seminal paper of Zaanen & Gunnarsson[8] which studied the SSH model in 2–D, in that excess charge tends to localize on straight lines; however, in the MDW state the domain lines are diagonal, ferromagnetic, and do not induce a phase change across the domain line. Compared to the spiral state found by Assaad [52] at $U = 6$ and small doping, the MDW state is similar in that they both align along the diagonal (1,1)-direction. However, they differ in their properties. The MDW, in some sense, may combine the presence of AFM spin modulations with ferromagnetism as we will further discuss in 2.3.3.

Our calculations indicate that the MDWs tend to align periodically in one-dimension (1D) along the diagonal line, though there are some two-dimensional features. We cannot rule out completely that these connecting structures arise solely from commensurability or boundary effects, since we have yet to find a perfectly commensurate lattice that only contains 1D structures. However, a clear preference for a periodicity in spacing is seen in the MDWs. To quantify this feature, we scan long, rectangular lattices. By varying the lattice in a single diagonal direction, minima in the energy/site vs. length will show which geometries are preferred for the domain walls. Fig. 2.4 shows an example for $4 \times L_{(1,1)}$ lattices. A regular pattern is evident, with minima at $L_{(1,1)} = 6, 9, 12$, and 15. Since there are two copper atoms per unit cell, this corresponds to 12, 18, 24, and 30 diagonal copper planes. This suggests that, at $h = 1/8$, the MDWs prefer lattices that allow regular spacing of 6 copper planes between the domain walls.

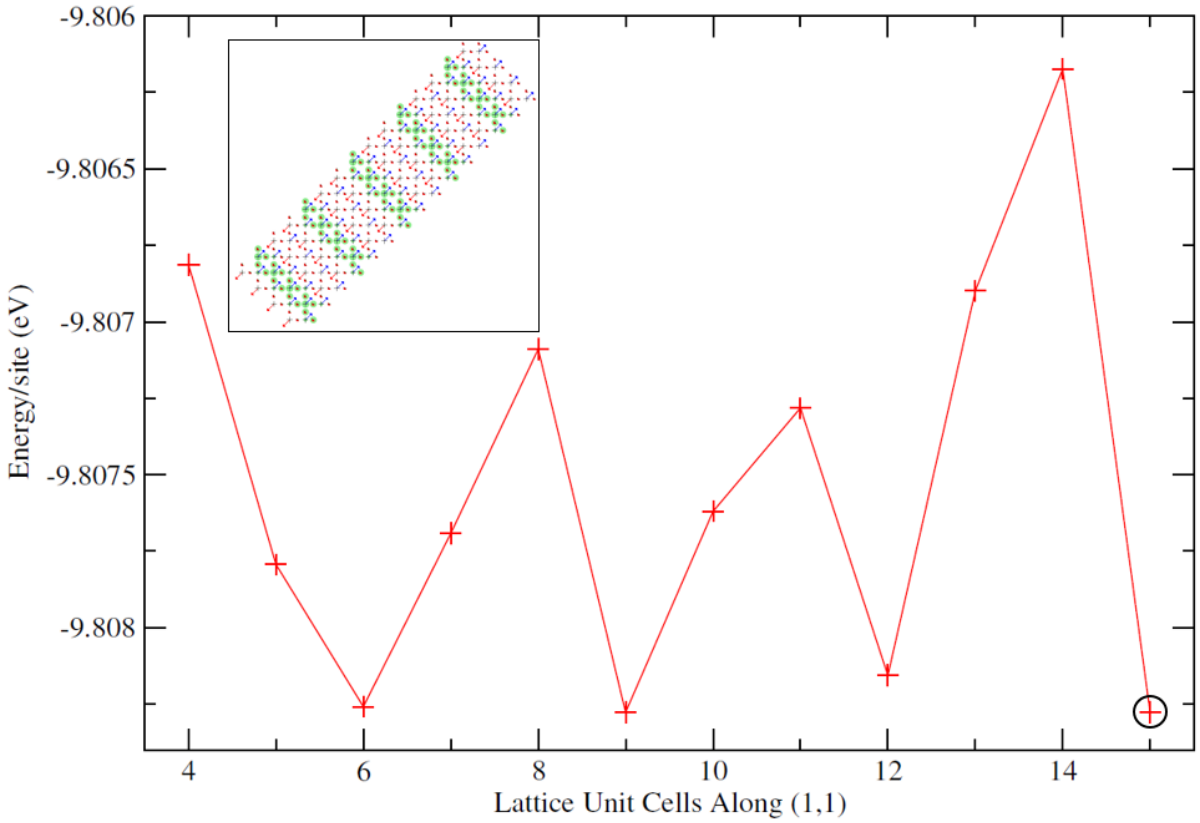

FIG. 2.4: (Color online) Ground-state energy per site, E/L, vs. supercell size along the diagonal $(1,1)$-direction for $4 \times L_{(1,1)}$ systems, for $\Delta = 4.4$, $h = 1/8$, tilted PBC. The inset shows the charge and spin order for the lowest E/L solution (corresponding to the 4×15 supercell, indicated by a circle). Magnetic and charge orders are plotted in the same manner as in Fig. 2.3.

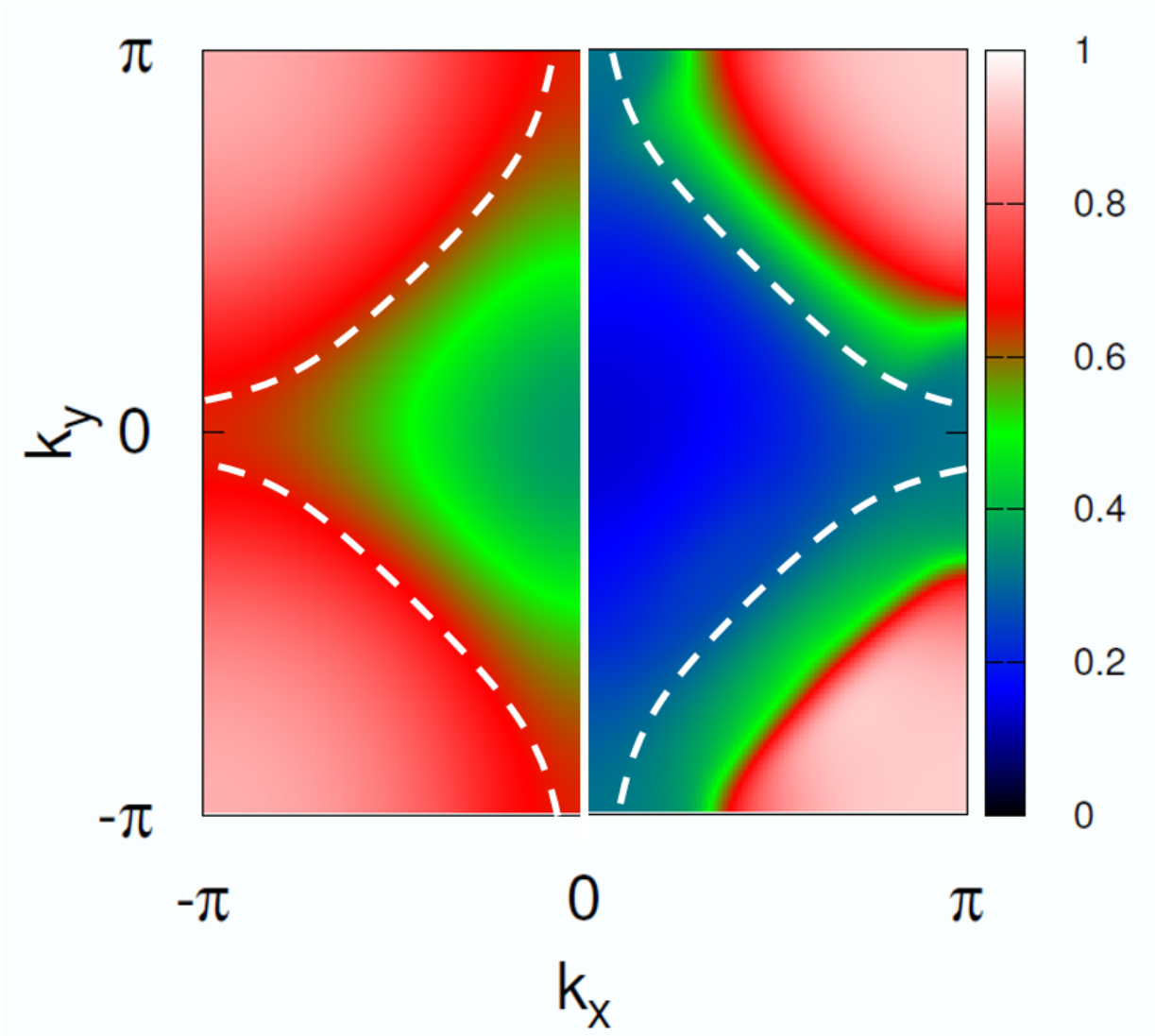

FIG. 2.5: (Color online) Momentum distribution in MDW state. The total momentum distribution are shown for spin up (left) and spin down (right) particles from the 24×30 supercell calculation of Fig. 2.3. The white dotted lines outline the Fermi surface of the non-interacting solution for the same system.

Fig. 2.5 depicts the total spin-↑ and spin-↓ momentum distributions $n_\sigma(\mathbf{k}) = \langle\Psi|\hat{d}^\dagger_{\mathbf{k},\sigma}\hat{d}_{\mathbf{k},\sigma} + \hat{p}^\dagger_{\mathbf{k},\sigma}\hat{p}_{\mathbf{k},\sigma}|\Psi\rangle$, where $\hat{p}_{\mathbf{k},\sigma}$ is the Fourier transform of $\hat{p}_{j,\sigma}$ with j running over both sets of basis vectors $\vec{r}_{\mathrm{O}_x}$ and $\vec{r}_{\mathrm{O}_y}$, and similarly $\hat{d}_{\mathbf{k},\sigma}$ is the Fourier transform of $\hat{d}_{i,\sigma}$. We see the spin imbalance present in the system, as well as the tendency to develop diagonal modulations. Symmetries about the k_x or k_y axes are both broken. In the figure, the left half shows $n_\uparrow(\mathbf{k})$ while the right half shows $n_\downarrow(\mathbf{k})$. The missing portions of the momentum distributions can be constructed by reflection with respect to the origin, $n_\sigma(-\mathbf{k}) = n_\sigma(\mathbf{k})$ In addition to the broken spin symmetry, we see significant re-construction of the Fermi surface to create nesting which produces the modulated MDW structures. We comment in passing that spin imbalance with attractive interactions, for example in Fermi atomic gases on an optical lattice, are expected to have non-trivial modulated pairing states. It would be interesting to investigate possible relation between the spin imbalance seen here and potential non-trivial pair density wave states, using more advanced many-body methods in future studies.

Formation of Domain Walls from Low Doping

To probe the mechanism that leads to the formation of the MDW within the AFM background, we scan lightly doped systems. The plots in Fig. 2.6 illustrate how a small number of holes accumulate and nucleate. For single hole systems, the calculations show that the extra hole (green circle) localizes around a randomly chosen copper site in a periodic supercell. There is some smearing over to local O sites as well as nearest neighbor copper sites. The system has perfect AFM order on the copper atoms, except for the site where the hole localizes. On that site, there is local ferromagnetic order with neighboring copper sites. The direction of the spin on the neighboring p-bands oppose this ferromagnetic order. This behavior is very robust, and is seen in all our calculations with a single hole under PBC, for all lattice sizes and geometries. We call this local magnetic and charge

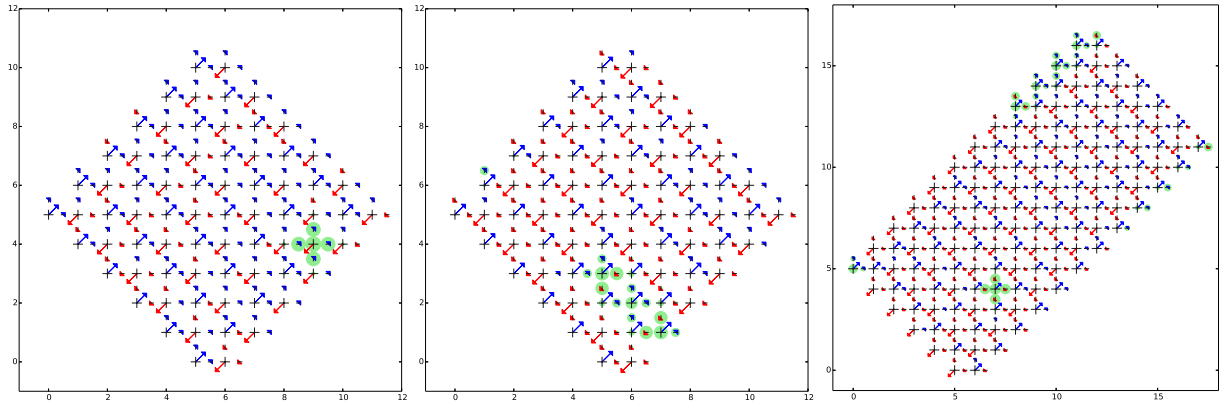

(a) h=1/72 (b) h=1/36 (c) h=1/36

FIG. 2.6: (Color online) Formation of MDWs from low doping, at $\Delta = 4.4$. The crosses represent the d-orbital on the copper atom and the horizontal and vertical dashes represent the p_x and p_y orbitals on the oxygen, respectively. The colored arrows are proportional to the spin (which are all oriented in one arbitrary direction as in Fig. 2.3), with blue representing positive spin and red representing negative. The green circles indicate where the extra charge (holes) localize, with their sizes proportional to the excess hole density on a given site (δn_{excess}). Tilted supercells with PBC are used in the calculations, with sizes: a) 6×6 (single hole doped); b) 6×6 (two hole doped); c) 6×12 (four hole doped).

order a spin flip defect.

We interpret the spin flip defect, in which the extra hole density is accompanied by an overall spin flip on the corresponding Cu site, as a way to gain exchange energy. The density increase within the ferromagnetic defects (see Sec. 2.3.1) makes the total density of the CuO_2 unit cell well above unity (indeed higher than $1 + h$) along the MDW. This renders the AFM state, which avoids double occupancy of the d-sites, less effective. The system then chooses to flip the spin on the d-site and introduce local ferromagnetic order on the Cu sublattice. In order for this exchange energy gain to be efficient, the excess hole has to remain localized around the spin-flipped site, consistent with the numerical results. If these defects can be properly connected along the diagonal line with minimal frustration, the gain in exchange energy is maximized.

When the system is doped with two holes, the ground state under PBC shows three

spin flip defects that bind into a diagonal line as can be seen from the local ferromagnetic behavior superimposed on the AFM background. This diagonal line of three spin flips contains all of the extra hole density. We will refer to this as a magnetic line defect from the AFM order. In less energetically favorable systems, two spin flips similar to the ones in the one hole systems were seen. Our calculations on these systems suggested that the single spin flip defects repel each other, and the lowest energy state is reached when they bind into a magnetic line defect occuring over three diagonal Cu sites.

The last system in Fig. 2.6 has the same doping, $h = 1/36$, as the two-hole doped system just discussed; however, it has a supercell twice the size, thus giving a doping of four holes. The calculations show the magnetic line defects growing longer (5 Cu sites vs. 3) with similar spin and charge order on the O p-sites as the two-hole doped system. Along with the magnetic line defect is an isolated spin flip defect. The calculations suggest that the system slowly builds 1-D magnetic line defects as doping is increased. At first the excess holes repel until a sufficient number of defects are present and it becomes beneficial to combine them. (Pan and Gong[53] had performed mean-field studies of a few-hole doped systems, though they did not explore a similar parameter space.)

These calculation suggest the following physical picture from GHF. At very low doping there are isolated holes and short magnetic defect lines. As doping increases, the lines start to create one-dimensional MDWs which are spaced away from each other. Around $h = 1/8$ doping (roughly corresponding to maximum transition temperature in cuprates), closely spaced, mostly one-dimensional, domain walls dominate the system. As doping is further increased, the system starts to create orthogonal domain walls, eventually creating checkerboard patterns. Some of these features are likely related to the situation in the intermediate Δ regime, which is discussed below in Sec. 2.3.3.

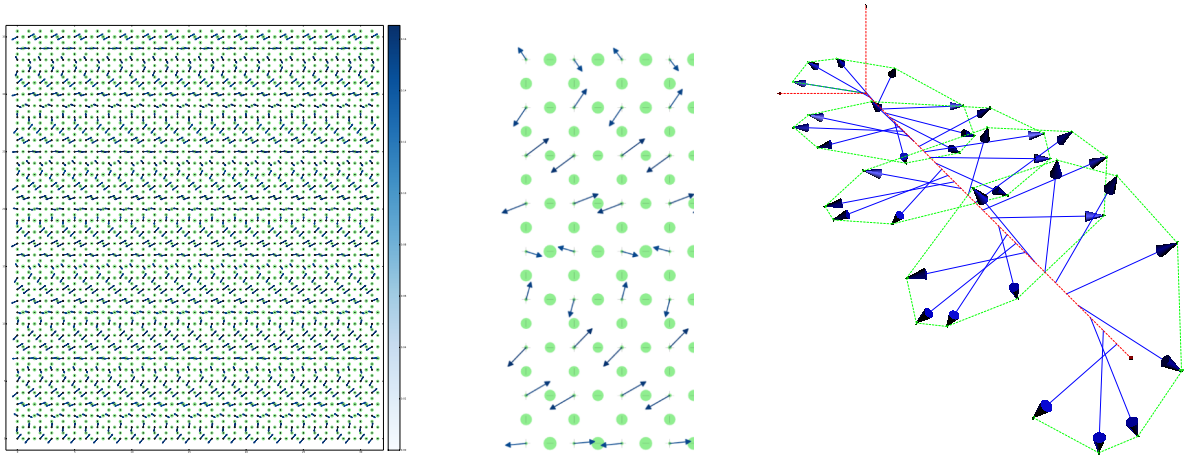

(a) (b) (c)

FIG. 2.7: (Color online) Charge and magnetic order for a periodic 32×36 supercell, with $\Delta = 1.5$ eV and $h = 1/8$. In (a), the spins (arrows) are plotted as a projection in the x-y plane. The total spin, $S_{tot}(\vec{r})$, on each site is given by the color gradient on the right. The spin on the O sites is negligible. The size of the green circles are proportional to the excess hole density from half-filling, $\delta n_{\text{excess}}(\vec{r})$. A small section of the lattice can be seen in (b), better highlighting the order. In (c) a 3-D plot of the staggered spin is shown along a line cut at $x = 0$, viewed along the y-axis. Blue arrows are the real 3D staggered spin and green dashed lines connect near neighbor spins to highlight spiral structure.

2.3.2 Spin Spirals

Magnetic and Charge Order

We now turn to the lowest considered charge-transfer energy, $\Delta = 1.5\ eV$. In this regime, we find an AFM state at half-filling with $n_d \approx 0.4657$ and $n_p \approx 0.2672$. At doping of $h = 1/8$, we find a new spin order, characterized by a uniform charge distribution with a long wavelength planar spin spiral. In the GHF ground state, most of the extra charge (holes) are localized on the oxygen p-orbitals, as opposed to the d-orbitals on the Cu sites.

In Fig. 2.7, we show the spin density $(S_x(\vec{r}), S_y(\vec{r}), S_z(\vec{r}))$ and the excess hole density, $\delta n_{\text{excess}}(\vec{r})$ on a lattice containing 32×36 unit cells with periodic boundary conditions, that is, from a $Cu_{1152}O_{2304}$ supercell. The spin on the p-orbitals is negligible and is omitted in the plot. The charge order is uniform across the lattice. The leading spin order is anti-

ferromagnetic on the Cu sites; however, the spin is slowly turning in a randomly chosen plane. Unlike in a linear spin-density wave, the spiral has a near constant total spin, S_{tot}.

In the right panel of Fig. 2.7, an image of the 3–D *staggered* spin density, $(-1)^{x_i+y_i}\,\vec{S}_i$ is shown along a line cut. The spin rotation is almost perfectly constrained to a plane (i.e., if all spins are translated to a single point, the spin vectors lie in a plane), with the orientation of the plane seemingly random. The projection of a spin spiral onto a single spin orientation, which would be typically how the spins are resolved experimentally, would appear as a linear spin wave or AFM domains. Our results suggest that such structures could be an indication of a more complex three-dimensional spiral behavior.

To estimate the wavelength of the spiral, we investigated the dependence of the energy per site, E/L, on L_y in $4 \times L_y$ supercells. As we show in Fig. 2.8, there are comparable energy solutions with spiral wavelengths of 7, 8, 9, and 10 Cu sites. The best solutions, as indicated by E/L, occur at $L_y = 36, 72$, which would suggest a spiral wavelength of 9 Cu sites. On the other hand, perfect spiral order with constant charge order were also observed in an 8×8 supercell . Further, for wider $8 \times L_y$ supercells, the spiral tends to align along the (short) x-direction. We then performed a comprehensive study of 16×18 systems, which shows a variational energy preference to align the spiral in the y-direction ($L_y = 18$) rather than x. This leads us to believe the spiral wavelength is closer to 9 Cu sites, with uniform charge density. The order is very robust against changes in geometries and sizes. The spiral s always oriented along x- or y-direction, propagating along the Cu-O bonds.

Momentum Distributions and Nesting

In this section, we examine the properties of the GHF ground state in momentum space. In particular, we are interested in detecting and understanding nesting properties of these systems. As in Sec. 2.3.1, we consider spin-resolved momentum distributions $n_\uparrow(\mathbf{k})$

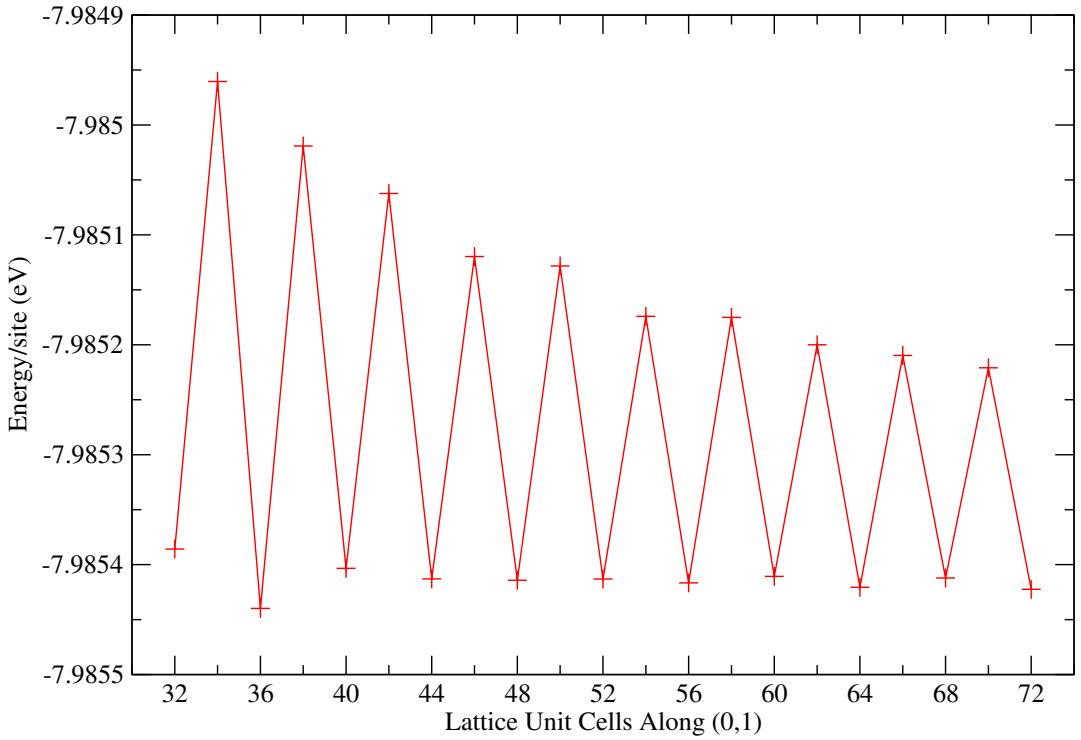

FIG. 2.8: (Color online) Energy per site vs. lattice length along y for $4 \times L_y$ systems at $\Delta = 1.5$ eV, $h = 1/8$, PBC.

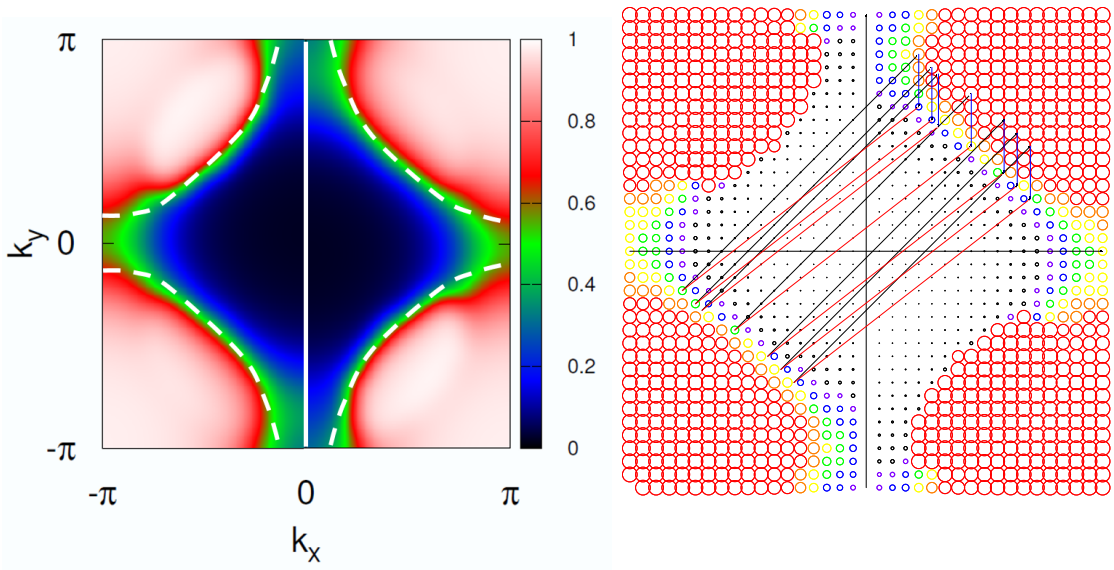

(a) (b)

FIG. 2.9: (Color online) Momentum distribution and nesting structure for spin spiral states. The left panel shows $n_\sigma(\mathbf{k})$ for $\sigma =\uparrow$ (left half) and $\downarrow$ (right half) in the 32×36 supercell in Fig. 2.7. The color scale is set to show nearly fully occupied momenta in white/red, nearly empty momenta in blue/black, and half occupied momenta around the Fermi surface in green. The white dotted lines outline the Fermi surface of the non-interacting solution for the same system. The right panel illustrates the nesting structure. Similar to the left panel, $n_\uparrow$ is on the left half and $n_\downarrow$ is on the right. The size of the circles is proportional to the occupation (magnitude of n_σ). The colors are to guide the eye around the Fermi surface. The black lines represent a (π, π) vector. The red lines connect complementary points $\mathbf{k}$ and $\mathbf{k}'$ between $n_\uparrow(\mathbf{k})$ and $n_\downarrow(\mathbf{k}')$ near the Fermi surfaces (see text). The blue lines show the shift $(\mathbf{k}' - \mathbf{k})$ [with respect to (π, π)], which defines the spiral wave vector.

and $n_\downarrow(\mathbf{k})$. Fig. 2.9 shows the momentum distributions for a large, 32×36 supercell. Only half of $n_\sigma(\mathbf{k})$ is displayed for each σ. In the GHF solution, symmetry is broken along y but preserved in the x direction, so that the full momentum distribution can be recovered by reflection with respect to the k_y axis, $n_\sigma(-k_x, k_y) = n_\sigma(k_x, k_y)$. The re-construction at the Fermi surface is evident relative to the non-interacting momentum distribution. (It should be stressed that all the formulation is in terms of holes; the momentum distributions for electrons can of course be mapped straightforwardly from these results.)

We observe a spectacular interplay between $SU(2)$ symmetry breaking and translational symmetry breaking, resulting in a nesting property that stabilizes a spin spiral. For perfect AFM order, the nesting vector, $\vec{Q}$, should coincide with (π, π). A shift in this nesting vector corresponds to an instability towards a modulated phase. In the one-band Hubbard model, for example, the HF solution is found [51] to produce linear spin density waves in large portions of the parameter space, the symmetry $n_\uparrow(\mathbf{k}) = n_\downarrow(\mathbf{k})$ is preserved, and the spin density waves can be thought of as a linear combination of two counter-propagating spirals. Here we have a broken symmetry in the momentum distribution between $\uparrow$- and $\downarrow$-spins, resulting in a non-colinear spin wave. The right panel of Fig. 2.9 illustrates the nesting more quantitatively. We identify complementary points $\mathbf{k}$ and $\mathbf{k}'$ near the two Fermi surfaces for which $n_\uparrow(\mathbf{k}) + n_\downarrow(\mathbf{k}') \doteq 1$ within a few percent. The large number of pairs found indicate that the spiral is created predominantly by a simple pairing mechanism [58, 51] involving two primary planewaves. [The simplest model [59] to help visualize the spiral state is spin orbitals of the form $u \exp(i\,\mathbf{k}\cdot\mathbf{r})|\uparrow\rangle + v \exp(i\,\mathbf{k}'\cdot\mathbf{r})|\downarrow\rangle$, where $|u|^2 + |v|^2 = 1$ and the nesting vector is $\mathbf{Q} \equiv \mathbf{k}' - \mathbf{k}$.] From the figure we see that the nesting vector is consistently shifted along the y-direction by $4 \times (2\pi)/36$, which corresponds to 9 Cu sites in real space. This is consistent with the numerical estimation above.

Behavior at Low Doping

We also explored the cases with very low doping (one and two doped holes) in a periodic lattice, as we have done for the magnetic domain wall phase in Sec. 2.3.1. For an 8×8 supercell, $Cu_{64}O_{128}$, at $h = 1/64$ and $1/32$ doping, the order of the systems showed very little deviation from half-filling. For a single hole ($h = 1/64$), the calculations show that the order is nearly a perfect anti-ferromagnet. There are some minor periodic modulations of the total spin in the Cu d-orbitals from an AFM background. The density is also very close to uniform, with minor modulations coinciding with the Cu spin deviation. As in the case of $h = 1/8$, most of the extra density lies on the O p-orbitals. For two holes ($h = 1/32$), the calculations show similar order as the single hole case. The spin shows near perfect AFM order with periodic deviations in the total spin. Compared to the single hole system, the periodic deviation occurs twice as often. The charge order is nearly uniform with most of the extra hole density on the O p-orbitals, again with minor modulation coinciding with that of the total spin.

The low doped regimes for the large ($\Delta = 4.4$) and small charge transfer ($\Delta = 1.5$) systems highlight their differences. In the large charge transfer regime, as discussed in Sec. 2.3.1, occupation of the O p-orbital is highly unfavorable compared to occupation of the Cu d-orbital, even at very low doping. This causes the system to find charge configurations in which the extra hole density is concentrated and localized around some Cu sites, where a spin-flip occurs to exploit exchange energy. In contrast, in the lower charge transfer regime, extra holes occupying an O p-site is less unfavorable. This allows more uniform charge configurations in which the O sites carry most of the excess charge. From the uniformity, the spin order on the Cu sites is able to largely retain AFM order, with smooth modulations leading to wave behavior (i.e. spin waves and spirals).

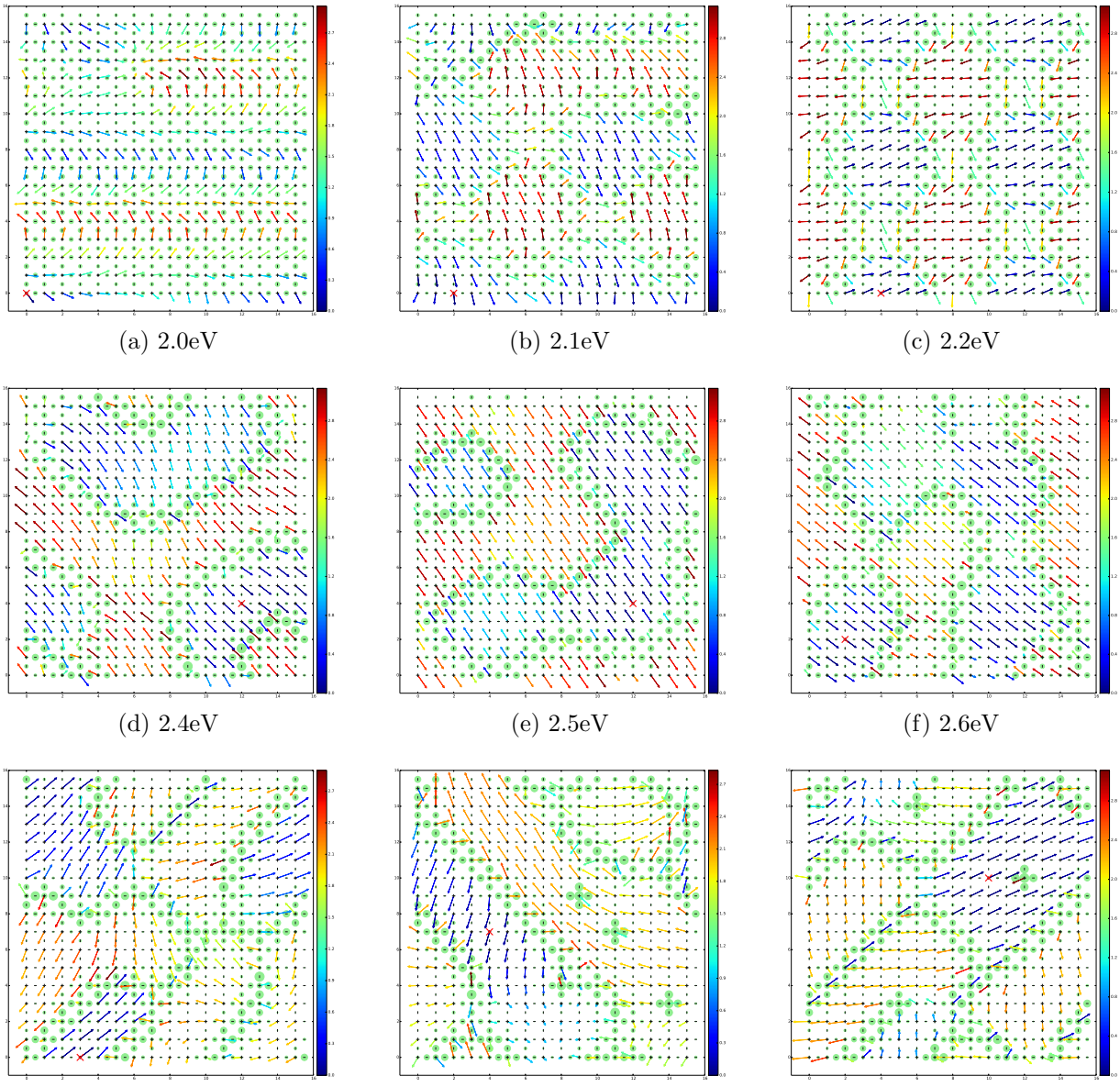

(a) 2.0eV (b) 2.1eV (c) 2.2eV

(d) 2.4eV (e) 2.5eV (f) 2.6eV

(g) 2.8eV (h) 2.9eV (i) 3.0eV

FIG. 2.10: (Color online) Evolution of the magnetic and charge order from an AFM spiral to ferromagnetic domain walls. A 16×16 supercell is studied for varying values of the charge transfer energy, Δ, in the intermediate regime, at $h = 1/8$. The total staggered spins (arrows) are plotted as a projection in the x-y plane. The color of the arrow represents the angle between the spin on that site and a reference spin marked by the red "x". It can be thought of as a spin correlation and it runs from $(0, \pi)$. The spin on the O sites is negligible and omitted from the plot. The size of the green circles are proportional to the excess hole density from half-filling, $\delta n_{\text{excess}}(\vec{r})$.

2.3.3 Intermediate Nematic Order

Within GHF, the MDW phase discussed in Sec. 2.3.1 is sustained at high Δ down to $\Delta \sim 4.2$, while the spin spiral phase discussed in Sec. 2.3.2 exists up to $\Delta \sim 2$. This is for hole doping of $h = 1/8$ and the parameter values given in Table 2.1. Clearly the phase boundaries in Δ as well as the nature of the phases can vary with the other parameters. We next investigate charge transfer values between the two regimes, scanning Δ = 2-3. Our goal was to determine what happens in the intermediate region between the MDW and the spiral states, whether additional phase(s) exists, and how the transition occurs.

Fig. 2.10 shows order plots for an $L_x \times L_y = 16 \times 16$ supercell, i.e. $Cu_{256}O_{512}$, at $h = 1/8$ for varying values of the charge transfer energy. Systems with $\Delta \leq 2.0$ lie in the spiral phase, while systems with $\Delta \geq 4.3$ lie in the MDW phase. Between the two, there appears to be a crossover regime. Though the charge and spin order are unique at each Δ value as we scan through the transition region, there are common features. At lower values of the charge transfer energy Δ, the excess charge is distributed more uniformly across the O p-orbitals in the lattice. When Δ is raised, the excess charge accumulates into predominantly diagonal lines on the lattice. Up until a sufficient value of $\Delta \sim 2.8$, these lines are mostly centered on the O p-sites. As the charge transfer energy is increased, the lines of excess charge become more rigidly locked at 45° (135°) angles.

Inspecting the spin order in conjunction with the charge order, we also see clearly the effect of doping on the system. Uniform excess holes that lie on the O p-orbitals allow for a smooth spiral modulation of the spin. The system is able to retain anti-ferromagnetism to leading order with an overall modulation to accommodate the excess holes. As the charge starts to accumulate from a uniform distribution to localized diagonal lines, it creates a need for more dramatic changes in the spin order from that at half-filling to accommodate highly localized excess holes. Away from these diagonal lines, the charge order is close to

that of half-filling at the same Δ and therefore recovers anti-ferromagnetic order. Close to these lines of excess charge, the spin turns sharply, creating ferromagnetic domain walls that separate spin-isolated anti-ferromagnetic domains.

The excess charge on the Cu atoms leads to a staggered spin correlation between the spin in the neighboring domain and the spin on the domain wall. The value of this staggered spin angle correlation between the two spins seems to be related to the excess hole occupation on the Cu atom. The greater the excess hole occupation, the greater the staggered spin angle correlation is between the domain wall and the neighboring AFM domains. At first, the d-sites develop frustration, i.e., ferromagnetic links, from the AFM background, creating a phase slip similar to the spin-density wave or stripe phase in the one-band Hubbard model [48, 51, 47]. As Δ further increases, the Cu sites near the excess charge line start to develop spin-isolating ferromagnetic domain wall order as a precursor to the MDW phase. Separated by the walls of localized charge density, the AFM order in each isolated domain can be in a completely different direction (third row), creating nematic orders. The spin correlation hits a critical point at a certain excess hole occupation on the Cu atom at which the correlation is at a maximum value of π. For example, when at $\Delta = 3.0$ some of isolated spin flip defects which correspond to this maximum value can be seen. Once the charge transfer energy is high enough ($\Delta \sim 4.3$) to consistently allow greater excess hole occupation on the Cu d-orbitals than the O p-orbitals, we enter the MDW phase, in which the different domains become phase coherent.

Our results in this regime, particularly those regarding the interface between two domains, seems consistent with the spin canting phases found by Seibold et. al, who use an unrestricted Gutzwiller approximation on the three-band Hubbard model [57, 60]. They argue that the spin canting phase is a result of the competition between a classical diagonal stripe phase, characterized by the localized domain walls, and linear spin spirals, characterized by the canting of the spin order near these lines. Though their study finds

this order at very low doping of $h = 0.03$, our results are consistent with this interplay between the localized diagonal domain walls and the spin spirals. Unlike this spin canting phase, our nematic phase does not exhibit coherent AFM order in the domains throughout the supercell. Rather, the spiral behavior across different domain walls occurs in different random planes, causing the direction of the AFM order within the domains to isolate from each other, creating the incoherent AFM domains.

2.4 Summary and Discussion

We have presented our study of the hole-doped CuO plane applying the generalized Hartree-Fock approach to the three-band Hubbard model. We scanned values of the charge transfer energy and different doping parameters, using "physical" values for the other parameters as derived for lanthanum-based cuprates. We find that, compared to the simplest picture of the one-band Hubbard model, the inclusion of the Oxygen p-orbitals within the three-band (Emery) model leads to new phases with fascinating characteristics potentially of direct relevance to experimental observations in high-T_c materials.

The charge transfer energy directly affects the hole occupation on the Cu d-orbitals versus the O p-orbitals. Our study showed that, even for high values of the charge transfer energy ($\Delta = 4.4$), where occupation of the O p-orbitals is highly unfavorable, there is still non-trivial hole occupation on the p-sites, highlighting the importance of the three-band model. Though a majority of the doped holes lie on the Cu d-orbitals, there is significant ordering on near neighbor O p-obitals. As the charge transfer energy is lowered, more holes occupy the p-orbitals as expected. At $\Delta = 1.5$ the charge ordering is uniform with a vast majority of the doped holes occupying the O p-orbitals.

While varying the charge transfer energy at optimal doping, $h = 1/8$, we find three distinct phases: Magnetic Domain Walls, Spin Spirals, and an intermediate crossover with

nematic order. In the MDW phase, which occurs at large Δ, the doped holes localize on diagonal lines centered on the Cu sites. An overall spin flip ($\vec{S} \rightarrow -\vec{S}$) occurs in the middle along the diagonal line, embedded in an anti-ferromagnetic background. This forms diagonal domain walls with a thickness of three Cu sites along the x (or y) direction, with the middle one bearing the spin flip and most of the excess charge. There is no phase flip between adjacent AFM domains separated by the MDW. Though our lowest energy solutions with finite (but large) supercells tend to show some two-dimensional features, it seems likely that the GHF ground state in the thermodynamic limit is one-dimensional, with parallel diagonal MDWs, with a lateral spacing of 6 Copper sites.

In the spiral phase, which occurs at low $\Delta < 2.0$, the charge order is uniform with most of the doped holes in the O p-orbitals. The spins on the Cu sites have a modulated anti-ferromagnetic order. The anti-ferromagnetic order slowly turns in a randomly chosen plane (depending on the initial variational state) as it propagates along x or y-direction. The wavelength of the spiral, for $h = 1/8$ and with the *ab initio* parameters, appears to be around 8 or 9 Cu sites.

In the intermediate Δ region, there is competition between the uniform charge order of the spiral phase and the localized charge order of the MDW phase. A majority of the doped holes occupy the O p-orbitals. Starting from an antiferromagnetic spiral state propagating along the y-direction (x-direction), the different spiral lines at different y (x) positions gradually develop phase differences beyond the perfect staggered order $(-1)^y$. As the charge transfer energy is increased, holes start to localize on diagonal lines centered on the O p-sites. The spins in the Cu d-orbitals near such O sites make more drastic deviations from the AFM order. As the diagonal lines of excess charge form, the Cu spin order near it most resembles the linear spin-density wave or stripe order seen in the one-band Hubbard model. The diagonal lines of charge separate anti-phase, anti-ferromagnetic domains.

It is important to keep in mind that these are results from a mean-field GHF approach. More accurate treatment of correlation effects can move the phase boundaries with respect to parameter values (or even invalidate some of the phases). However, experience from the one-band Hubbard model indicates that HF tends to capture most of the magnetic and charge orders qualitatively [48, 51]. In fact in the one-band Hubbard model, UHF with a renormalized effective U/t parameter seems to give quantitatively quite accurate results on the magnetic and charge orders [22]. Our study serves as a starting point for future studies, and reveals several important candidate phases. For certain advanced methods such as auxiliary-field quantum Monte Carlo (AFQMC) [61, 62], our results also provide the necessary trial wave functions. Furthermore, a self-consistency procedure coupling our GHF calculation to AFQMC will allow an even more accurate determination of the many-body ground state.

It will be very interesting, in future studies, to investigate possible connections of the characteristics of magnetic and nematic orders to superconducting order. This will require more advanced methods, since no superconducting order can arise within the GHF approach adopted here. An approach that generalizes it would be to introduce a term with paring order in the mean-field Hamiltonian, and couple the calculation self-consistently to a many-body calculation (e.g., AFQMC) to match spin densities and anomalous density matrix (pairing order parameters), which will allow an effective pairing interaction strength to be determined.

CHAPTER 3

An auxiliary-field quantum Monte Carlo study of the magnetic and charge orders in the ground state of the Emery model in the underdoped regime

Motivated by the considerations laid out in the previous chapters and to understand how similar or different the three-band model is from the one-band Hubbard model, we investigate in this chapter the three-band model at zero-temperature in the underdoped regime, using a state-of-the-art auxiliary-field quantum Monte Carlo (AFQMC) algorithm. We focus on the nature of the spin and charge orders, and seek to quantify the competition between stripes, spin spirals, and other nematic orders in the thermodynamic limit. Our method employs a self-consistent constraint [22] on paths sampled in auxiliary-field space,

which has been referred to as the constrained path (CP) approximation [62] in computations of model systems. The CP approach relies on a trial wave function or density matrix for a sign or gauge condition on the sign or gauge of the Slater determinants sampled in the AFQMC, thereby controlling the sign problem. This approach has consistently demonstrated a high level of accuracy and allowed robust predictions in the one-band Hubbard model [63, 47, 48].

The rest of the chapter is organized as follows. In Sec. 3.1, we introduce the three-band Hubbard model. In Sec 3.2, we briefly describe the CP AFQMC method as well as the self–consistent scheme used. In Sec. 3.3, we present our findings for the (3.3.1) spin and charge order, (3.3.2) momentum distributions, (3.3.3) several other ground-state properties, and (3.3.4) the hole-electron asymmetry. We further discuss results and make conclusions in Sec. 3.4.

3.1 Model

The Emery model, also called three-band Hubbard model, includes the Cu $3d_{x^2-y^2}$ orbital and the O $2p_x$ and $2p_y$ orbitals explicitly in the description of the copper-oxide planes in the cuprates. In Fig. 3.1, a schematic representation of one CuO_2 plane is shown to help visualize the model. We will consider simulation supercells made of $M = L_x \times L_y$ unit cells of CuO_2, with a given number of particles (or more precisely of holes), N , which then defines the density or doping. The Hamiltonian is

$$\begin{aligned}\hat{H} = &\varepsilon_d \sum_{i,\sigma} \hat{d}^\dagger_{i,\sigma}\hat{d}_{i,\sigma} + \varepsilon_p \sum_{j,\sigma} \hat{p}^\dagger_{j,\sigma}\hat{p}_{j,\sigma} + \\ &\sum_{<i,j>,\sigma} t^{ij}_{pd}\left(\hat{d}^\dagger_{i,\sigma}\hat{p}_{j,\sigma} + h.c\right) + \sum_{<j,k>,\sigma} t^{jk}_{pp}\left(\hat{p}^\dagger_{j,\sigma}\hat{p}_{k,\sigma} + h.c\right) \\ &+ U_d \sum_i \hat{d}^\dagger_{i,\uparrow}\hat{d}_{i,\uparrow}\hat{d}^\dagger_{i,\downarrow}\hat{d}_{i,\downarrow} + U_p \sum_j \hat{p}^\dagger_{j,\uparrow}\hat{p}_{j,\uparrow}\hat{p}^\dagger_{j,\downarrow}\hat{p}_{j,\downarrow}\,.\end{aligned} \tag{3.1}$$

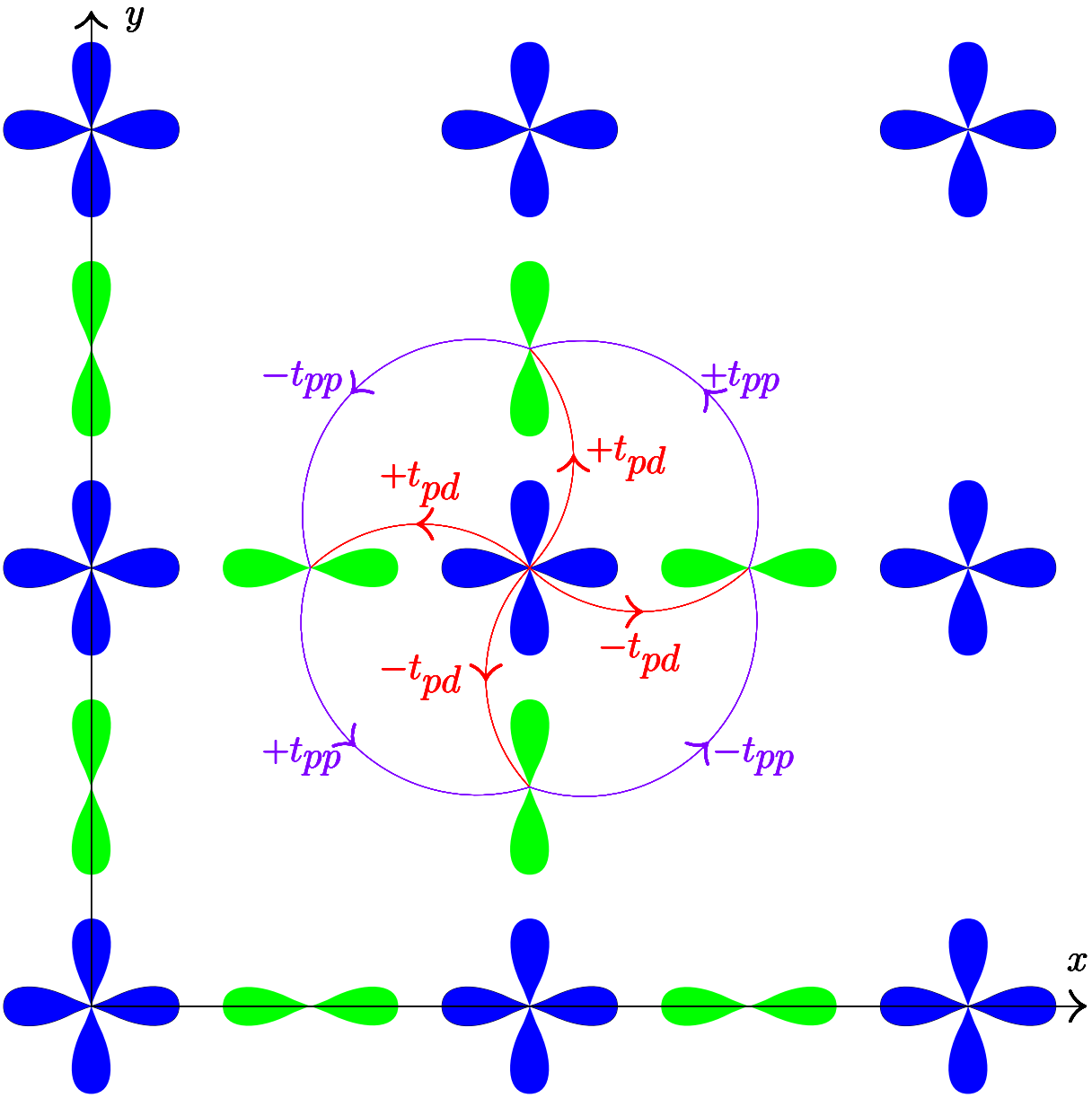

FIG. 3.1: (Color online) Schematic view of the CuO_2 planes in cuprates and illustration of the 3-band model. Cu $3d_{x^2-y^2}$ orbitals are represented in blue, and O $2p_x$ and $2p_y$ orbitals in green. We use the reference frame defined by the two axes in the figure. The curve connectors represent the hopping, and the labels define the sign rule.

TABLE 3.1: Parameter values adopted in the present study. The parameters are obtained from La_2CuO_4 [1]. We study the value of $\Delta = \varepsilon_p - \varepsilon_d$ at 4.4 and 2.5.

Parameter	U_d	U_p	ε_d	ε_p	t_{pd}	t_{pp}
Value (eV)	8.4	2.0	-8.0	-3.6	1.2	0.7

In Eq. (3.1), i runs over the sites $\vec{r} = (x, y)$ of a square lattice $\mathbb{Z}^2$ defined by the positions of the Cu atoms, $\vec{r}_{\mathrm{Cu}}$. The labels j and k run over the positions of the O atoms, shifted with respect to the Cu sites, $\vec{r}_{\mathrm{O}_x} = \vec{r}_{\mathrm{Cu}} + 0.5\,\hat{x}$ for the $2p_x$ orbitals, and $\vec{r}_{\mathrm{O}_y} = \vec{r}_{\mathrm{Cu}} + 0.5\,\hat{y}$ for the $2p_y$ orbitals. The model is formulated in terms of holes rather than electrons: for example, the operator $\hat{d}^{\dagger}_{i,\sigma}$ creates a hole on the $3d_{x^2-y^2}$ orbital at site i with spin $\sigma = \uparrow, \downarrow$. The first two terms in the Hamiltonian contain the orbital energies, which define the charge-transfer energy parameter $\Delta \equiv \varepsilon_p - \varepsilon_d$, which can be thought of as the energy needed for a hole to move from a Cu $3d_{x^2-y^2}$ orbital to an O p orbital. The next two terms describe hopping between orbitals; the hopping amplitudes t_{pd}^{ij} and t_{pp}^{jk} are expressed in terms of two parameters, t_{pd} and t_{pp}, and the dependence on the sites is simply a sign factor, as depicted in Fig. 3.1. Finally, the last two terms represent the on-site repulsion energies, or double-occupancy penalties, similar to those in the one–band Hubbard model. We neglect Coulomb interactions beyond the on-site terms.

We study the properties of the model as a function of the charge transfer energy Δ. Our starting point is an *ab intio* set [1] of parameters obtained for La_2CuO_4, the parent compound of the lanthanum based family of cuprates. The parameter values are listed in Table 3.1. This set corresponds to a charge transfer energy $\Delta = 4.4$ eV. To correct for possible double counting issues [31] would imply a considerable reduction of this value to $\Delta \sim 1.5$ eV, which as pointed out above, can greatly change the physics of a system.

Most of our calculations are performed at hole-doping, $h = 1/8$. The hopping and on-site interaction parameters are kept at the values given in Table 3.1, and the charge–

transfer energy, Δ, is varied. Building on our half-filling study [34], we focus on two particular values, $\Delta = 4.4$ and 2.5, which are representative of the insulating and conducting states at half–filling, respectively.

3.2 Methods

To compute the ground state properties of the model in Eq. (3.1) for a given system, i.e., a given set of parameters $(\varepsilon_d, \varepsilon_p, \{t^{ij}_{\alpha\beta}\}, U_d, U_p)$ and supercell, we use the Constrained Path Auxiliary Field Quantum Monte Carlo (CP-AFQMC) method [61, 62]. In addition to tests in lattice models [63], this method has been shown in a variety of other correlated systems to be among the most accurate, low-polynomial scaling many-body methods [64, 65].

In order to sample the ground state $|\Psi_0\rangle$ of the Hamiltonian in Eq. (3.1) for a given supercell, the technique relies on the imaginary-time evolution of an approximate initial wave function, say $|\psi\rangle$:

$$|\Psi_0\rangle \propto \lim_{\beta\to+\infty} \exp(-\beta(\hat{H} - E_0))|\psi\rangle \tag{3.2}$$

where E_0 is the ground state energy which is estimated adaptively in the process. The projection formula in Eq. (3.2) is valid for any $\langle\psi \,|\, \Psi_0\rangle \neq 0$. In the CP–AFQMC algorithm, the imaginary-time evolution is mapped on to open-ended branching random walks in the manifold of Slater determinants, known as the "walkers." The sign problem is controlled through the introduction of a trial wave function, $|\psi_T\rangle$, which guides the random walks and imposes a sign constraint by eliminating random walk paths when the overlap of a walker with $|\psi_T\rangle$ first turns negative. (A gauge constraint is applied on the overall phase of the Slater determinant in the case of walkers described by Slater determinants with complex orbitals [66].)

In this study, we are concerned with the cooperating or competing magnetic and charge orders that may arise in the three–band model as a function of the charge transfer energy. We define the spin on the Cu sites for the d-bands as

$$\hat{\mathbf{S}}(\mathbf{r}) = \frac{1}{2} \sum_{\sigma,\sigma'} \boldsymbol{\sigma}_{\sigma,\sigma'} \, \hat{d}^{\dagger}_{i,\sigma} \hat{d}_{i,\sigma'} \, , \tag{3.3}$$

where $\boldsymbol{\sigma}_{\sigma,\sigma'}$ denotes the elements of the Pauli spin matrices. As in (3.1), the label i is in one-to-one correspondence with the position $\mathbf{r} = (x, y)$. The spins on the O p-bands can be similarly written down, but they turn out to be negligible as we discuss below. The charge densities are defined as

$$\hat{n}_{\alpha}(\mathbf{r}) = \sum_{\sigma} \hat{\alpha}^{\dagger}_{i,\sigma} \hat{\alpha}_{i,\sigma} \, , \tag{3.4}$$

where α is either d or p_x or p_y, and the operator $\hat{\alpha}^{\dagger}_{i,\sigma}$ is the corresponding creation operator for a hole of spin σ in the unit cell i.

In order to optimize the numerical detection of complex spin and charge orders, we explicitly break translational and $SU(2)$ symmetry through the application of a weak pinning field coupled to the local spin density on one side of the system:

$$\hat{V}_{\text{ext}} = \sum_{\mathbf{r}=(x,y)} \delta_{y,0} (-1)^{x+y} \, \mathbf{h}_{\text{pinn}} \cdot \hat{\mathbf{S}}(\mathbf{r}) \tag{3.5}$$

where $\mathbf{h}_{\text{pinn}} = (h_x, h_y, h_z)$ can be tuned to obtain the desired external field. Throughout this paper, we choose the pinning field to be coupled to the in-plane x-component of the spin density, unless stated otherwise. This field induces a local antiferromagnetic (AFM) order on the $d_{x^2-y^2}$ orbitals on one side of the system. The presence of the long-range order is determined by measuring the behaviors of the spin and charge density, after

extrapolation of the results to the thermodynamic limit and to the $h_{\text{pinn}} \to 0$ limit. The symmetry-breaking pinning field allows us to measure densities as opposed to correlation functions which would be needed in fully periodic calculations. This dramatically improves our resolution, since at large distance (from the location of the pinning field) the order being numerically measured becomes $\mathcal{O}(S)$ rather than $\mathcal{O}(S^2)$, where S is the "order parameter", for example, the magnitude of the spin.

3.2.1 Self-Consistent Constraint

The CP constraint is an approximation which results in a systematic bias. The magnitude of the bias has been shown to be usually very small, even with simple mean-field $|\psi_T\rangle$. (For example, in the one-band Hubbard model with $U/t = 8$ and near 1/8 doping, the CP error in the energy [67, 63] using a $|\psi_T\rangle$ from unrestricted Hartree-Fock is less than the Trotter error from a time-step choice of $\tau = 0.05\, t^{-1}$, which is typically considered a very conservative choice in standard calculations.) Better choices of $|\psi_T\rangle$ can reduce the systematic bias. In our implementation, the trial wave function $|\psi_T\rangle$ is of the form of general Slater determinant:

$$\begin{aligned} |\psi_T\rangle &= \prod_{n=1}^{N} \hat{\phi}_n^\dagger \, |0\rangle \\ \hat{\phi}_n^\dagger &= \sum_{i=1}^{M} \sum_{\sigma=\uparrow,\downarrow} \sum_{\alpha=d,p_x,p_y} u_n(i,\alpha,\sigma)\, \hat{\alpha}_{i,\sigma}^\dagger \end{aligned} \tag{3.6}$$

where the notations follow Eq. (3.1), with the operator $\hat{\alpha}_{i,\sigma}^\dagger$ creating a hole of spin σ in the α-band in the unit cell i.

The spin-orbitals $u_n(i,\alpha,\sigma)$ in Eq. (3.6) are constructed within a self-consistent scheme which was introduced in [22]. In the first step a GHF calculation is performed where the wave function (3.6) is obtained by minimizing the energy $\langle \Psi \,|\, \hat{H} \,|\, \Psi \rangle$ within the manifold

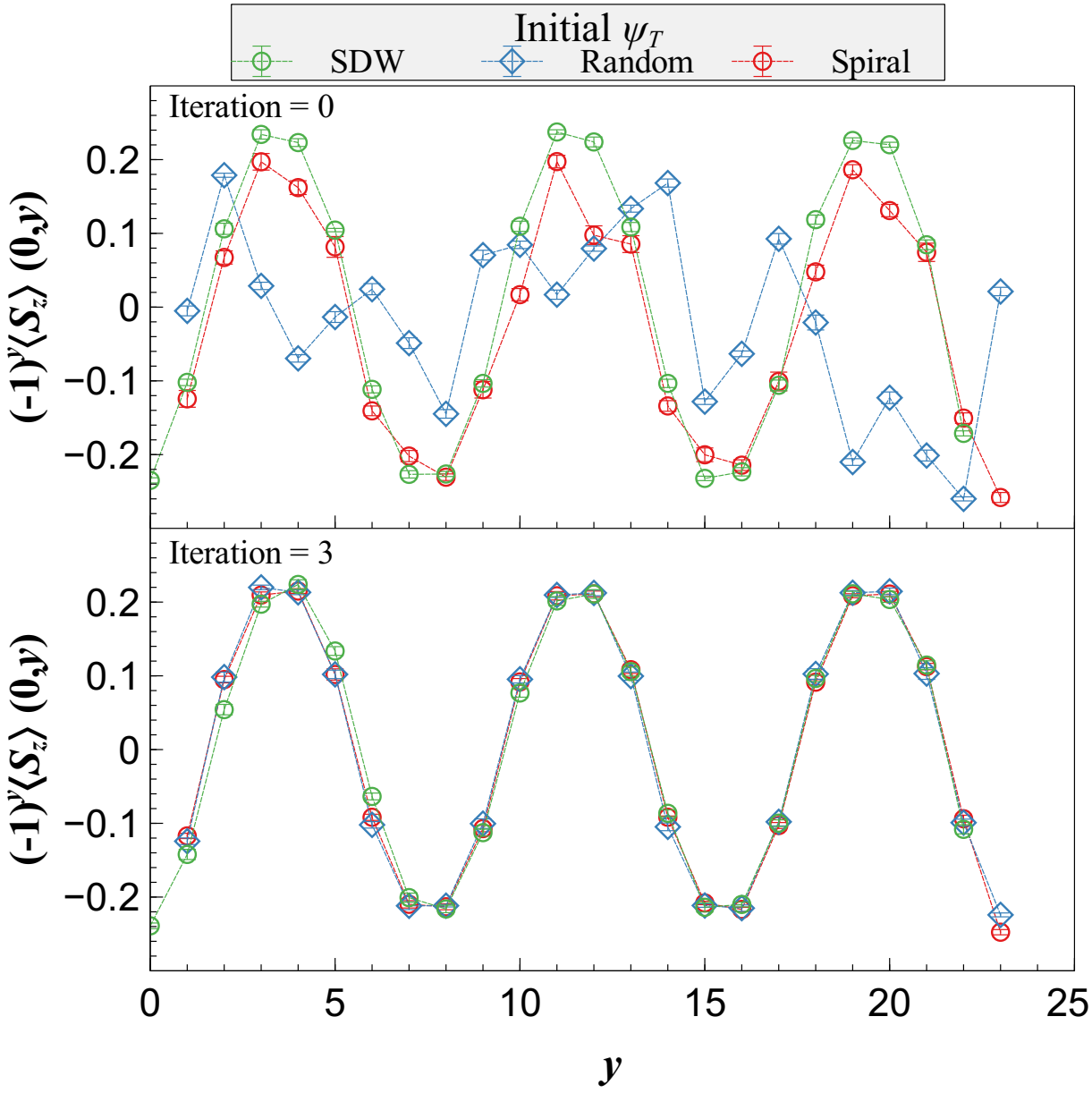

FIG. 3.2: (Color online) Plots of the S_z-component of the staggered spin vector along the line cut at $x = 0$, for three separate self–consistent calculations starting from varied initial states (SDW, Random, and Spiral) for $\Delta = 4.4$. The top panel is the QMC spin order for the 0^{th} iteration. The bottom panel shows the order is converged by the 3^{rd} iteration. The final order is a linear SDW with the majority of the spin vector in the S_z-direction, the same as the pinning field.

of N-particles Slater determinants, using the true Hamiltonian in Eq. (3.1). For the GHF procedure we do not assume any particular form for the order parameter, and we use a combination of randomization and annealing to help find the global minimum [46]. In the following steps, we use the results of CP-AFQMC simulations to correct the trial wave function internally [22] in which the output of a CP-AFQMC calculation relying on a given $|\psi_T\rangle$ is given as feedback in generating a new trial in the GHF framework, but using effective Hamiltonians for $\hat{H}$.

In practice, the new wave function is found by diagonalizing an effective one-body hamiltonian, like in the original GHF procedure, but with effective parameters that are chosen so as to minimize the discrepancy between the variational and the CP-AFQMC estimations of the one-body density matrix. Then, a new CP-AFQMC calculation relying on the updated $|\psi_T\rangle$ is performed and the procedure is continued until convergence is reached. This interface between sophisticated mean-field and correlated CP-AFQMC makes our "adaptive" algorithm able to "learn" the best trial wave function to feed the final CP-AFQMC simulation.

As a further check of the reliability of the approach, we systematically explore the robustness of the self-consistency loops against the choice of the initial condition, that is the wave-function used in the first iteration. Although the GHF solution is a natural starting point, we explored starting from the non-interacting ground-state, as well as from mean-field wave functions displaying other possible orders such as spin density waves, spirals, domain walls. As seen in Fig. 3.2, the self-consistency loops converge to the same spin order, even starting from a random GHF initial state. This is a very strong indicator that our calculations minimize the bias arising from the constraint to control the sign problem. This provides another very powerful check on the robustness and accuracy of the many-body results.

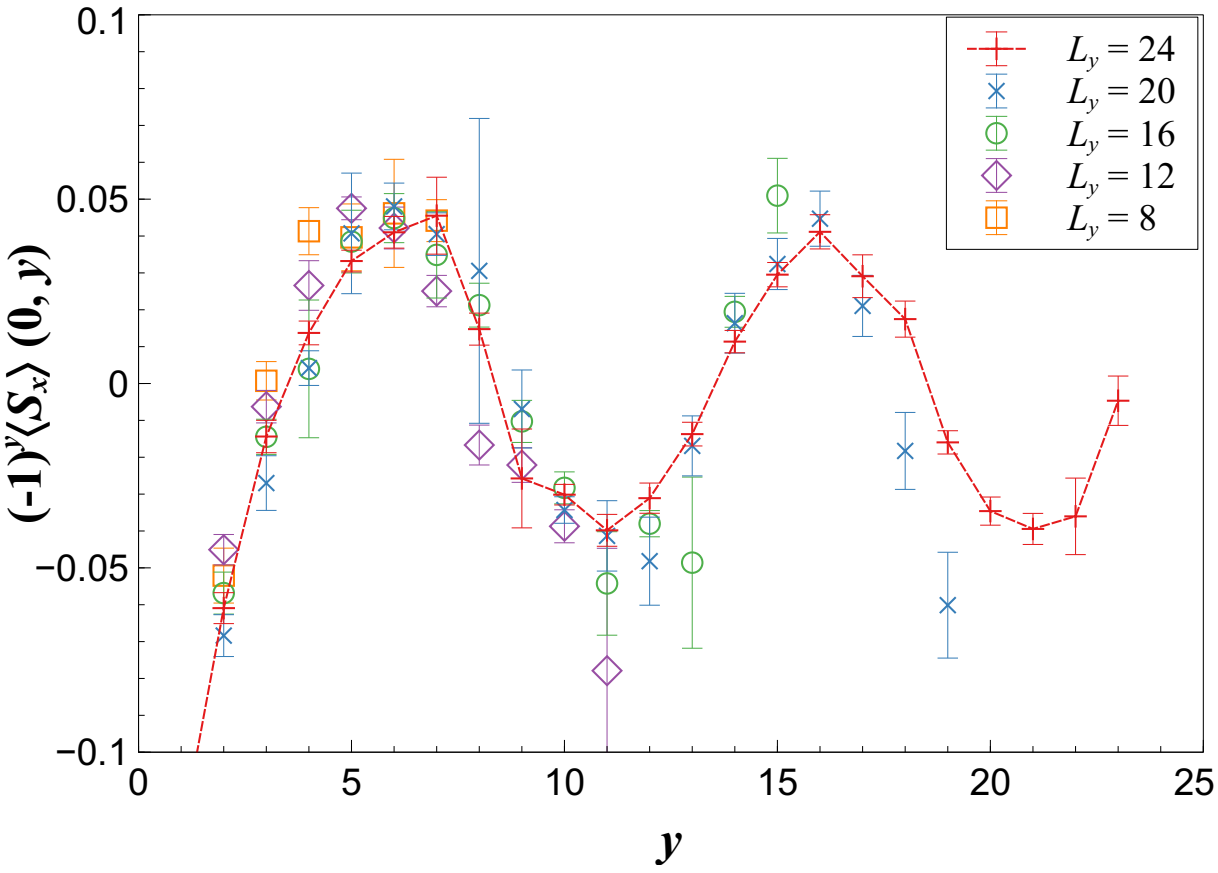

FIG. 3.3: (Color online) Plot of the *staggered* spin vector, $(-1)^y S_x$, for $\Delta = 4.4$ along the line cut at $x = 0$ for a group of $6 \times L_y$ systems. A pinning field is applied at $y = 0$. The spin across the x-direction is antiferromagnetic. The spin order converges as $L_y \to \infty$.

3.2.2 Extrapolation to Thermodynamic Limit

Our AFQMC calculations treat large supercells containing up to ~ 500 atoms, which makes it possible to capture long wavelength collective modes. In addition, we perform various tests to help extrapolate our results to the bulk limit. Our calculations in periodic supercells with $L_x \times L_y$ show that the AFQMC solution favors orders along the x -or y-direction, i.e., along the lines connecting the d orbitals with the nearest neighbor p orbitals. Unlike in the mean-field solutions [46], we find no evidence at the many-body level of a tendency to form long-range orders in the diagonal direction. On the other hand, our results from varying lattice sizes and aspect ratios clearly indicate that large lattices are

needed to accommodate the order while minimizing frustration.

The systematic analysis and experimentation (see for example the results below in Table 3.2) led us to focus on studying rectangular $6 \times L_y$ and $8 \times L_y$ systems. We use periodic boundary condition (PBC) along the x-direction and open boundaries along the y-direction, giving the system the topology of a cylinder, in such a way to accommodate commensurate spin and charge orders along the y direction. We have also carried out calculations with PBCs along both directions (still applying pinning field) to verify the consistency of our results. The cylinder systems and the pinning field break translational symmetry along y and C_4 symmetry, which makes it compatible to use the self-consistent procedure discussed in Sec. 3.2.1. Figure 3.3 shows a validation versus L_y, to establish the spin order as $L_y \to \infty$. We see that, within statistical error, the spin order is already converged at $L_y = 16$. Comparing $6 \times L_y$ calculations with $8 \times L_y$ (and wider systems when there is any indication of numerical difference or as spot checks), we validate that the dependence on L_x, when L_y is large enough, is negligible.

3.3 Results

In Table 3.2 we list the values of several properties of the systems as a function of the size of the system $M = L_x \times L_y$ and of the charge transfer energy, $\Delta = \epsilon_d - \epsilon_p$. The detailed data may prove useful for future analysis. With the high accuracy of these calculations, the results will also help provide benchmark for future studies. In addition, the details help illustrate the convergence with respect to system size.

Results are shown for the total energy per site, the kinetic energies measured by the average nearest neighbor hopping amplitudes, which are the lattice averages of the matrix elements of the one-body density matrix (per site): $T_{dd} = \langle \hat{d}_i^\dagger \hat{d}_{i+\hat{x}(\hat{y})} \rangle$, $T_{pd} = \langle \hat{d}_i^\dagger \hat{p}_{i+\hat{x}(\hat{y})/2} \rangle$, $T_{pp} = \langle \hat{p}_{i+\hat{y}/2}^\dagger \hat{p}_{i+\hat{x}/2} \rangle$, and the interaction energy. Also shown are the average density of

holes on the d and p orbitals respectively (Eq. (3.4)), and the percent of doped holes on the copper d-band, defined as $\delta_{n_d} = ({n_d}^h - {n_d}^0)/h$ where the reference ${n_d}^0$ is the average density of holes on the d orbitals at half filling, while ${n_d}^h$ is the value at the current doping h. The quantity gives an indication of the fraction of the doped holes which go on the d sites.

As mentioned above, all of our calculations include an external pinning field in the hamiltonian acting on the line $x = 0$, playing the role of a surface term, explicitly breaking translational and rotational symmetry. For a fixed value of L_x, both the energies and the densities appear to be consistent with a linear dependence on $1/L_y$, which allows us to compute the bulk values in the limit $L_y \to +\infty$ where all finite-size effects arising from the pinning field and the choice of the boundary conditions vanish. In the table, we report the results of the linear extrapolation as $L_x \times \infty$.

In order to further assess the robustness of our calculations, we also monitored the behavior of the total energy as a function of the width L_x for fixed L_y. The results are presented in Table 3.3 and convincingly show that, thanks to the periodic boundary conditions along x-direction, changing L_x results in variations which are not larger than our estimated statistical error on the $L_x \times \infty$ results, and thus can be neglected.

3.3.1 Spin and Charge Orders

We find that the spin–orders in the Emery model tend to be very subtle, with multiple viable orders competing at tiny energy scales. This results in a high sensitivity of the spin-order with respect to the details of the trial wave function guiding the CP-AFQMC procedure and with respect to the size of the system. It was necessary to perform systematic crosschecks by initializing the self-consistent loop described in Sec. 3.2.1 in several different ways: diagonal magnetic domain walls, spin-density waves (SDW), spiral orders,

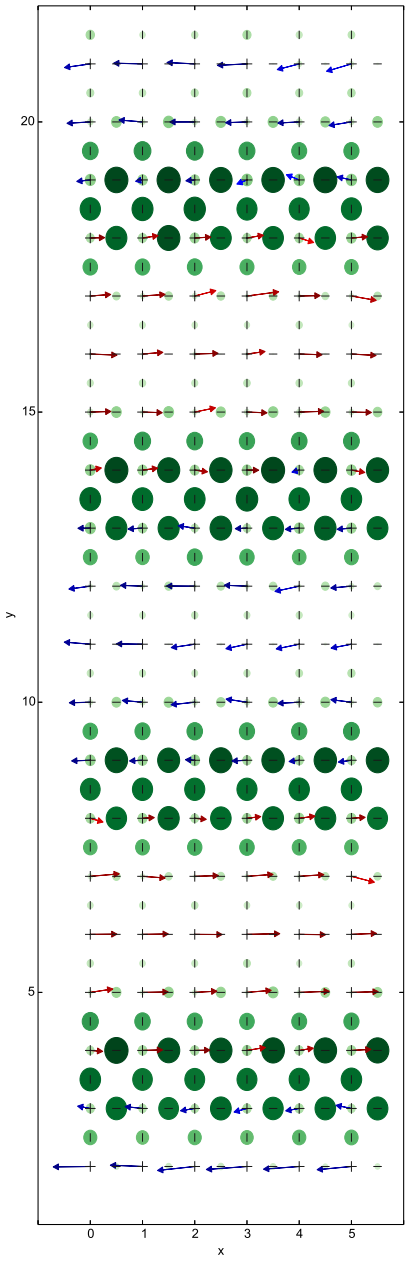

FIG. 3.4: (Color online) 2-D plot of the staggered spin vector, $(-1)^{x+y}\langle\hat{\mathbf{S}}(\mathbf{r})\rangle$, and charge density, $\langle\hat{n}(\mathbf{r})\rangle$, for $\Delta = 4.4$ and $h = 1/8$. The total staggered spins (arrows) are plotted as a projection in the x-z plane. The color of the arrow represents the angle between the spin on that site and an arbitrary reference spin. It can be thought of as a spin correlation and it runs from $(0, \pi)$. The spin on the O p-orbitals is negligible and omitted from the plot. The size of the circle is proportional to the density, with an overall background subtracted away. We neglect the first and last two rows to avoid the open boundaries and pinning field.

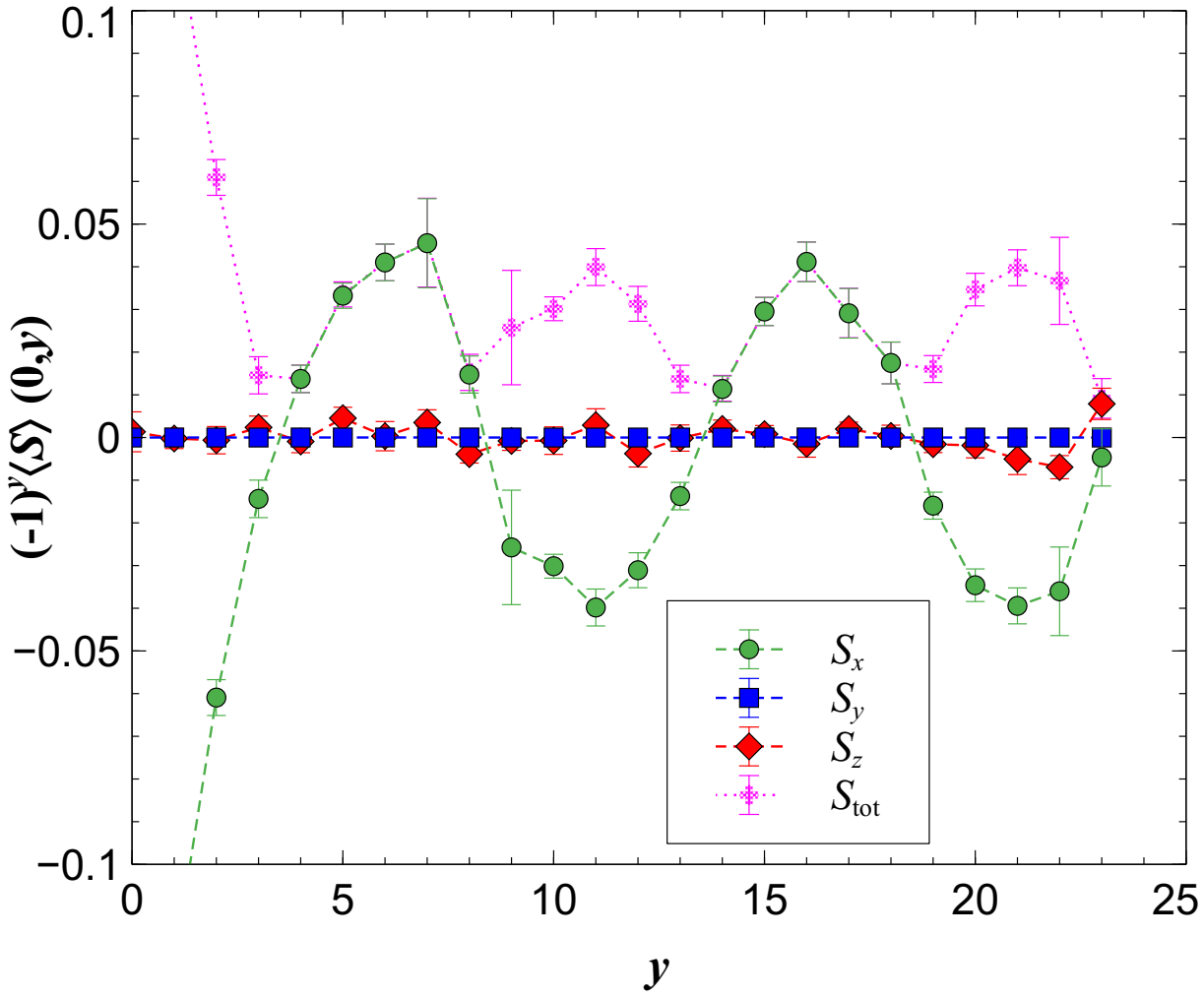

FIG. 3.5: (Color online) Plot of the components of the staggered spin vector along the line cut at $x = 0$, for the system in Fig. 3.4. The spin across the x–direction is antiferromagnetic. The majority of the spin vector lies in the S_x-direction, the same as the pinning field. A stripe phase with antiferromagnetic domains is seen.

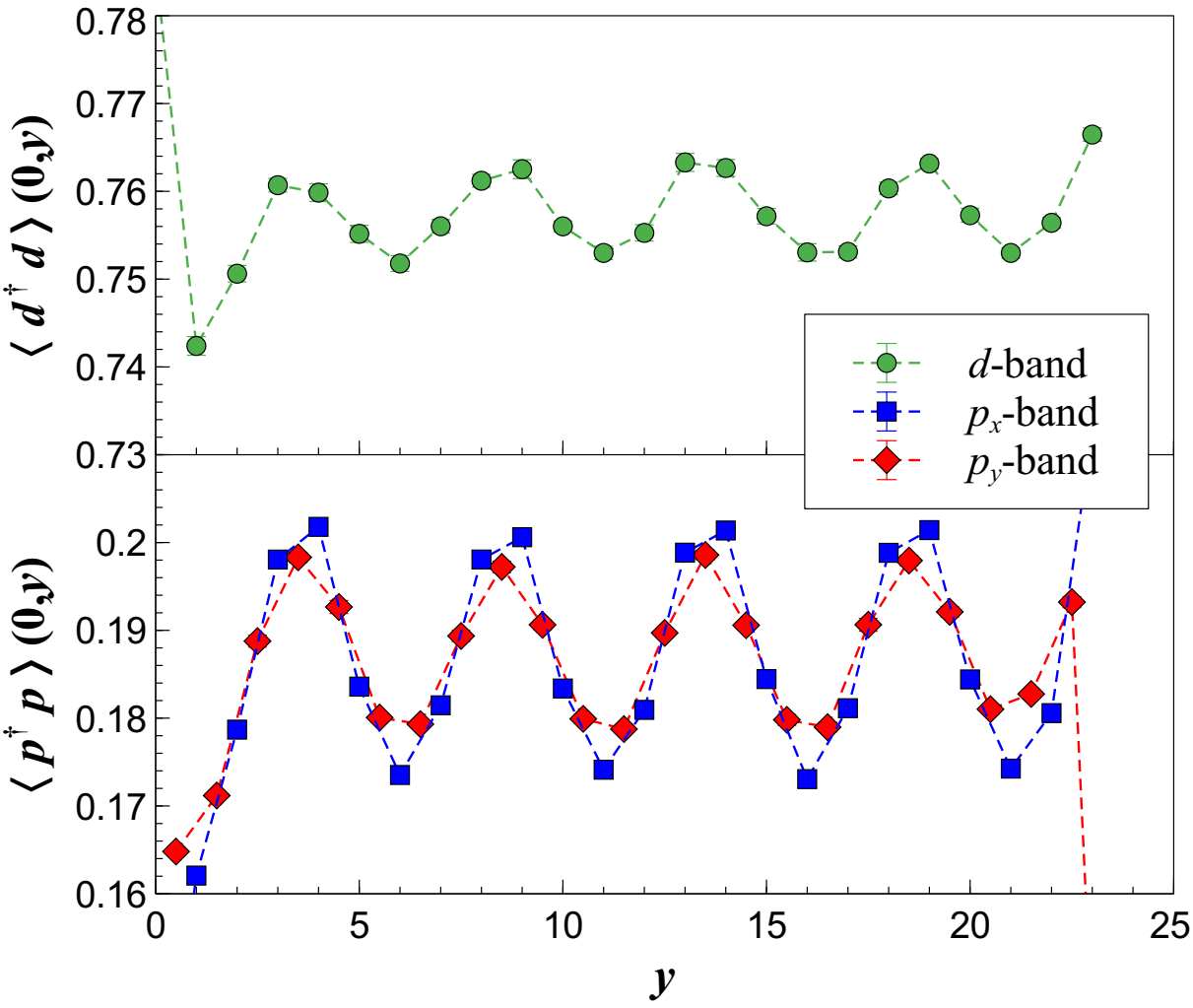

FIG. 3.6: (Color online) Plot of the occupations on different sites along the line cut at $x = 0$, for the system in Fig. 3.4. The Cu d-band occupation is shown in the top panel, and the O p_x and p_y-bands are plotted in the bottom. The hole density wave is correlated with the spin order in Fig. 3.5, with higher density at the domain boundaries. A small asymmetry is seen between p_x and p_y sites.

and homogeneous phases were used as initial trial wave functions. After several iterations, consistency is reached in many cases, allowing us to draw conclusions about the spin order in the ground state of the model as a function of the charge–transfer energy. We will highlight cases where different candidate spin orders are especially close and the balance is especially delicate, as indicated by the competition persisting with the self-consistency, and by closeness of their energies. The charge–order, on the other hand, appears to be very robust. Negligible effects are seen of the choice of the trial wave-function and of the system size on the density of holes on d and p orbitals.

At the higher value of the charge-transfer energy, $\Delta = 4.4$, a stripe–like phase appears. The spin and charge orders are illustrated in Fig. 3.4. The spin density on the p orbitals turns out to be negligible, so we only show the spin order on the Cu d orbitals. Figure 3.5 shows the spin order in more details, where spatially modulated spin densities along the y-direction are seen. The majority of the spin vector lies in the S_x-direction, the same as the pinning field. Figure 3.6 shows the charge occupations on the Cu d- and the O p_x- and p_y-sites, along the same line cut as the spin density above. From these figures we can visualize a regular distribution of AFM domains, separated by regions of high holes density, in particular on the p orbitals, where the antiferromagnetic order reverses direction. The "node" where the reversal occurs falls between two Cu sites, creating a "domain wall" between two AFM domains with two adjacent rows of aligned spins on the Cu d-orbitals. The wavelength of the spin order on the d orbitals is around 10 Cu sites, while hole densities show a corresponding oscillation with half the period and higher density tending towards the domain boundary of the spin order. These characters are similar to the behavior of stripe orders seen in the one-band Hubbard model.

The results at lower $\Delta = 2.5$ are shown in Figs. 3.7, 3.8 and 3.9. The spin order appears to be substantially smoother than at $\Delta = 4.4$. We interpret this as a signature of a shift toward a SDW phase, in contrast with the situation at $\Delta = 4.4$ which suggests

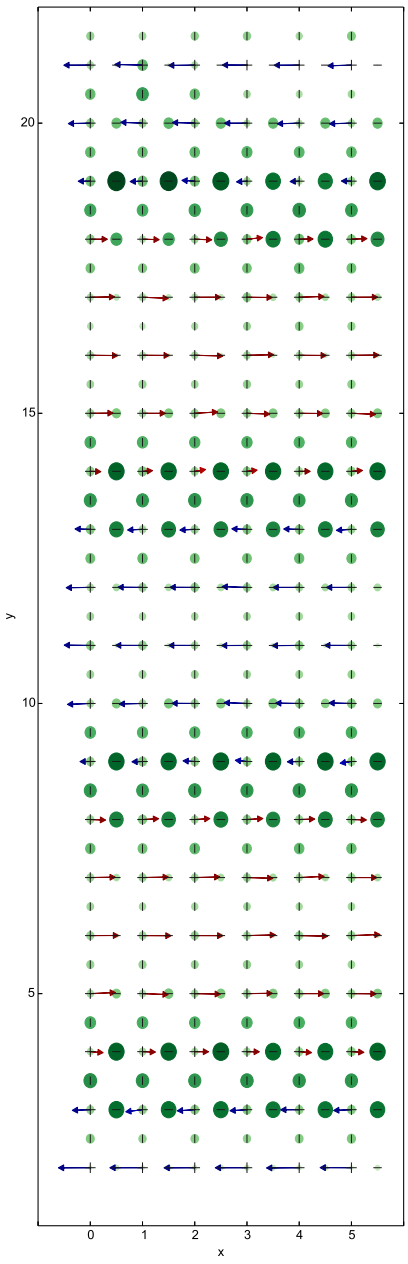

FIG. 3.7: (Color online) 2-D plot of the staggered spin vector and hole density, similar to Fig. 3.4, but for $\Delta = 2.5$.

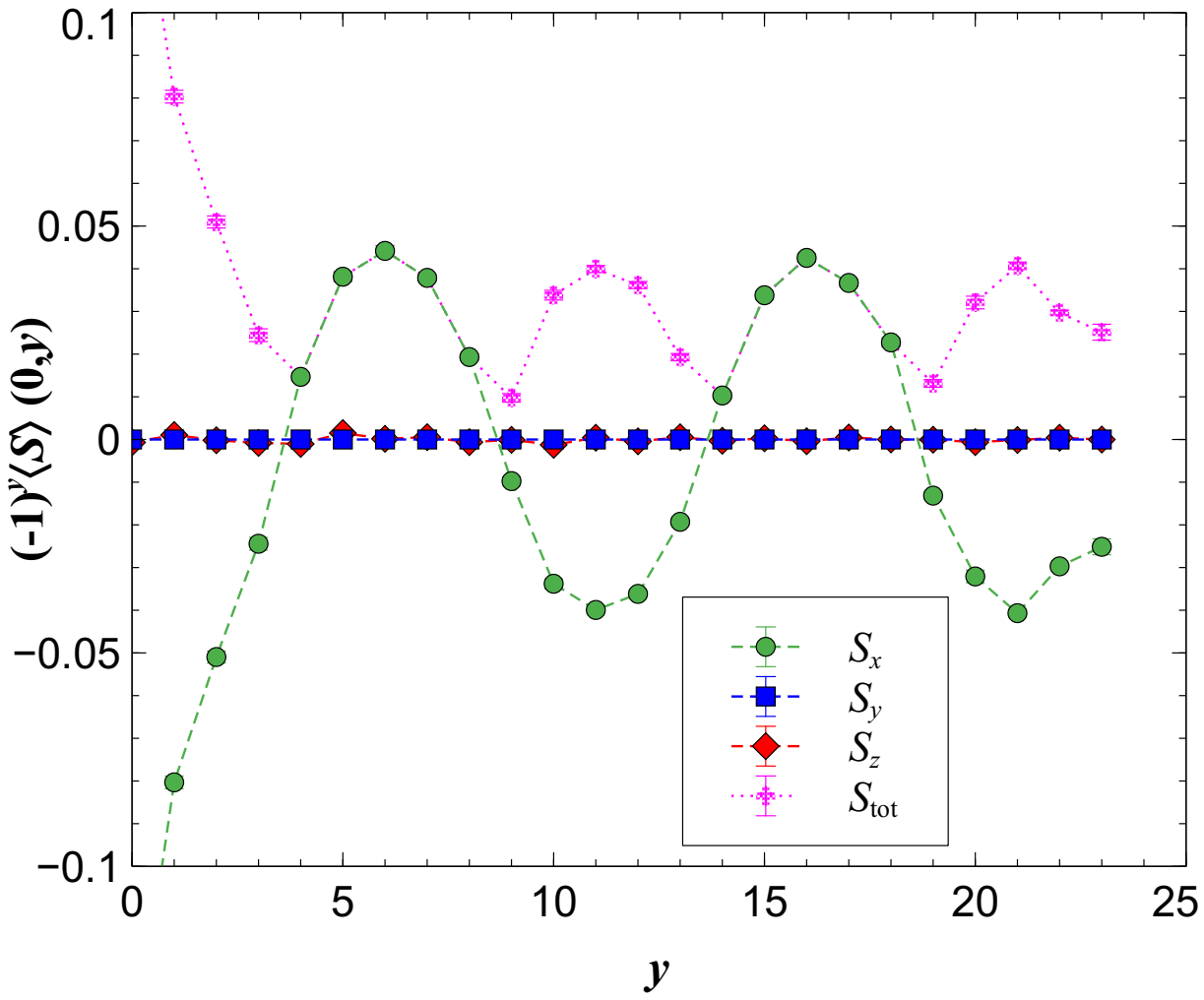

FIG. 3.8: (Color online) Plot of the components of the staggered spin vector along the line cut at $x = 0$, for the system in Fig. 3.7. The spin across the x–direction is antiferromagnetic. The majority of the spin vector lies in the S_x-direction, the same as the pinning field. A smooth antiferromagnetic spin-density wave is seen.

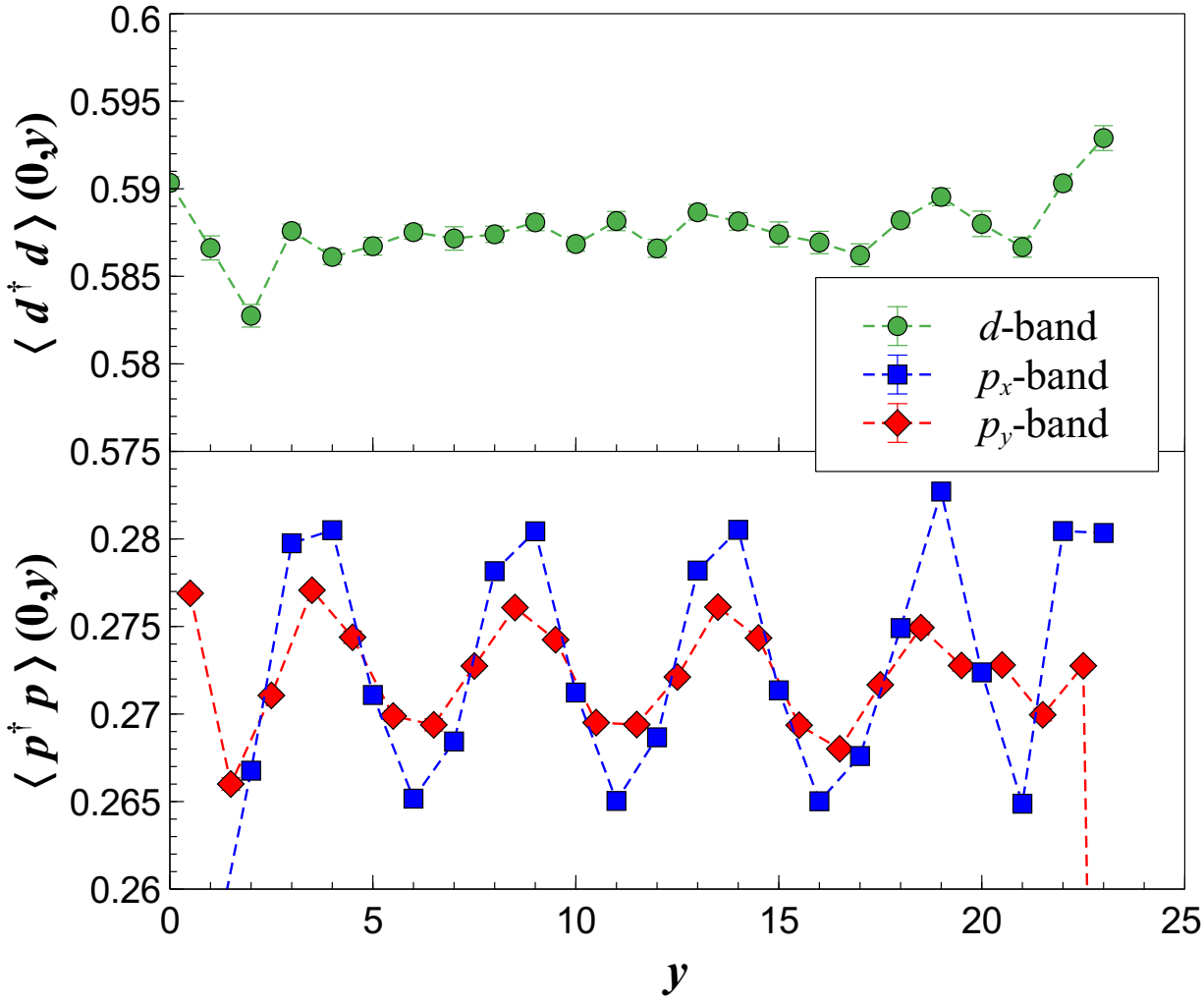

FIG. 3.9: (Color online) Plot of the occupations on different sites along the line cut at $x = 0$, for the system in Fig. 3.7. The Cu d-band occupation is shown in the top panel, and the O p_x and p_y-bands are plotted in the bottom. Densities on the d sites show little fluctuation, while occupations on the p sites are correlated with the spin density in Fig. 3.8, with p_x sites showing a much larger response.

a stripe-like order. For the charge order, the average Cu d-orbital occupation is nearly uniform and, as expected, greatly reduced with respect to $\Delta = 4.4$. There are still signs of a charge density wave on the O p-orbitals, although the amplitude is decreased by half compared to the charge wave at $\Delta = 4.4$. The maxima of the density of holes on the p orbitals correspond to the nodes of the staggered spin density on the d orbitals, as happens at the higher Δ. A significant asymmetry is seen in the occupancy of the O p_x and p_y sites, indicative of a strong nematic response to the SDW.

We find that a spiral order, pictured in Fig. 3.10, can become stable at $\Delta = 2.5$, and is nearly degenerate with respect to the SDW order within our resolution. The nature of the spiral order is similar to that seen in the generalized Hartree-Fock solution [46]. The AFQMC self-consistency loops can converge to a spiral state or a SDW depending on the starting trial wave function, and the resulting energies are extremely close. For example, in an 8×18 supercell the energy per site is $-9.0881(1)$ for the SDW state, versus $-9.0886(1)$ for the spiral state. The state also depends delicately on the details of the system. As in 8×18, the 6×18 system also shows the spiral state as having slightly lower energy; however, in the 8×20 supercell the energy ordering is reversed. We conclude that there is an extremely subtle cooperation or competition between the SDW and spiral phases in this region of the phase diagram. This suggests that, in the ground state of the Emery model, when the charge transfer energy is small, the spin order appears to be relatively "soft", while the charge density appears to be more homogeneous compared to higher values of Δ.

We next address the question: where do the doped holes go, as we move from the parent compound to the underdoped systems? As given in Table 3.2, we can monitor the average copper and oxygen occupation as a function of the charge–transfer energy Δ and doping h. Expectedly, as Δ is increased, the Cu d-orbital occupation increases both in the half–filled and the doped systems. The fraction of doped holes on the Cu d-bands

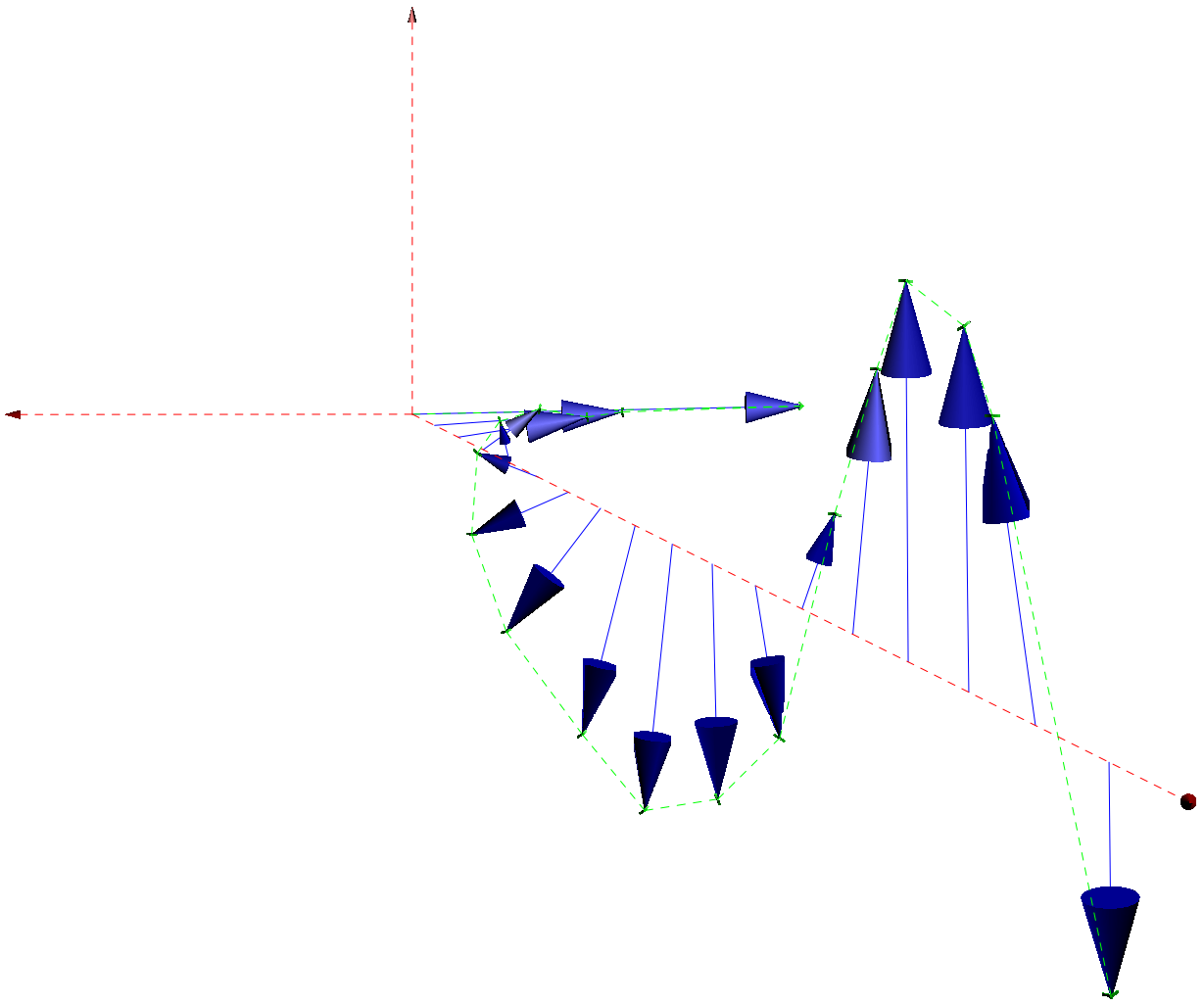

FIG. 3.10: (Color online) 3D plot of the staggered spiral spin order for an 8×18 system, at $\Delta = 2.5$ and $h = 1/8$. The staggered spin is shown, projected in three-dimensions along a line-cut at $x = 0$ plotting along the y-direction. Along the x-direction, the order remains perfect AFM.

remains smaller than 50% for both values of Δ. This means that as holes are doped, significantly more choose to occupy the p-bands over the Cu d-bands, giving a roughly equal distribution of the excess holes on the d and the two p sites. Interestingly, while the occupancy of d-bands is considerably higher at larger Δ, the percentage of the doped holes on the d-bands is slightly lower. Comparing these densities to the experimental results of Jurkutat et. al.[27], at $\Delta = 4.4$, our results for the net Cu d–orbital occupation for both the half–filling and 1/8–doped systems are consistent with the measured values in the Y-based cuprate family, with $n_d \approx 0.75$ and $n_p \approx 0.4$ ($h \approx 0.15$). At $\Delta = 2.5$, on the other hand, the results are consistent with the Cu d–orbital occupation of the Hg-, Bi-, and TI-based cuprate families, with $n_d \approx 0.59$ and $n_p \approx 0.54$ ($h \approx 0.13$). Also the Δ -dependence of the percentage of the doped holes occupying the d-bands appears to be consistent with the observations in the above-mentioned families of cuprates [27]. In fact, the results in [27] suggest that the fate of excess holes varies significantly across the different families: the percentage of holes occupying the d-orbitals is significantly larger in the Hg-, Bi-, and TI-based cuprate families than in the Y-based cuprate family, consistently with our results. This evidence indicates that the possibility to tune the charge-transfer energy in the Emery model gives us a very intriguing flexibility, by allowing us to capture differences among the different families of real materials, which is certainly not possible with the one-band Hubbard model.

As mentioned above, our explorations indicate that the charge and spin orders in the ground state of the Emery model, for the parameters studied in this work, appear along the x- or y-direction, i.e., the direction connecting a Cu site to one of its nearest neighbor O site. This led us to focus on elongated geometries of supercells, in order to accommodate potential collective modes. The artificial symmetry-breaking makes it easier to probe the density waves, but more delicate to study nematic orders, especially with the necessary reduction in supercell size in QMC compared to mean-field calculations. In the

latter, nematic orders readily appeared for intermediate Δ values [46]. Intra–unit cell nematic order has been observed both in theory [68, 69] and experiment[70]. Within our QMC calculations, signatures of nematicity are present in narrow $4 \times L_y$ systems; as L_x is increased, the spatially averaged nematic order $|n_{p_x} - n_{p_y}|$ fades away. However, locally, on the unit cell, nematic order is present in Fig. 3.6 and is very apparent at lower Δ in Fig. 3.9. This local nematic order accompanies the long-range spin and charge orders, which explicitly break the rotational symmetry in the lattice and in which the doped holes tend to organize close to the nodes of the spin density to induce asymmetry.

3.3.2 Momentum Distributions

We complement our detailed analysis of spin and charge orders in the Emery model with the calculation of the momentum distribution of the holes:

$$n_\sigma(\boldsymbol{k}) = \left\langle \hat{d}^\dagger_{\boldsymbol{k},\sigma} \hat{d}_{\boldsymbol{k},\sigma} + \hat{p}^\dagger_{x,\,\boldsymbol{k},\sigma} \hat{p}_{x,\,\boldsymbol{k},\sigma} + \hat{p}^\dagger_{y,\,\boldsymbol{k},\sigma} \hat{p}_{y,\,\boldsymbol{k},\sigma} \right\rangle , \tag{3.7}$$

where the creation (destruction) operators are the Fourier components of the operators appearing in the Hamiltonian in Eq. (3.1). We focus on the stripe phase at $\Delta = 4.4$ and on the spiral phase at $\Delta = 2.5$.

The top panel Figure 3.11 shows the total momentum distributions $n(\boldsymbol{k}) \equiv \frac{1}{2}(n_\uparrow(\boldsymbol{k}) + n_\downarrow(\boldsymbol{k}))$ in an 8×18 lattice for $\Delta = 4.4$ system and $\Delta = 2.5$, respectively. In the bottom panel, we plot the hole occupation in momentum space for the same two systems along a path in the Brillouin zone including the Γ point $\boldsymbol{k} = (0, 0)$, the antinodes $(0, \pi)$ and $(\pi, 0)$, the node $(\pi/2, \pi/2)$ and the corner of the Brillouin zone (π, π). We also show the momentum distribution of the corresponding half-filled systems, in order to probe the fate of the excess holes. At $\Delta = 4.4$, the momentum distribution appears to be smoother than at $\Delta = 2.5$, where the Fermi surface is much more defined and closer to the non-

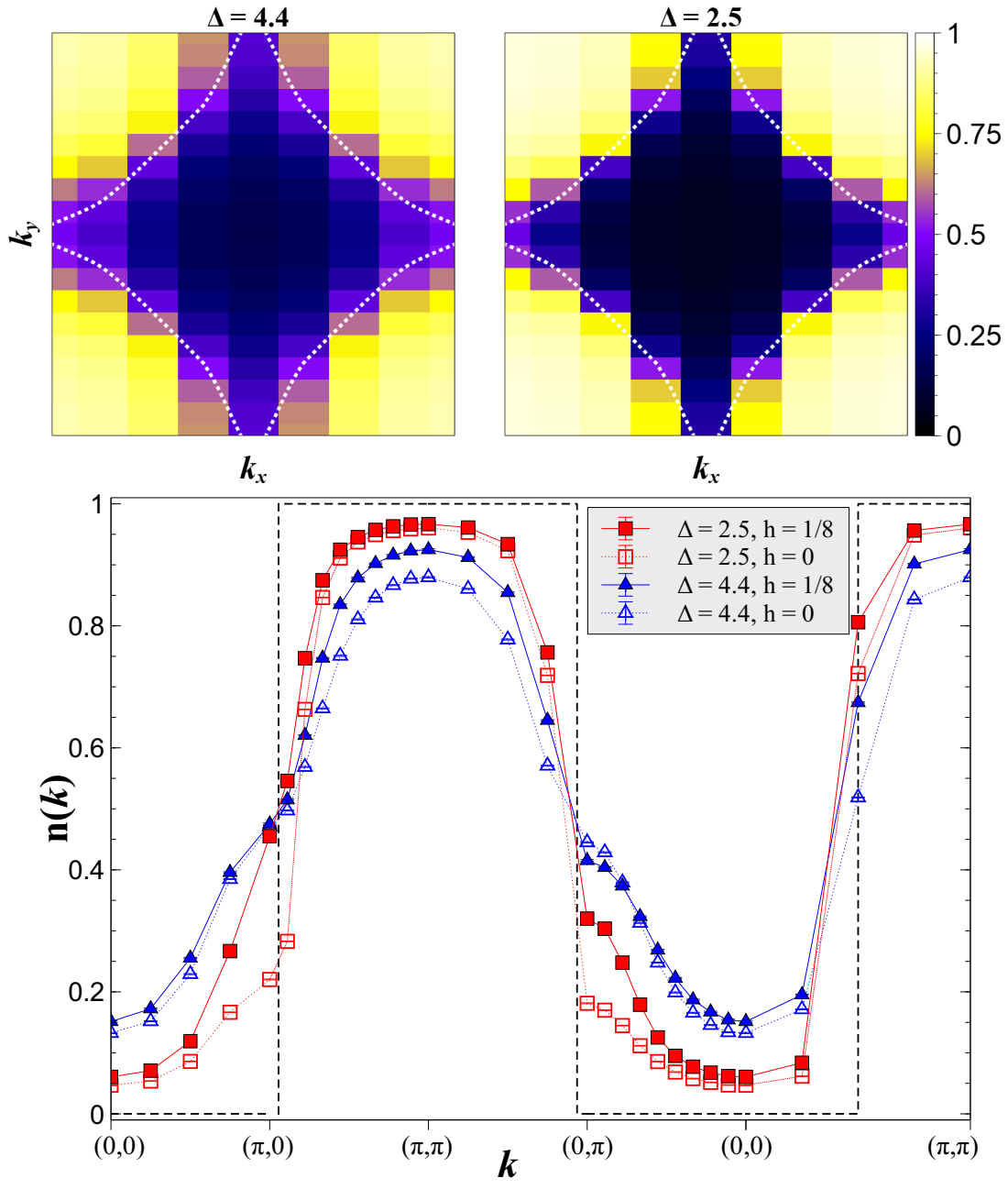

FIG. 3.11: (Color online) (Top) Total momentum distributions for $\Delta = 4.4$ (left) and $\Delta = 2.5$ spiral state (right) in the 8×18 system at $h = 1/8$. For reference, the corresponding non-interacting Fermi surface is plotted as a white dashed line. (Bottom) Hole occupation, $n(\boldsymbol{k}) \equiv \frac{1}{2}(n_\uparrow(\boldsymbol{k}) + n_\downarrow(\boldsymbol{k}))$, plotted along the path in momentum space $(0,0) \rightarrow (\pi,0) \rightarrow (\pi,\pi) \rightarrow (0,\pi) \rightarrow (0,0) \rightarrow (\pi,\pi)$ for the same systems in (a) along with their corresponding half-filled systems. For reference, the non-interacting system is plotted as the black dashed line.

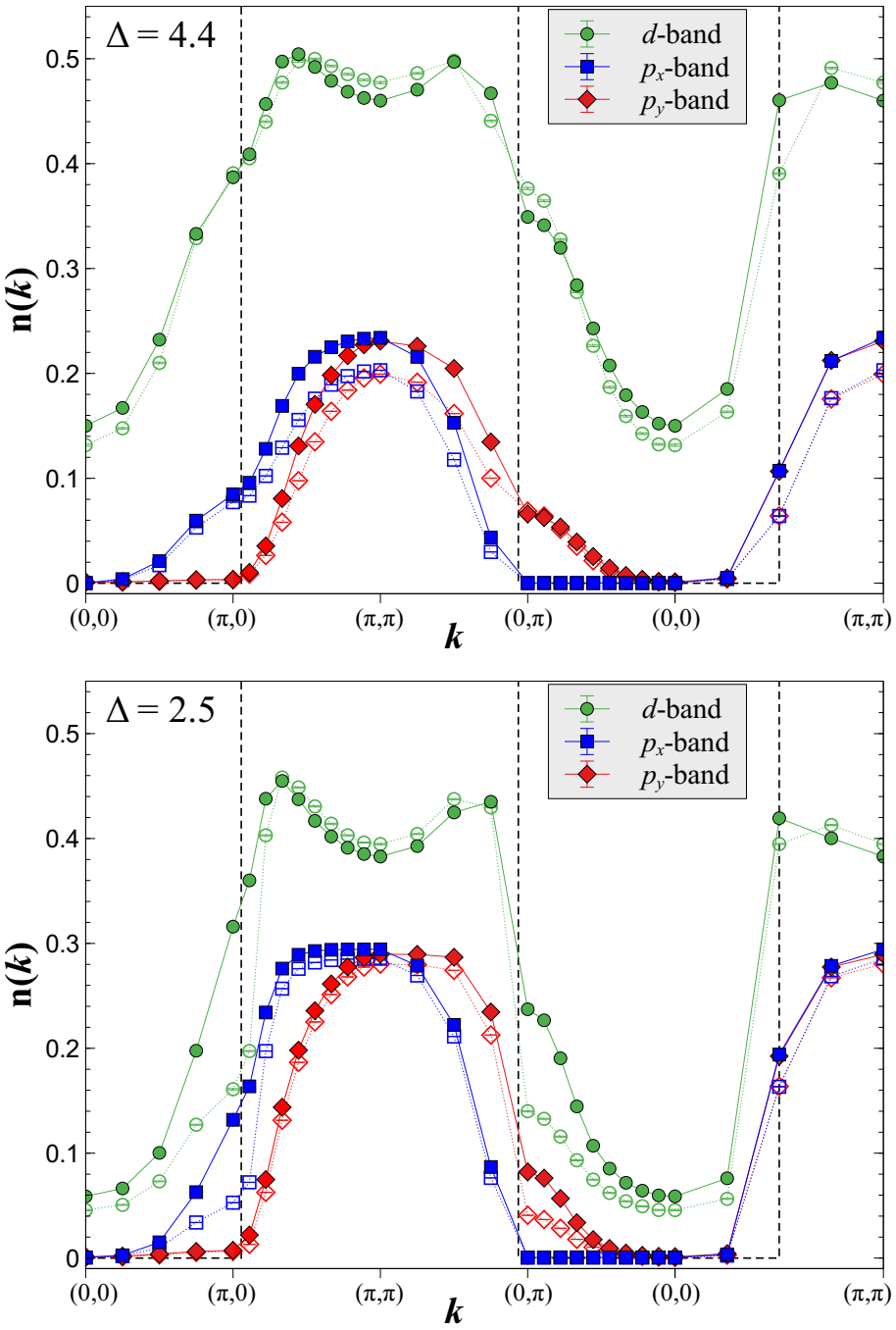

FIG. 3.12: (Color online) Band resolved hole occupation, $n(\boldsymbol{k}) \equiv \frac{1}{2}(n_{\uparrow}(\boldsymbol{k}) + n_{\downarrow}(\boldsymbol{k}))$, plotted along the path in momentum space $(0,0) \rightarrow (\pi,0) \rightarrow (\pi,\pi) \rightarrow (0,\pi) \rightarrow (0,0) \rightarrow (\pi,\pi)$ for the same systems in Fig. 3.11 (closed symbols) along with their corresponding half-filled systems (open symbols). For reference, the non-interacting system is plotted as the black dashed line.

interacting structure. This is consistent with the fact that the system is more correlated at $\Delta = 4.4$, where more holes are on the d orbitals and therefore we observe a higher number of double-occupancies. We observe a kink in the momentum distribution close to the antinodes, more prominent when $\Delta = 4.4$, consistent with a reconstruction the of the Fermi surface which would become more similar to a closed circle, as opposed to the open diamond-shape of the non-interacting Fermi Surface. Interestingly, the comparison with the half-filled results suggests that, in momentum space, the excess holes tend to occupy "internal" momenta close to (π, π) and the node (and symmetry-related points) in the system with $\Delta = 4.4$, while, for the smaller value of Δ, they mostly occupy the antinodal and the nodal regions, close to the non-interacting Fermi surface. In Fig. 3.12, we complement the information by showing the band-resolved momentum distribution, that is the the three terms in Eq. (3.7) separately. We observe that the asymmetry between p_x and p_y orbitals can be understood as a consequence of the geometry of the lattice and the definition of the hopping amplitudes in the hamiltonian Eq. (3.1): for a hole in the p_x orbital, for example, it is much more likely to have momentum in the x direction, which is evident in Fig. 3.12. We also have a more detailed picture of the fate of excess holes: when $\Delta = 4.4$, upon doping the holes tend to occupy the p orbitals close to (π, π), while a percentage of them appear to occupy both d and p orbitals close to the the node $(\pi/2, \pi/2)$. On the other hand, when $\Delta = 2.5$ the excess holes appear to occupy d and p orbitals with momenta close to the antinode $(0, \pi)$, as well as close to the node $(\pi/2, \pi/2)$. It thus appears that the system at $\Delta = 2.5$ finds it more convenient to organize the excess holes close to the non-interacting Fermi surface, and we argue that this favors an interesting nesting property, which becomes evident in the spin-resolved momentum distribution and gives rise to the spiral order which we observe.

In fact, a remarkable difference between the two values of the charge-transfer energy is seen in spin symmetry-breaking. In the stripe-phase at $\Delta = 4.4$, the difference between

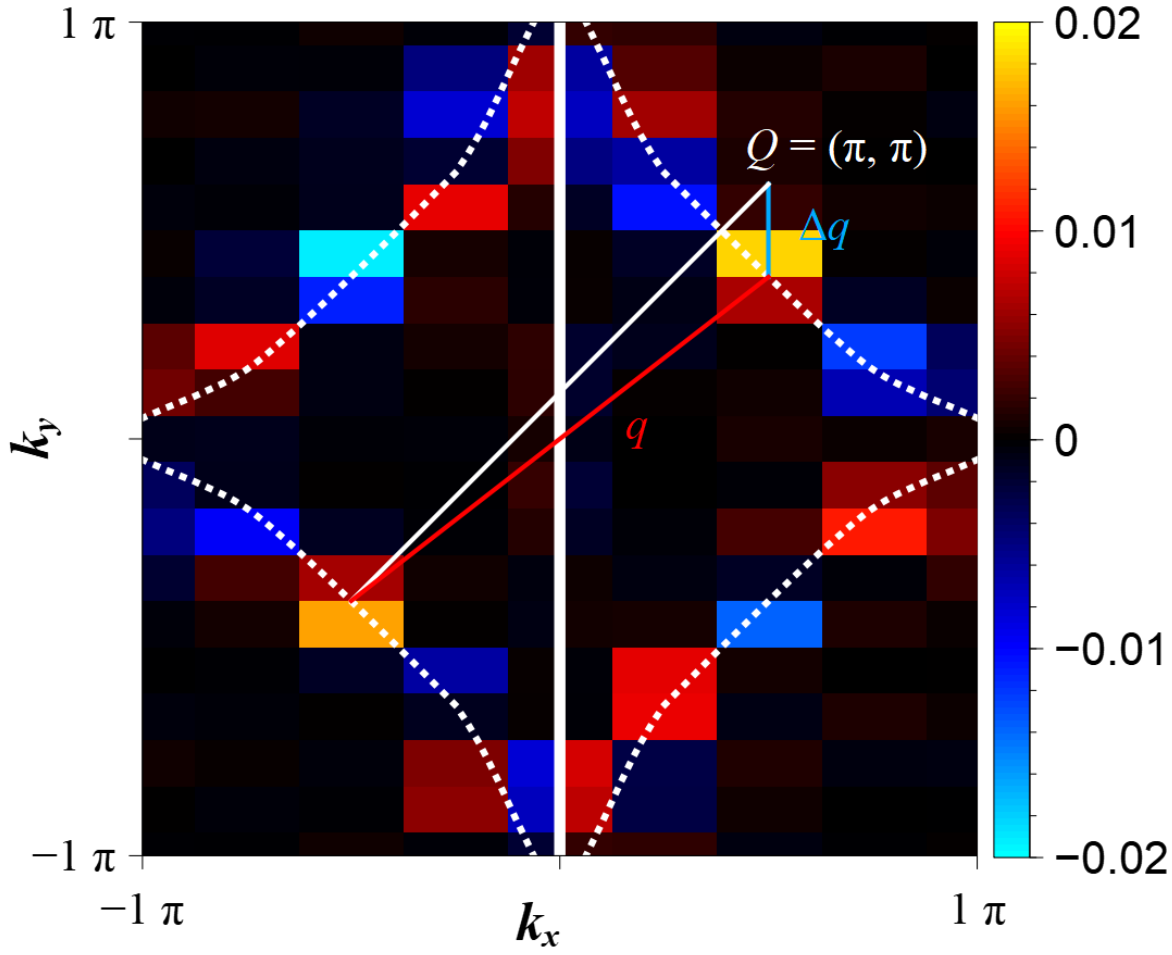

FIG. 3.13: (Color online) The difference between the spin-up and spin-down momentum distributions in the spiral state at $\Delta = 2.5$ with $h = 1/8$. To guide the eye to complimentary nesting points on the Fermi surface, for $k_x < 0$, we plot $n_\uparrow(\boldsymbol{k}) - n_\downarrow(\boldsymbol{k})$, and for $k_x > 0$, we plot $n_\downarrow(\boldsymbol{k}) - n_\uparrow(\boldsymbol{k})$. We plot the nesting vector, q, in red, $Q = (\pi, \pi)$ in white, and $\Delta q = q - Q$ in blue.

$n_\uparrow(\boldsymbol{k})$ and $n_\downarrow(\boldsymbol{k})$ is negligible, and $n_\uparrow(\boldsymbol{k}) - n_\downarrow(\boldsymbol{k})$ is zero within statistical error. In the spiral phase at $\Delta = 2.5$, $n_\uparrow(\boldsymbol{k})$ and $n_\downarrow(\boldsymbol{k})$ are not the same. The difference $n_\uparrow(\boldsymbol{k}) - n_\downarrow(\boldsymbol{k})$ is crucial for the spiral order, as we extensively discussed at the mean-level in our earlier study [46]. In Fig. 3.13, we compare the subtle differences between $n_\uparrow(\boldsymbol{k})$ and $n_\downarrow(\boldsymbol{k})$. To guide the eye to complimentary points around the Fermi surface, for $k_x < 0$, we plot $n_\uparrow(\boldsymbol{k}) - n_\downarrow(\boldsymbol{k})$ and for $k_x > 0$, $n_\downarrow(\boldsymbol{k}) - n_\uparrow(\boldsymbol{k})$ for the spiral state at $\Delta = 2.5$. Complimentary points are where $n_\uparrow(\boldsymbol{k}) - n_\downarrow(\boldsymbol{k}) = n_\downarrow(\boldsymbol{k}') - n_\uparrow(\boldsymbol{k}')$. The vector connecting $\boldsymbol{k}$ and $\boldsymbol{k}'$ is the nesting vector, q, plotted as the red line. The resolution from QMC is limited by the finite size of the system, in particular in the x direction, such that the exact nesting vector is difficult to infer. The results in Fig. 3.13 allows us to infer the difference $\boldsymbol{\Delta q} = \mathbf{q} - \mathbf{Q}$ between the spiral nesting vector $\mathbf{q}$ and the wave-vector describing the AFM order $\mathbf{Q} = (\pi, \pi)$ The resulting $\boldsymbol{\Delta q}$ is along the y-direction, consistently with the observation of the long-range order along y: a modulation from AFM order manifesting the formation of the spiral state. We estimate $\Delta q \simeq \pi/9$ in momentum space, which corresponds to a wavelength of 9 Cu sites in real space. This is nearly consistent with the wavelength of 10 Cu sites discussed in the previous section.

3.3.3 Zhang-Rice Singlets and Localization

The Zhang-Rice (ZR) singlet is theorized to play an important role in the superconducting state of the Cuprates [21]. It also has ties to the formalism of the one–band Hubbard model. Within our CP-AFQMC framework, is is straightforward to compute the density of ZR singlets in the ground state of the three–band model. In order to make the calculations, we define the creation operator of a singlet around a Cu site i as follows:

$$\hat{c}_i^\dagger = \frac{1}{\sqrt{2}} \left(\hat{d}_{i,\downarrow}^\dagger \hat{\phi}_{i,\uparrow}^\dagger - \hat{d}_{i,\uparrow}^\dagger \hat{\phi}_{i,\downarrow}^\dagger \right) \tag{3.8}$$

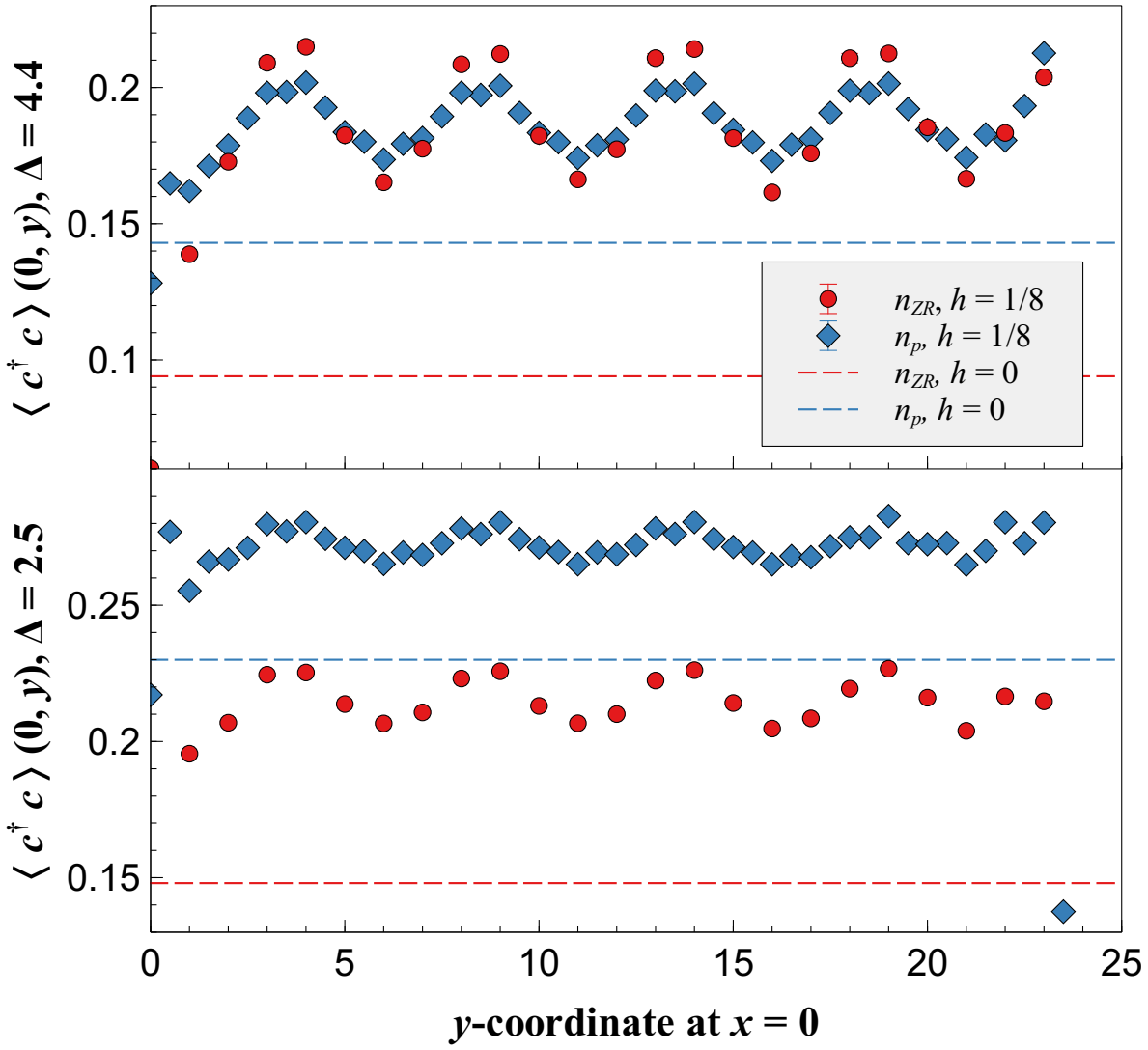

FIG. 3.14: (Color online) Zhang-Rice singlet density for both $\Delta = 4.4$ and 2.5. The results are plotted along a line cut $x = 0$, alongside the Oxygen p_x and p_y-orbital densities for both doped ($h = 1/8$) and half–filled ($h = 0$) systems. Plots are taken along a line cut at $x = 0$. Note: the overall scale is the same for both values of Δ; however there is an overall shift.

where the operator $\hat{\phi}^{\dagger}_{i,\sigma}$ creates a hole delocalized on the four surrounding p:

$$\hat{\phi}^{\dagger}_{i,\sigma} = \frac{1}{2}\left(-\hat{p}^{\dagger}_{i+\hat{x}/2,\sigma} + \hat{p}^{\dagger}_{i+\hat{y}/2,\sigma} + \hat{p}^{\dagger}_{i-\hat{x}/2,\sigma} - \hat{p}^{\dagger}_{i-\hat{y}/2,\sigma}\right) \tag{3.9}$$

The local density of ZR singlets is computed as $\langle \hat{c}^{\dagger}_i \hat{c}_i \rangle$ and is plotted in Fig. 3.14, where we include also the results at half-filling for comparison.

At $\Delta = 4.4$, there is a strong enhancement in the presence of ZR singlets compared to the parent compound. As mentioned earlier, a larger percentage of the doped holes occupy the O p orbitals compared to lower Δ. A larger portion of the holes on the p orbitals appear to be involved in forming the ZR singlet. The hole density on Cu d is significantly higher here. At $\Delta = 2.5$, the average overall density of ZR singlets is actually higher than the value at $\Delta = 4.4$. As seen in Table 3.2, n_d is substantially lower here, so effectively the system is at a larger doping and hence weaker correlation, consistent with earlier observations. The wave amplitude of the ZR singlets is significantly smaller, consistently with the dependence of the amplitude of the spin density waves on Δ discussed earlier.

In our QMC study of the Emery model at half–filling[34], a phase transition was clearly identified between an antiferromagnetic insulating state, which is stable at high values of Δ, and a non–magnetic metal state which exists below $\Delta = 3.0$. One of the probes that we used to detect whether the system was insulating or conducting was the Resta-Sorella localization estimator[71]. Here we also study the localization of the holes in the doped systems. However, since we have systematically used open boundary conditions, we will use as a probe the Quantum Metric Tensor (QMT) [71], defined by the 2×2 matrix:

$$Q_{ab} = \frac{1}{N}\big(\langle \hat{r}_a \hat{r}_b \rangle - \langle \hat{r}_a \rangle \langle \hat{r}_b \rangle \big), \quad a, b = x, y \tag{3.10}$$

The position operator is defined as:

$$\hat{r}_a = \sum_{i=1}^{M} \sum_{\alpha=d,p_x,p_y} \left(r_{i,\alpha}\right)_a \sum_{\sigma} \hat{\alpha}^{\dagger}_{i,\sigma} \hat{\alpha}_{i,\sigma} \,, \tag{3.11}$$

where $\left(r_{i,\alpha}\right)_a$ is the cartesian a-component of the position vector of the orbital α in the unit cell i. The diagonal components of the QMT provide a measure of the localization of the holes in the system. In particular, since our supercells are elongated in the y direction, we focus on the size dependence of the Q_{yy}-component of the QMT under open boundary condition. If $Q_{yy} \to \infty$ as $L_y \to \infty$, then we have a conductive state; if Q_{yy} converges to a finite value in the bulk limit, the system is an insulator.

In Fig. 3.15, we plot Q_{yy} computed from AFQMC as a function of lattice size. We did not observe any significant difference between results for $L_x = 6$ and $L_x = 8$, indicating that the role of the transverse direction is negligible. For clarity and to maximize the length of the extrapolation, we only show results for $6 \times L_y$ systems. The results at half-filling for both values of the charge-transfer energies are also shown for comparison, and provide a reference relating to our previous study [34], which established that the ground state of the Emery model at half-filling is conductive at $\Delta = 2.5$ and insulating at $\Delta = 4.4$.

In the 1/8-doped systems, the QMT increases as a function of the supercell size for both values of Δ. Interestingly, the slopes of Q_{yy} as functions of L_y for the two doped systems lie between the corresponding results at half-filling. Although these system sizes are much larger than previously possible by accurate many-body computations, we are still somewhat limited at $L_y = 24$, especially for extrapolation of the asymptotic behavior and we are not able to provide a conclusive answer about whether the ground state of the model is insulating or conductive. Nevertheless, we can extract some important qualitative considerations. At $\Delta = 4.4$ the holes become less localized as we dope the system starting from the parent compound. This is very interesting, especially if the holes at $\Delta = 4.4$

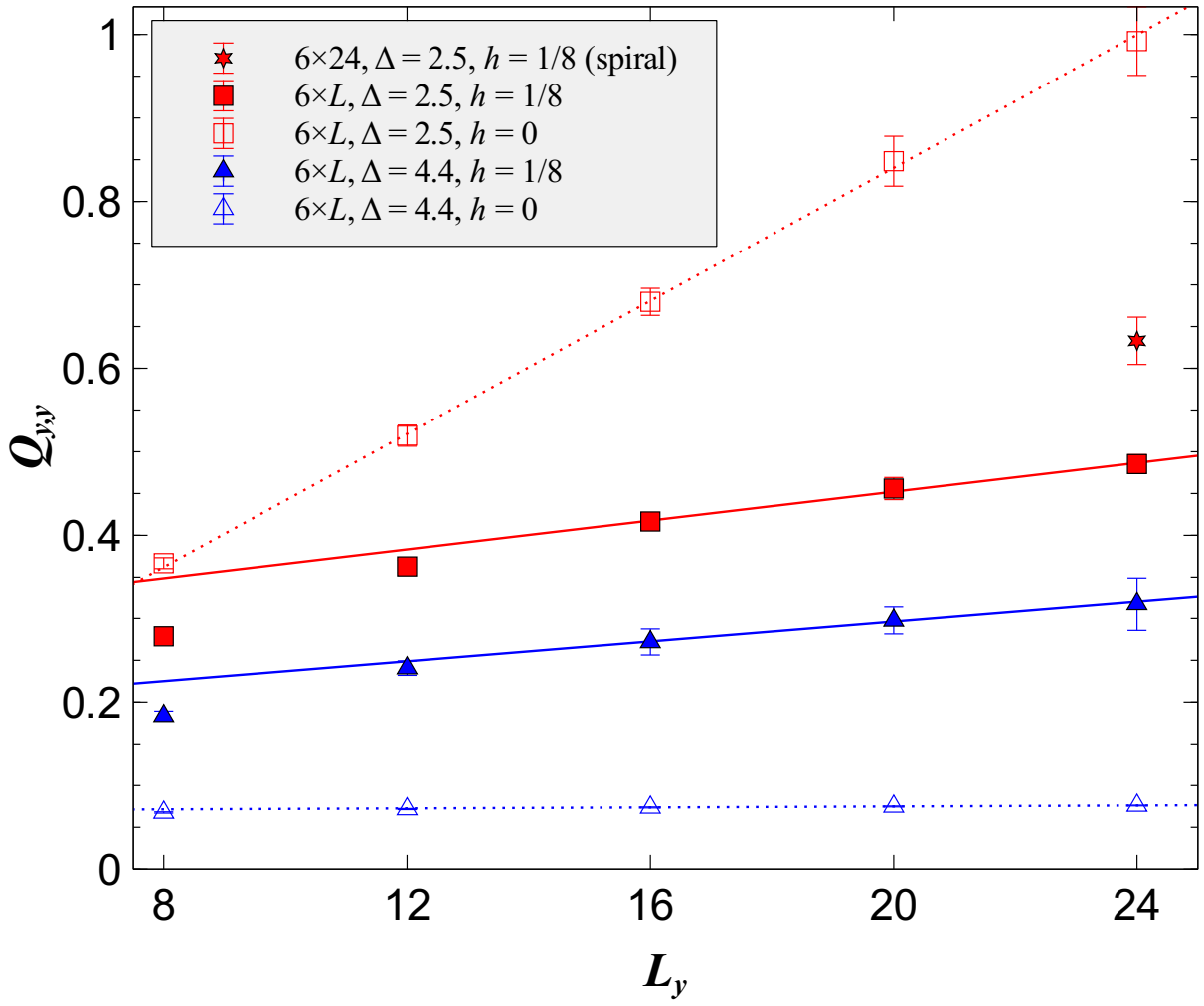

FIG. 3.15: (Color online) Plot of the (y, y)–component of the QMT as a function of L_y. At $\Delta = 4.4$, the value of the QMT is saturated for large lattice sizes suggesting an insulating state. For both $\Delta = 2.5, 4.4$, the QMT appears to be still increasing suggesting conducting states.

are, indeed, delocalized, which unfortunately we cannot state with certainty. The results would suggest that even though the system exhibits stripe order, it also shows signs of delocalized holes, though potentially weakly delocalized. This is counter–intuitive, since stripe order pulls charge at the domain boundaries, thus creating huge potentials for mobile holes to overcome. In addition, this is highly unintuitive, as domain walls suggest high concentrations of localized charge. At $\Delta = 2.5$, very interestingly, the comparison with the results at half-filling shows that the excess holes substantially reduce the overall mobility of the system. The resulting systems still show evidence of delocalized holes, with a mobility that seems higher with respect to the case at higher Δ. The mobility appears to be even higher in the spiral phase, which is not very surprising since spiral order systems create fewer (ideally no) domain walls, and therefore are conceptually more conducting.

Our results for the localization of the holes in the Emery model may have an intriguing connection with the physics of the real materials, as it is well known that some families of the cuprates do not have a stable parent compound. The fact that ground state of the model becomes conductive at half-filling for small values of the change-transfer energy, is indeed consistent the absence of an antiferromagnetic and insulating parent compound. Although it is possible that the choice of the parameters of the model may not be appropriate to describe the physical systems in some regimes, our probe of the localization may be capturing some important physical mechanism which underlies the delicate doping dependence of the physical properties of the cuprates. An even more exciting question is: may this mobility be somehow related to superconductivity? This will be deferred to future studies, as we will need significant methodological advances to have a resolution that would allow us to detect superconducting correlations in the ground state of the Emery model in some regions of the parameter space.

Finally, we also computed the hopping amplitudes, namely the nearest-neighbor components of the one body density matrix, as listed in Table 3.2. These can be relevant to

experiments, for example in scanning tunneling microscopy [72]. The matrix elements provide an indicator of the amplitude for the holes to hop between nearest neighbor orbitals, and thus they yield a further probe the local mobility of the holes. From the results it is evident that the local mobility of the holes increases as we decrease the value of the charge-transfer energy, consistent with the QMT results above.

3.3.4 Electron-Hole Asymmetry

An important feature of the Cuprates is the asymmetry in the hole doped and electron doped phase diagrams, which is not captured by the one-band Hubbard model with nearest-neighbor hopping. Anti-ferromagnetic correlations in the hole-doped case rapidly melt as holes are added to the system. In the electron doped case, on the other hand, the anti-ferromagnetic state survives for higher values of electron doping. Although the main focus of this work is on the hole-doped regime, our methodology allows us to compute physical properties of electron-doped systems as well. In Fig. 3.16, we consider two 6×16 systems at $\Delta = 4.4$ in the three-band model. On the left is a hole doped system ($h = 1/8$) and the behavior we observe consistent with what we have seen in Sec. 3.3.1: a stripe phase in which the spin is modulated in phase with a charge wave. On the right is an electron doped system (negative hole doping $h = -1/8$) and we see a strikingly different behavior from the corresponding hole-doped system. We observe a phase separated system in which a significant percentage of the doped electrons are localized on the d-orbitals near the pinning line at $y = 0$. Far enough from the pinning field, the systems aligns in a homogenous AFM order, consistently with the behavior of real materials. In Fig. 3.17 we show a quantitative comparison for the band-resolved hole density between the hole-doped (filled symbols) and the electron-doped (empty symbols) systems. It is evident that the majority of the doped electrons occupy d-orbitals, while doped holes tend to go to the p-orbitals with higher

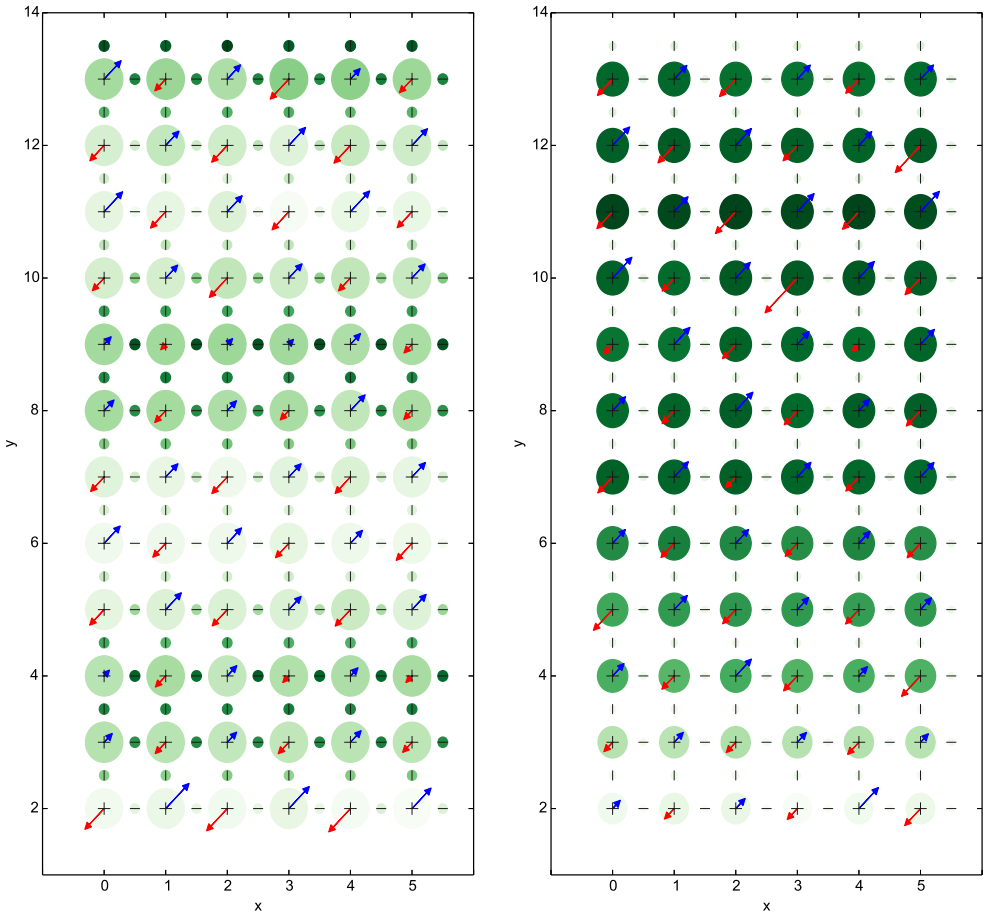

(a) $h = 1/8$ (b) $h = -1/8$

FIG. 3.16: (Color online) 2-D plot of the x-component of the total spin vector, $\langle \hat{\mathbf{S}}_x(\mathbf{r}) \rangle$, and charge density, $\langle \hat{n}(\mathbf{r}) \rangle$, for $\Delta = 4.4$ for both (a) a hole doped system, $h = 1/8$, and (b) an electron doped system $h = -1/8$. The spins (arrows) are plotted as a projection in the x- plane. The color of the arrow represents the directionality of the spin in the x-direction, blue being positive and red negative, to highlight AFM order. The spin on the O p-orbitals is negligible and omitted from the plot. The size of the green circles are proportional to the hole density. To highlight density waves, we plot the color of the circles scaled to the maximum and minimum hole densities for the respective systems. We neglect the first and last two rows to avoid effects at the open boundaries and pinning field.

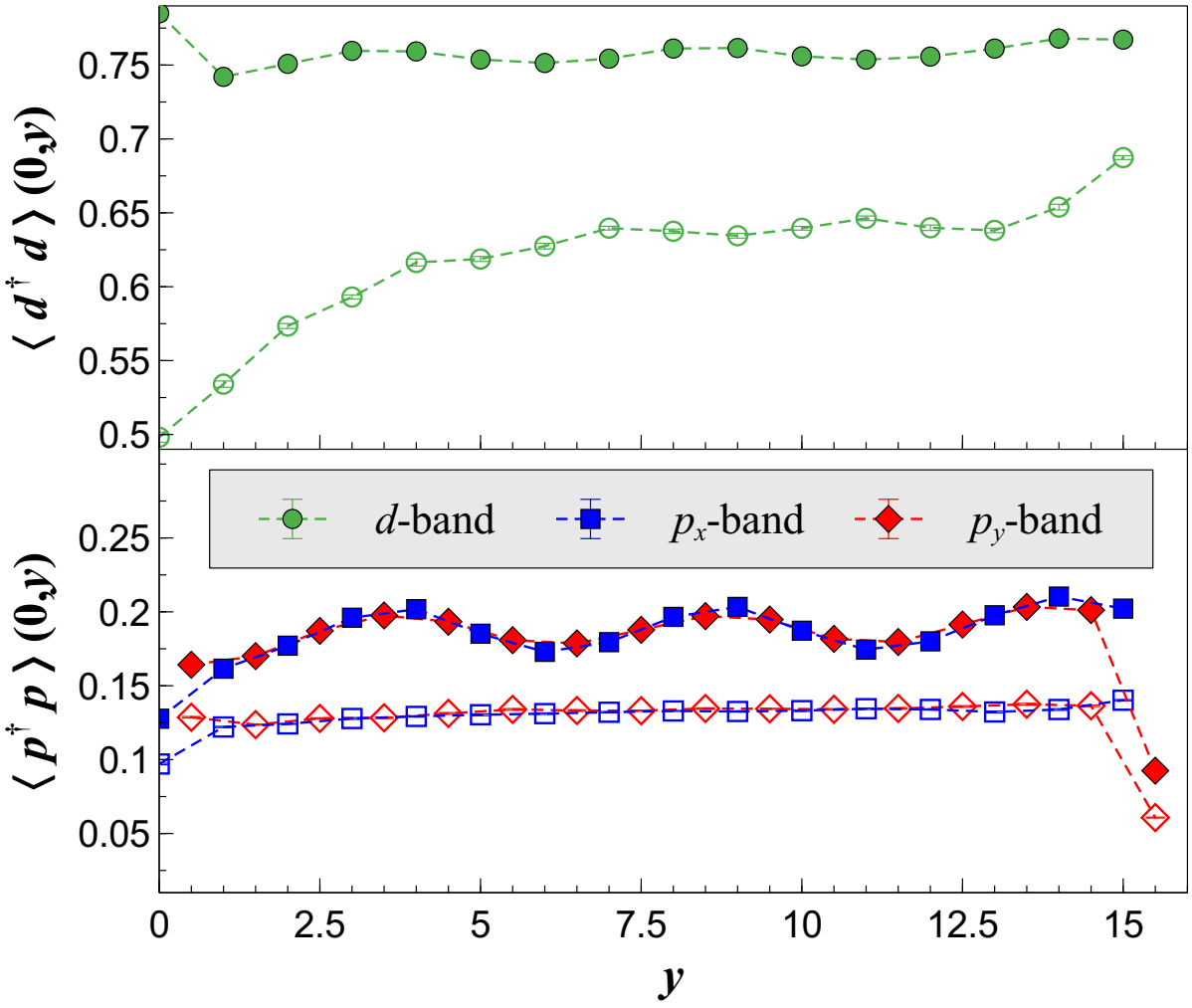

FIG. 3.17: (Color online) Plot of the occupations on different sites along the line cut at $x = 0$, for the systems in Fig. 3.16. The Cu d-band occupation is shown in the top panel, and the O p_x and p_y-bands are plotted in the bottom. Closed symbols represent the hole doped system ($h = 1/8$) and open symbols represent the electron doped system ($h = -1/8$).

probability; the system appears to phase separate, in order to build an optimal density to form an homogenous AFM order, consistent with the experimental observation. The ability to capture this electron-hole asymmetry is another strong indication that the Emery model provides indeed a significant step forward with respect to the simple particle-hole symmetric one-band model in the plan of finding a realistic model for the Cuprates.

3.4 Summary and Discussion

Using CP-AFQMC with the latest developments, we have studied the hole–doped, three–band Hubbard model as a function of the charge–transfer energy. The magnetic and charge orders are determined at two representative values of Δ. Accurate numerical results are obtained from computations on large supercells to provide systematic information on a variety of ground-state properties. Based on the performance of CP-AFQMC both in simplified models and in real materials, these results represent the state-of-the-art in many-body computation for the combination of accuracy and approaching the bulk limit in the model. Thus the detailed data will serve as useful benchmarks for future theoretical and computational studies.

Comparing the computed average Cu and O occupations to experimental studies, we find that, with the parameters adopted, the Emery model at $\Delta = 4.4$ most closely relates to the Y-family of Cuprates, while at $\Delta = 2.5$, it most resembles the Hg-, Bi-, TI-based families. At $\Delta = 4.4$, we observe a robust stripe order consisting of spin density waves with corresponding charge density modulation, creating antiferromagnetic domains with a phase change across the domain walls where the density is higher. At $\Delta = 2.5$, on the other hand, the spin order was more nuanced with several competing orders sensitive to the system sizes and geometries and initial trial wave functions. We find a spin density wave state, characterized by modulated AFM order along with a weak charge density wave only

on the O p-sites, as well as a spin spiral state in which the spins cant in a randomly chosen plane along the propagation direction with essentially uniform charge density. These states are separated by an energy scale that is almost degenerate within the (high) resolution of the AFQMC calculation, suggesting a possible quasi-degeneracy of the ground state of the Emery model.

We characterized the properties of these states with detailed information on the densities in supercells with a pinning field applied on one side to break translational symmetry. We also computed average hopping amplitudes and energetics as detailed in Table 3.2. The momentum distributions were analyzed and compared for the stripe and spiral states. We also observed that the holes become more delocalized as the charge–transfer energy was reduced, by measurements of the QMT and the one–body density matrix. The spiral spin state, which has a nearly constant charge density, has holes substantially more delocalized than in the stripe state. Finally, we explored the relation between hole and electron doping in the context of the Emery model and we found an important asymmetry, consistent with the phase diagrams of the real materials.

At the mean field level, we had showed that the spin order had an extremely nuanced and rich phase diagram ranging from orders such as diagonal Magnetic Domain Walls and spin spirals. Though we didn't observe any diagonal order in the QMC results, the spin order was still very rich and subtle. At $\Delta = 4.4$, we observed a robust stripe order consisting of spin density waves with commensurate density modulation, creating antiferromagnetic domains with a phase change across the domain walls where the density is higher. At $\Delta = 2.5$, on the other hand, the spin order was more nuanced with several competing orders depending on the system geometries and initial trial wave functions. We found a spin density wave state, characterized by modulated AFM order along with a weak density wave only on the oxygen p–orbitals, as well as a spin spiral state in which the spin cants in a randomly chosen plane along the propagation direction. The energy scales were ex-

tremely close within our resolution, suggesting a possible quasi-degeneracy of the ground state of the Emery model in this point of the phase diagram.

We computed also the momentum distributions for both the stripe phase at $\Delta = 4.4$ and the spiral phase at $\Delta = 2.5$ resulting in two completely different orders in momentum space. At $\Delta = 4.4$, we see a symmetry between spin-up $n_\uparrow(\boldsymbol{k})$ and spin-down $n_\downarrow(\boldsymbol{k})$, consistent with a linear spin-density wave order. At $\Delta = 2.5$, on the other hand, when our estimate of the ground state displays a spiral order we see a break in the symmetry between $n_\uparrow(\boldsymbol{k})$ and $n_\downarrow(\boldsymbol{k})$ along the Fermi surface. This creates an highly non-trivial nesting property that is consistent with the canting of the spin density that we observed.

The ground state of the model at the considered doping appears to depend on the charge transfer energy in a highly nontrivial way: we find subtle differences in the spin order and significant differences in the charge order, spin resolved momentum distributions, density of Zhang-Rice singlets, and localization properties. Our results suggest the at $\Delta = 4.4$ the doped system creates a stripe–like phase [3] that is weakly conducting. As we reduce the charge–transfer to $\Delta = 2.5$, the system prefers more subtle, linear spin density wave (SDW) and spiral orders with small density modulation on the oxygen p–orbitals and shows stronger signs of hole delocalization through measurements of the quantum metric tensor and one–body density matrix.

We also computed a few additional, and in some sense more "exotic", properties with interest to the high-T_c community. We detected a Zhang–Rice singlets density wave, highly correlated with the density wave on the oxygen p–orbitals. We also observed the holes become more delocalized as the charge–transfer energy was reduced by measurements of the quantum metric tensor and the nearest-neighbor components of the one–body density matrix. Compared to our half–filling study, these results are consistent and show an increase in delocalization as the model is doped.

TABLE 3.2: Table of measured ground-state properties at doping $h = 1/8$, for different supercell sizes $M = L_x \times L_y$, at two different values of charge transfer energy Δ. All systems have PBC in both directions and have a pinning field applied in one row along the short direction with $h_{\text{pinn}} = 0.05$. The quantities are energy per site, d- and p- (sum of p_x and p_y) occupancies, percentage of the doped holes in the Cu d band, expectation values of the hopping matrix elements (kinetic energy components), and the interaction energy.

Δ (eV)	$L_x \times L_y$	E_{tot}/M (eV)	n_d	n_p	δ_{n_d} (%)	T_{dd} (eV)	T_{pd} (eV)	T_{pp} (eV)	E_{int}/M (eV)
4.4	6×8	$-10.3389(1)$	0.764(1)	0.361(1)	31.7(1)	0.0538(3)	0.1345(3)	0.0584(3)	0.2006(1)
	6×12	$-10.3578(1)$	0.761(1)	0.364(1)	31.8(1)	0.0539(3)	0.1347(3)	0.0584(3)	0.2023(1)
	6×16	$-10.3679(1)$	0.759(1)	0.366(1)	31.3(1)	0.0543(3)	0.1345(3)	0.0589(3)	0.2036(1)
	6×20	$-10.3724(1)$	0.758(1)	0.367(1)	31.5(1)	0.0546(3)	0.1346(3)	0.0587(3)	0.2038(1)
	6×24	$-10.3762(1)$	0.758(1)	0.367(1)	31.8(1)	0.0541(3)	0.1347(3)	0.0587(3)	0.2040(1)
	$6 \times \infty$	$-10.395(1)$	0.754(1)	0.371(1)	31.6(1)				0.206(1)
	8×12	$-10.3572(1)$	0.761(1)	0.364(1)	31.9(1)	0.0539(3)	0.1339(3)	0.0587(3)	0.2025(1)
	8×14	$-10.3627(1)$	0.760(1)	0.365(1)	32.0(1)	0.0541(3)	0.1351(3)	0.0585(3)	0.2026(1)
	8×16	$-10.3658(1)$	0.760(1)	0.365(1)	32.3(1)	0.0533(3)	0.1348(3)	0.0588(3)	0.2027(1)
	8×18	$-10.3692(1)$	0.759(1)	0.366(1)	31.8(1)	0.0539(3)	0.1343(3)	0.0589(3)	0.2037(1)
	8×20	$-10.3718(1)$	0.758(1)	0.366(1)	31.8(1)	0.0542(3)	0.1339(3)	0.0588(3)	0.2037(1)
	$8 \times \infty$	$-10.393(1)$	0.754(1)	0.371(1)	31.9(1)				0.206(1)
2.5	6×8	$-9.0480(1)$	0.594(1)	0.531(1)	36.9(1)	0.0644(1)	0.1512(1)	0.0847(1)	0.1930(1)
	6×12	$-9.0737(1)$	0.591(1)	0.534(1)	36.2(1)	0.0641(1)	0.1505(1)	0.0844(1)	0.1941(1)
	6×16	$-9.0877(1)$	0.589(1)	0.536(1)	35.7(1)	0.0639(1)	0.1503(1)	0.0848(1)	0.1950(1)
	6×20	$-9.0942(1)$	0.588(1)	0.537(1)	36.1(1)	0.0636(1)	0.1498(1)	0.0846(1)	0.1949(1)
	6×24	$-9.0989(1)$	0.588(1)	0.537(1)	36.0(1)	0.0637(1)	0.1501(1)	0.0843(1)	0.1951(1)
	$6 \times \infty$	$-9.125(1)$	0.585(1)	0.540(1)	35.4(1)				0.196(1)
	8×12	$-9.0719(1)$	0.592(1)	0.533(1)	36.6(1)	0.0630(1)	0.1498(1)	0.0846(1)	0.1937(1)
	8×14	$-9.0794(1)$	0.592(1)	0.533(1)	36.9(1)	0.0630(1)	0.1501(1)	0.0841(1)	0.1935(1)
	8×16	$-9.0849(1)$	0.591(1)	0.533(1)	37.1(1)	0.0629(1)	0.1500(1)	0.0841(1)	0.1934(1)
	8×18	$-9.0886(1)$	0.590(1)	0.535(1)	36.7(1)	0.0628(1)	0.1498(1)	0.0843(1)	0.1939(1)
	8×20	$-9.0917(1)$	0.590(1)	0.535(1)	36.7(1)	0.0624(1)	0.1497(1)	0.0840(1)	0.1939(1)
	$8 \times \infty$	$-9.122(1)$	0.587(1)	0.538(1)	37.0(1)				0.194(1)

TABLE 3.3: Table of measured ground-state total energy at doping $h = 1/8$, for different supercell sizes $M = L_x \times 16$, at two different values of charge transfer energy Δ. All supercells use the same systematic parameters as in Tab. 3.2.

Δ (eV)	$L_x \times L_y$	E_{tot}/M (eV)
4.4	6×16	$-10.3679(1)$
	8×16	$-10.3658(1)$
	10×16	$-10.3672(1)$
	12×16	$-10.3682(1)$
2.5	6×16	$-9.0877(1)$
	8×16	$-9.0849(1)$
	10×16	$-9.0860(1)$
	12×16	$-9.0856(1)$

CHAPTER 4

Conclusion

Despite being a focal point in understanding high-temperature superconductivity, the underlying mechanisms and orders within the Cuprates is still ambiguous. The complexity of this highly correlated system makes a fully *ab initio* many-body treatment a formidable task, forcing theoretical research to the use of minimal models to describe the physics in the Copper-Oxygen plane. A majority of studies focus on the one-band Hubbard Hamiltonian, and many accurate results have been obtained that reflect results observed in experiment. Despite this, there is still no indication that this model displays superconducting order. Given recent advances in compuational power and experimental results that show that the Oxygen occupation have a non-trivial effect on critical temperature in different Cuprate families, we found it fit to move beyond to the three–band Hubbard (Emery) model.

Given that the characterization of the phases requires a detailed study of the bulk limit, we investigated in this work the three-band model at zero-temperature in the underdoped regime, using a state-of-the-art auxiliary-field quantum Monte Carlo (AFQMC) algorithm that can reach supercells up to 500 atoms. We focused on the nature of the spin and charge orders, and seek to quantify the competition between stripes, spin spirals, and

other nematic orders in the thermodynamic limit. Employing a self-consistent constraint [22] on paths sampled in auxiliary-field space, interfaced with GHF trial wave functions which are corrected internally and iteratively we believe we have robustly characterized the spin and charge orders that manifest in the ground state of the model.

In Chapter 2, we explored the spin and charge orders of the model as a function of the charge–transfer energy, Δ and doping, h. We found that, compared to the simplest picture of the one-band Hubbard model, the inclusion of the Oxygen p-orbitals within the three-band (Emery) model leads to new candidate phases with fascinating characteristics potentially of direct relevance to experimental observations in high-T_c materials that cooperate and compete, including magnetic domain walls, spin spirals, and nematic phases. We found that even at higher values of Δ a significant portion of holes occupied the Oxygen atoms highlighting the importance of the model.

We used the results from Chapter 2 to inform candidate trial wave functions to use in Chapter 3. Also informed by our half-filling study[34], we focused on studying two important regimes in Δ: at $\Delta = 4.4$, where the parent compound was found to be an AFM insulator, and at $\Delta = 2.5$, where it was found to be a non-magnetic metal. Accurate numerical results were obtained from computations on large supercells to provide systematic information on a variety of ground-state properties. We found the spin and charge order of the model to be extremely nuanced, with stripe order and $\Delta = 4.4$ and a competition between a SDW and spin spiral at $\Delta = 2.5$. Based on the performance of CP-AFQMC both in simplified models and in real materials, these results represent the state-of-the-art in many-body computation for the combination of accuracy and approaching the bulk limit in the model. Thus the detailed data will serve as useful benchmarks for future theoretical and computational studies.

The Emery model shows significant differences from the one-band Hubbard model at the mean field level. The ground state from generalized Hartree-Fock exhibits [46] a very

rich phase diagram including orders such as diagonal magnetic domain walls, nematicity, and spin spirals. At the many-body level, some of these features from GHF were not observed. The stripe state at $\Delta = 4.4$ and 1/8-doping is rather similar to what is seen in the one-band model. The spiral state at $\Delta = 2.5$, which is either the ground state or nearly degenerate with an SDW ground state, has not been seen in the simple one-band Hubbard model. (It is not clear whether some engineering of the hopping parameters beyond near-neighbors will make this state also appear in the one-band model.) So the answer to the question of how similar the Emery model is to the one-band Hubbard model is more nuanced. At $\Delta = 4.4$ the half-filled system has AFM order and is insulating, while the 1/8-doped system exhibits a stripe order as in the one-band model. On the other hand, the ground-state properties clearly show considerable sensitivity to parameter values and details. This basic feature is seen even in the one-band model, and is more pronounced in the Emery model, as reflected both in the variation with Δ and in the delicate balance at $\Delta = 2.5$ that we have observed. Indeed the presence of many competing or cooperating orders within small energy windows is a trademark of the real materials whose essential physics we hope are captured by these models. It is thus reasonable to assume, especially without precise knowledge of what balance of these states would be responsible for superconductivity, that the Emery model can be different in a non-trivial way. Moreover, we need to stress the flexibility that allows us to tune the charge-transfer energy to obtain occupation of d and p orbitals, n_d and n_p, which can be matched to different families of cuprates. This is certainly not available in the one-band model and it is very exciting since it is known that several properties of the cuprates including the superconducting critical temperature dramatically depend on n_d and n_p. Our results for the fate of excess holes and the localization appear to mirror the phenomenology of the different families real materials and this is very encouraging. Moreover, the Emery model captures the asymmetry seen in the phase diagram of the real materials between hole

doping and electron doping, which is not captured by the particle-hole symmetric one-band model.

We have not studied the nature of superconducting correlations in this work. Since our computations were done in the canonical ensemble, we could not directly measure superconducting order parameter. Pairing correlation functions can be measured, however these will have very small amplitude and will require systematic finite-size scaling with high resolution to determine the asymptotic (distance) behavior. We will leave this to a future investigation.

BIBLIOGRAPHY

[1] L. K. Wagner, private communication.

[2] J. M. Tranquada, AIP Conference Proceedings **1550**, 114 (2013), https://aip.scitation.org/doi/pdf/10.1063/1.4818402, URL https://aip.scitation.org/doi/abs/10.1063/1.4818402.

[3] J. M. Tranquada, B. J. Sternlieb, J. D. Axe, Y. Nakamura, and S. Uchida, Nature **375**, 561 (1995), URL http://dx.doi.org/10.1038/375561a0.

[4] M. Fujita, H. Hiraka, M. Matsuda, M. Matsuura, J. M. Tranquada, S. Wakimoto, G. Xu, and K. Yamada, Journal of the Physical Society of Japan **81**, 011007 (2012), https://doi.org/10.1143/JPSJ.81.011007, URL https://doi.org/10.1143/JPSJ.81.011007.

[5] J. Chang, E. Blackburn, A. T. Holmes, N. B. Christensen, J. Larsen, J. Mesot, R. Liang, D. A. Bonn, W. N. Hardy, A. Watenphul, et al., Nature Physics **8**, 871 (2012), URL http://dx.doi.org/10.1038/nphys2456.

[6] M. H. Fischer, S. Wu, M. Lawler, A. Paramekanti, and E.-A. Kim, New Journal of Physics **16**, 093057 (2014), URL http://stacks.iop.org/1367-2630/16/i=9/a=093057.

[7] D. Poilblanc and T. M. Rice, Phys. Rev. B **39**, 9749 (1989), URL https://link.aps.org/doi/10.1103/PhysRevB.39.9749.

[8] J. Zaanen and O. Gunnarsson, Phys. Rev. B **40**, 7391 (1989), URL https://link.aps.org/doi/10.1103/PhysRevB.40.7391.

[9] A. J. Millis and M. R. Norman, Phys. Rev. B **76**, 220503 (2007), URL https://link.aps.org/doi/10.1103/PhysRevB.76.220503.

[10] S. R. White and D. J. Scalapino, Phys. Rev. B **92**, 205112 (2015), URL https://link.aps.org/doi/10.1103/PhysRevB.92.205112.

[11] S. R. White and D. J. Scalapino, Phys. Rev. Lett. **80**, 1272 (1998), URL https://link.aps.org/doi/10.1103/PhysRevLett.80.1272.

[12] S. Sarker, C. Jayaprakash, H. R. Krishnamurthy, and W. Wenzel, Phys. Rev. B **43**, 8775 (1991), URL https://link.aps.org/doi/10.1103/PhysRevB.43.8775.

[13] A. Thomson and S. Sachdev, Phys. Rev. B **91**, 115142 (2015), URL https://link.aps.org/doi/10.1103/PhysRevB.91.115142.

[14] S. R. White and D. J. Scalapino, Phys. Rev. B **70**, 220506 (2004), URL https://link.aps.org/doi/10.1103/PhysRevB.70.220506.

[15] E. Dagotto, Rev. Mod. Phys. **66**, 763 (1994), URL https://link.aps.org/doi/10.1103/RevModPhys.66.763.

[16] V. J. Emery, Phys. Rev. Lett. **58**, 2794 (1987), URL https://link.aps.org/doi/10.1103/PhysRevLett.58.2794.

[17] N. P. Armitage, F. Ronning, D. H. Lu, C. Kim, A. Damascelli, K. M. Shen, D. L. Feng, H. Eisaki, Z.-X. Shen, P. K. Mang, et al., Phys. Rev. Lett. **88**, 257001 (2002), URL https://link.aps.org/doi/10.1103/PhysRevLett.88.257001.

[18] E. Fradkin, S. A. Kivelson, and J. M. Tranquada, Rev. Mod. Phys. **87**, 457 (2015), URL https://link.aps.org/doi/10.1103/RevModPhys.87.457.

[19] D. Sénéchal, P.-L. Lavertu, M.-A. Marois, and A.-M. S. Tremblay, Phys. Rev. Lett. **94**, 156404 (2005), URL https://link.aps.org/doi/10.1103/PhysRevLett.94.156404.

[20] P. W. Anderson and R. Schrieffer, Physics Today **44** (1991), URL https://physicstoday.scitation.org/doi/10.1063/1.881261.

[21] F. C. Zhang and T. M. Rice, Phys. Rev. B **37**, 3759 (1988), URL https://link.aps.org/doi/10.1103/PhysRevB.37.3759.

[22] M. Qin, H. Shi, and S. Zhang, Phys. Rev. B **94**, 085103 (2016), URL https://link.aps.org/doi/10.1103/PhysRevB.94.085103.

[23] J. P. F. LeBlanc, A. E. Antipov, F. Becca, I. W. Bulik, G. K.-L. Chan, C.-M. Chung, Y. Deng, M. Ferrero, T. M. Henderson, C. A. Jiménez-Hoyos, et al. (Simons Collaboration on the Many-Electron Problem), Phys. Rev. X **5**, 041041 (2015), URL https://link.aps.org/doi/10.1103/PhysRevX.5.041041.

[24] B.-X. Zheng, C.-M. Chung, P. Corboz, G. Ehlers, M.-P. Qin, R. M. Noack, H. Shi, S. R. White, S. Zhang, and G. K.-L. Chan, Science **358**, 1155 (2017), ISSN 0036-8075, https://science.sciencemag.org/content/358/6367/1155.full.pdf, URL https://science.sciencemag.org/content/358/6367/1155.

[25] M. Qin, C.-M. Chung, H. Shi, E. Vitali, C. Hubig, U. Schollwck, S. R. White, and S. Zhang, *Absence of superconductivity in the pure two-dimensional hubbard model* (2019), 1910.08931.

[26] R. Comin and A. Damascelli, Annual Review of Condensed Matter Physics **7**, 369 (2016), https://doi.org/10.1146/annurev-conmatphys-031115-011401, URL https://doi.org/10.1146/annurev-conmatphys-031115-011401.

[27] M. Jurkutat, D. Rybicki, O. P. Sushkov, G. V. M. Williams, A. Erb, and J. Haase, Phys. Rev. B **90**, 140504 (2014), URL https://link.aps.org/doi/10.1103/PhysRevB.90.140504.

[28] D. Rybicki, M. Jurkutat, S. Reichardt, C. Kapusta, and J. Haase, Nature Communications **7**, 11413 EP (2016), article, URL http://dx.doi.org/10.1038/ncomms11413.

[29] A. J. Achkar, F. He, R. Sutarto, C. McMahon, M. Zwiebler, M. Hcker, G. D. Gu, R. Liang, D. A. Bonn, W. N. Hardy, et al., Nature Materials **15**, 616 (2016), URL http://dx.doi.org/10.1038/nmat4568.

[30] J. Haase, O. P. Sushkov, P. Horsch, and G. V. M. Williams, Phys. Rev. B **69**, 094504 (2004), URL https://link.aps.org/doi/10.1103/PhysRevB.69.094504.

[31] X. Wang, M. J. Han, L. de' Medici, H. Park, C. A. Marianetti, and A. J. Millis, Phys. Rev. B **86**, 195136 (2012), URL https://link.aps.org/doi/10.1103/PhysRevB.86.195136.

[32] W. Ruan, C. Hu, J. Zhao, P. Cai, Y. Peng, C. Ye, R. Yu, X. Li, Z. Hao, C. Jin, et al., Science Bulletin **61**, 1826 (2016), ISSN 2095-9273, URL http://www.sciencedirect.com/science/article/pii/S2095927316306168.

[33] C. Weber, C. Yee, K. Haule, and G. Kotilar, Europhysics Letters **100**, 37001 (2012).

[34] E. Vitali, H. Shi, A. Chiciak, and S. Zhang, Phys. Rev. B **99**, 165116 (2019), URL https://link.aps.org/doi/10.1103/PhysRevB.99.165116.

[35] A. Dobry, A. Greco, J. Lorenzana, and J. Riera, Phys. Rev. B **49**, 505 (1994), URL https://link.aps.org/doi/10.1103/PhysRevB.49.505.

[36] W. A. Atkinson, A. P. Kampf, and S. Bulut, New Journal of Physics **17**, 013025 (2015), URL http://stacks.iop.org/1367-2630/17/i=1/a=013025.

[37] G. Dopf, A. Muramatsu, and W. Hanke, Phys. Rev. B **41**, 9264 (1990), URL https://link.aps.org/doi/10.1103/PhysRevB.41.9264.

[38] R. T. Scalettar, D. J. Scalapino, R. L. Sugar, and S. R. White, Phys. Rev. B **44**, 770 (1991), URL https://link.aps.org/doi/10.1103/PhysRevB.44.770.

[39] T. Yanagisawa, S. Koike, and K. Yamaji, Phys. Rev. B **64**, 184509 (2001), URL https://link.aps.org/doi/10.1103/PhysRevB.64.184509.

[40] M. Guerrero, J. E. Gubernatis, and S. Zhang, Phys. Rev. B **57**, 11980 (1998), URL https://link.aps.org/doi/10.1103/PhysRevB.57.11980.

[41] E. Arrigoni, M. Aichhorn, M. Daghofer, and W. Hanke, New Journal of Physics **11** (2009), URL 10.1088/1367-2630/11/5/055066.

[42] P. R. C. Kent, T. Saha-Dasgupta, O. Jepsen, O. K. Andersen, A. Macridin, T. A. Maier, M. Jarrell, and T. C. Schulthess, Phys. Rev. B **78**, 035132 (2008), URL https://link.aps.org/doi/10.1103/PhysRevB.78.035132.

[43] C. Weber, C. Yee, K. Haule, and G. Kotliar, EPL (Europhysics Letters) **100**, 37001 (2012), URL http://stacks.iop.org/0295-5075/100/i=3/a=37001.

[44] Z.-H. Cui, C. Sun, U. Ray, B.-X. Zheng, Q. Sun, and G. K.-L. Chan, arXiv: Strongly Correlated Electrons (2020).

[45] E. W. Huang, C. B. Mendl, S. Liu, S. Johnston, H. chen Jiang, B. Moritz, and T. P. Devereaux, Science **358**, 1161 (2017).

[46] A. Chiciak, E. Vitali, H. Shi, and S. Zhang, Phys. Rev. B **97**, 235127 (2018), URL https://link.aps.org/doi/10.1103/PhysRevB.97.235127.

[47] B.-X. Zheng, C.-M. Chung, P. Corboz, G. Ehlers, M.-P. Qin, R. M. Noack, H. Shi, S. R. White, S. Zhang, and G. K.-L. Chan, Science **358**, 1155 (2017), ISSN 0036-8075, http://science.sciencemag.org/content/358/6367/1155.full.pdf, URL http://science.sciencemag.org/content/358/6367/1155.

[48] C.-C. Chang and S. Zhang, Phys. Rev. Lett. **104**, 116402 (2010), URL https://link.aps.org/doi/10.1103/PhysRevLett.104.116402.

[49] G. Ehlers, S. R. White, and R. M. Noack, Phys. Rev. B **95**, 125125 (2017), URL https://link.aps.org/doi/10.1103/PhysRevB.95.125125.

[50] C.-C. Chang and S. Zhang, Phys. Rev. B **78**, 165101 (2008), URL https://link.aps.org/doi/10.1103/PhysRevB.78.165101.

[51] J. Xu, C.-C. Chang, E. J. Walter, and S. Zhang, Journal of Physics: Condensed Matter **23**, 505601 (2011), URL https://arxiv.org/abs/1107.0976.

[52] F. F. Assaad, Phys. Rev. B **47**, 7910 (1993), URL https://link.aps.org/doi/10.1103/PhysRevB.47.7910.

[53] L.-H. Pan and C.-D. Gong, Journal of Physics: Condensed Matter **18**, 9669 (2006), URL http://stacks.iop.org/0953-8984/18/i=42/a=013.

[54] G. Seibold, E. Sigmund, and V. Hizhnyakov, Phys. Rev. B **48**, 7537 (1993), URL https://link.aps.org/doi/10.1103/PhysRevB.48.7537.

[55] G. Seibold, J. Seidel, and E. Sigmund, Phys. Rev. B **53**, 5166 (1996), URL https://link.aps.org/doi/10.1103/PhysRevB.53.5166.

[56] A. Sadori and M. Grilli, Phys. Rev. Lett. **84**, 5375 (2000), URL https://link.aps.org/doi/10.1103/PhysRevLett.84.5375.

[57] G. Seibold, R. S. Markiewicz, and J. Lorenzana, Journal of Superconductivity and Novel Magnetism **26**, 49 (2013), ISSN 1557-1947, URL https://doi.org/10.1007/s10948-012-1701-3.

[58] S. Zhang and D. M. Ceperley, Phys. Rev. Lett. **100**, 236404 (2008), URL https://link.aps.org/doi/10.1103/PhysRevLett.100.236404.

[59] A. W. Overhauser, Phys. Rev. **128**, 1437 (1962), URL https://link.aps.org/doi/10.1103/PhysRev.128.1437.

[60] G. Seibold, R. S. Markiewicz, and J. Lorenzana, Phys. Rev. B **83**, 205108 (2011), URL https://link.aps.org/doi/10.1103/PhysRevB.83.205108.

[61] S. Zhang, J. Carlson, and J. E. Gubernatis, Phys. Rev. B **55**, 7464 (1997), URL https://link.aps.org/doi/10.1103/PhysRevB.55.7464.

[62] S. Zhang, in *Many-Body Methods for Real Materials: Modeling and Simulation*, edited by E. Pavarini, E. Koch, and S. Zhang (Verlag des Forschungszentrum Jülich, Jülich, Germany, 2019), vol. 9, URL http://www.cond-mat.de/events/correl19.

[63] J. P. F. LeBlanc, A. E. Antipov, F. Becca, I. W. Bulik, G. K.-L. Chan, C.-M. Chung, Y. Deng, M. Ferrero, T. M. Henderson, C. A. Jiménez-Hoyos, et al. (Simons Collaboration on the Many-Electron Problem), Phys. Rev. X **5**, 041041 (2015), URL https://link.aps.org/doi/10.1103/PhysRevX.5.041041.

[64] M. Motta, D. M. Ceperley, G. K.-L. Chan, J. A. Gomez, E. Gull, S. Guo, C. A. Jiménez-Hoyos, T. N. Lan, J. Li, F. Ma, et al. (Simons Collaboration on the Many-Electron Problem), Phys. Rev. X **7**, 031059 (2017), URL https://link.aps.org/doi/10.1103/PhysRevX.7.031059.

[65] K. T. Williams, Y. Yao, J. Li, L. Chen, H. Shi, M. Motta, C. Niu, U. Ray, S. Guo, R. J. Anderson, et al. (Simons Collaboration on the Many-Electron Problem), Phys. Rev. X **10**, 011041 (2020), URL https://link.aps.org/doi/10.1103/PhysRevX.10.011041.

[66] S. Zhang and H. Krakauer, Phys. Rev. Lett. **90**, 136401 (2003), URL https://link.aps.org/doi/10.1103/PhysRevLett.90.136401.

[67] H. Shi and S. Zhang, Phys. Rev. B **88**, 125132 (2013), URL https://link.aps.org/doi/10.1103/PhysRevB.88.125132.

[68] M. Zegrodnik, A. Biborski, and J. Spalek (2019).

[69] M. Zegrodnik, A. Biborski, M. Fidrysiak, and J. Spałek, Phys. Rev. B **99**, 104511 (2019), URL https://link.aps.org/doi/10.1103/PhysRevB.99.104511.

[70] R. Comin, R. Sutarto, E. H. da Silva Neto, L. Chauviere, R. Liang, W. N. Hardy, D. A. Bonn, F. He, G. A. Sawatzky, and A. Damascelli, Science **347**, 1335 (2015), ISSN 0036-8075, https://science.sciencemag.org/content/347/6228/1335.full.pdf, URL https://science.sciencemag.org/content/347/6228/1335.

[71] R. Resta and S. Sorella, Phys. Rev. Lett. **82**, 370 (1999), URL https://link.aps.org/doi/10.1103/PhysRevLett.82.370.

[72] O. Fischer, M. Kugler, I. Maggio-Aprile, C. Berthod, and C. Renner, Rev. Mod. Phys. **79**, 353 (2007), URL https://link.aps.org/doi/10.1103/RevModPhys.79.353.

VITA

Adam Chiciak

Adam Chiciak was born on January 14, 1992 in Hackensack, New Jersey. In high school, he showed interest in multiple sciences including biology, chemistry, and physics. He enrolled at Villanova University as a chemistry major, but quickly changed to astronomy & astrophysics before settling as a physics major, with minors in mathematics and business. He enrolled in graduate school at William & Mary in the fall of 2014. His initial interest in plasma physics led him to Professor Vahala to study nonlinear dynamics in his first year summer, but he eventually settled in the Shiwei Zhang's computational condensed matter group, focusing on lattice models for highly correlated systems, specifically high-temperature superconducting systems. He focused on the use of a few numerical techniques: generalized Hartree-Fock and auxiliary field quantum Monte Carlo. Post graduation, he hopes to take his knowledge and interest in machine learning and deep learning and apply to problems in the private sector in the growing field of data science.